UNIVERSITÀ DEGLI STUDI DI NAPOLI "FEDERICO II"

Dottorato di Ricerca in Fisica Fondamentale ed Applicata
XXIV Ciclo

Mario Merola

Study of the t-channel single top quark production and decay through $t \to Wb \to e\nu b$ at LHC with the CMS Experiment

Thesis for Doctor of Philosophy degree

Relatori:
Prof. Crisostomo Sciacca
Dott. Luca Lista

Coordinatore del Dottorato di Ricerca:
Prof. Raffaele Velotta

NOVEMBRE 2011

Contents

Introduction

The Large Hadron Collider (LHC) at CERN is a circular accelerator designed to provide proton-proton (and lead-lead ions) collisions with the unprecedented luminosity of $10^{34}\ \mathrm{cm}^{-2}\mathrm{s}^{-1}$ and a centre-of-mass energy of 14 TeV suitable for the study of rare events such as the production of the Higgs boson. Four are the main experiments situated in the interaction points where the proton beams collide: the general purpose CMS and ATLAS , the B-physics-oriented LHCb and the experiment dedicated to ion collisions, ALICE . During the first two years of running the CMS and ATLAS collected more than 5 fb^{-1} of data and published an impressive amount of physics results spanning from the first Standard Model precision tests, i.e. vector bosons production, to more complex and challenging measurements as top strong and electroweak production, towards searches for the Higgs boson and new physics beyond the Standard Model (supersymmetry, extra-dimenson theoretical models, etc.).

The work presented in this thesis consists of the study of one of the electroweak production modes of the top quark, the t-channel single top, done analyzing the collision data collected by the CMS detector during 2010 and 2011 data taking. The top quark, heaviest of the six constituting the three families of known quarks, was observed for the first time in the associated $t\bar{t}$ production at the proton-antiproton collider Tevatron at Fermilab in 1995. With more and more collected data, precision measurements of the top quark properties could be performed, till the first observation of the single top quark production in 2009 (first observation at LHC in 2010). The increased center of mass energy and the higher luminosity of the machine, make the LHC a top quark factory, producing at nominal energy and intensity around 1 $t\bar{t}$ pair per second and around 30 single tops per minute.

The aim of the analysis presented is to measure the t-channel single top production cross section after appropriate treatment of the underlying backgrounds has been established. For this purpose a data-driven estimation technique has been set up in order to minimize the effect of theoretical model uncertainties on the various backgrounds. Taking advantage of the particular topology of the process and of the spin correlations between the particles involved, a template fit signal extraction is performed and the t-channel cross section is measured.

The interest in the single top channels lies in the unique opportunity to explore the properties of a “bare quark”, such as spin, mass and charge, since it decays before had-

ronization could take place, and also to directly measure the V_{tb} CKM matrix element. Furthermore, the analysis hereafter presented could constitute the baseline for higher statistics studies: the single top channels sensitivity to new physics phenomena, indeed, allow us to test beyond Standard Model theories in the top quark sector, first of which the supersymmetric model.

The present thesis is organized in six chapters.
Chapter 1 briefly introduces the Standard Model of elementary particles, with particular emphasis to the Higgs mechanism.

Chapter 2 is devoted to a detailed description of the LHC accelerator machine and to the CMS detector.

Chapter 3 gives a picture of the physics results collected by LHC in the first year of data taking.

Chapter 4 presents the theoretical and experimental state of the art concerning the top quark physics, with particular stress on the recent measurements obtained at hadron colliders.

Chapter 5 contains the detailed description of the analysis set up for the single top cross section measurement in the t-channel. Starting from the event selection adopted to enrich the data sample in signal events, the data-driven techniques for backgrounds estimation are presented and in the end the fit procedure for signal extraction is described. This analysis is performed using the data collected by CMS in 2010.

Chapter 6 provides a preliminary update of the preceding analysis with a 25 times higher statistics collected in 2011. The strategy adopted in this case is slightly different from the 2010 analysis and in the text, omitting repetitions, these differences will be stressed.

Chapter 1

Standard Model

1.1 Introduction

The end of the last millennium witnessed the triumph of the Standard Model (SM) of the electroweak and strong interactions of elementary particles [1, 2]. The electroweak theory, proposed by Glashow, Salam and Weinberg [1] to describe the electromagnetic [3] and weak [4] interactions between quarks and leptons, is based on the gauge symmetry group $SU(2)_L \times U(1)_Y$ of weak isospin and hypercharge. Combined with Quantum Chromo-Dynamics (QCD) [2], the theory of the strong interactions between the colored quarks based on the symmetry group $SU(3)_C$, the model provides a unified framework to describe these three forces of Nature. Nevertheless there are established features of the universe the SM can not account for, among which the presence of dark matter, the baryon asymmetry, and neutrino masses. These are not considered as flaws of the SM, but as limitations of it, to be overcome by adding new elements, such as new interactions and new fundamental particles. With this perspective the LHC , starting from precision SM measurements in a new energy regime, has to probe, and hopefully provide evidence for, the existence of such new phenomena.

1.2 Standard Model of Elementary Particles

Quantum field theory combines two great achievements of physics in the 20th-century, quantum mechanics and special relativity. The Standard Model is a particular quantum field theory, based on the set of fields (particles) shown in Table 1.1, and the gauge symmetries $SU(3)_C \times SU(2)_L \times U(1)_Y$. There are three generations of quarks and leptons and one Higgs field ϕ. The index $i = 1, 2, 3$ on each field refers to the generation, and the subscript L, R refers to the chirality of the field ($\psi_{L,R} \equiv \frac{1}{2}(1 \mp \gamma_5)\psi$). The left-chiral and right-chiral fields corresponding to a given particle have different $SU(2)_L \times U(1)_Y$ quantum numbers, which leads to parity violation in the weak interaction.

Once the gauge symmetries and the fields are specified, the Lagrangian of the Standard Model is fixed by requiring it to be gauge invariant, local, and renormalizable. The Standard Model Lagrangian can be written as the sum of four pieces:

				T	T_3	Q
$Q_L^i =$	$\begin{pmatrix} u_L \\ d_L \end{pmatrix}$	$\begin{pmatrix} c_L \\ s_L \end{pmatrix}$	$\begin{pmatrix} t_L \\ b_L \end{pmatrix}$	$1/2$	$+1/2$ $-1/2$	$+2/3$ $-1/3$
u_R^i	u_R	c_R	t_R	0	0	$+2/3$
d_R^i	d_R	s_R	b_R	0	0	$-1/3$
$L_L^i =$	$\begin{pmatrix} \nu_L^e \\ e_L \end{pmatrix}$	$\begin{pmatrix} \nu_L^\mu \\ \mu_L \end{pmatrix}$	$\begin{pmatrix} \nu_L^\tau \\ \tau_L \end{pmatrix}$	$1/2$	$+1/2$ $-1/2$	0 -1
$e_R^i =$	e_R	μ_R	τ_R	0	0	-1
$\nu_R^i =$	ν_R^e	ν_R^μ	ν_R^τ	0	0	0
$\phi =$	$\begin{pmatrix} \phi^+ \\ \phi^0 \end{pmatrix}$			$1/2$	$+1/2$ $-1/2$	$+1$ 0

Table 1.1: The fields of the Standard Model and their weak isospin (T, T_3) and electric charge quantum numbers (Q).

$$\mathcal{L}_{SM} = \mathcal{L}_{Gauge} + \mathcal{L}_{Matter} + \mathcal{L}_{Higgs} + \mathcal{L}_{Yukawa}. \tag{1.1}$$

The first is the pure gauge interaction part, given by

$$\mathcal{L}_{Gauge} = \frac{1}{2g_S^2} Tr G^{\mu\nu} G_{\mu\nu} + \frac{1}{2g^2} Tr W^{\mu\nu} W_{\mu\nu} - \frac{1}{4g'^2} B^{\mu\nu} B_{\mu\nu}, \tag{1.2}$$

where $G^{\mu\nu}$ is the field-strength tensor of the gluon field, $W^{\mu\nu}$ is that of the weak-boson field, and $B^{\mu\nu}$ is the tensor for the hypercharge-boson field. These terms contain the kinetic energy of the gauge bosons and their self-interactions. The next piece is the Lagrangian for the fermions (the Matter Lagrangian), given by

$$\mathcal{L}_{Matter} = i\overline{Q}_L^i \not{D} Q_L^i + i\overline{u}_R^i \not{D} u_R^i + i\overline{d}_R^i \not{D} d_R^i + i\overline{L}_L^i \not{D} L_L^i + i\overline{e}_R^i \not{D} e_R^i. \tag{1.3}$$

The Einstein notation has been used, with the implicit sum on the repeated index (in this case the three generations). This term contains the kinetic energy of the fermions and their interactions with the gauge fields, which are contained in the covariant derivatives. For example,

$$\not{D} Q_L = \gamma^\mu \Big(\partial_\mu + i g_S G_\mu + i g W_\mu + i \frac{1}{6} g' B_\mu \Big) Q_L, \tag{1.4}$$

since the field Q_L participates in all three gauge interactions. Here $G_\mu \equiv T^a G_\mu^a$ with T^a for a =1,..., 8 the 3 $\times$ 3 matrices infinitesimal generators of $SU(3)_C$ symmetry and $W_\mu \equiv T^i W_\mu^i$ where T^i for i =1,..., 3 the 2 $\times$ 2 matrices generators of $SU(2)_L$ symmetry, i.e. the Pauli matrices. The theory thus far is very simple and elegant, but it is incomplete, for all the particles are massless. Mass terms for the gauge bosons and the fermions are forbidden by the gauge symmetries. As an example, the mass term for the up quark,

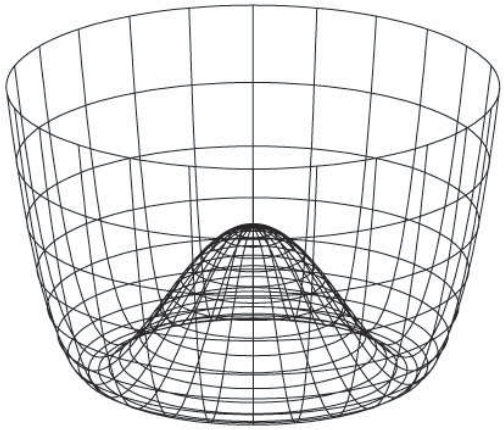

Figure 1.1: The Higgs potential. The neutral component of the Higgs field acquires a vacuum-expectation value $\langle\phi^0\rangle = v/\sqrt{2}$ on the circle of minima in Higgs-field space.

$$\mathcal{L} = -m\overline{u}_L u_R + h.c., \tag{1.5}$$

is forbidden by the fact that u_L and u_R are part of different SU(2) doublets and hence have different quantum numbers, breaking the gauge invariance of the Lagrangian. In the Standard Model the masses are put up via electroweak symmetry breaking, introducing an additional field, the Higgs doublet ϕ. So the simplest and most general Lagrangian for the Higgs field, consistent with gauge symmetry, is

$$\mathcal{L}_{Higgs} = (D^\mu\phi)^\dagger D_\mu\phi + \mu^2\phi^\dagger\phi - \lambda(\phi^\dagger\phi)^2. \tag{1.6}$$

The first term contains the kinetic energy of the Higgs field and its gauge interactions, while the other terms represent the Higgs potential, shown in Fig. 1.1. The coefficient of the quadratic term, μ^2, is the only dimensionful parameter in the Standard Model. The sign of this term has been chosen such that the minimum of the potential lies not at zero, but on a circle of minima

$$\langle\phi^0\rangle = \mu/\sqrt{2\lambda} \equiv \frac{v}{\sqrt{2}} \tag{1.7}$$

where ϕ^0 is the lower (neutral) component of the Higgs doublet field. This equation defines the parameter $v \approx 246$ GeV, the Higgs-field vacuum-expectation value. Exploiting the gauge invariance of the potential under $SU(2)_L$, we can arbitrarily choose

$$\langle\phi\rangle = \frac{1}{\sqrt{2}}\begin{pmatrix} 0 \\ v \end{pmatrix}. \tag{1.8}$$

With this choice the scalar doublet has an hypercharge number equal to 1 and so the symmetry generated by the electromagnetic charge is left unbroken, avoiding to give mass

to the photon,

$$Q_{em}\langle\phi\rangle = 0. \tag{1.9}$$

From the kinetic term in Eq. 1.6, we get the contribution for the gauge boson masses,

$$M^2_{GaugeBoson} \sim \frac{1}{2}(0,v)\left(\frac{1}{2}g\,\vec{\tau}\cdot\vec{W}_\mu + \frac{1}{2}g'B_\mu\right)^2 \begin{pmatrix} 0 \\ v \end{pmatrix}. \tag{1.10}$$

where $\vec{\tau}$ are the 2×2 Pauli matrices. After the substitution of the gauge fields with the physical ones, two charged $W^\pm$, and two neutral Z, A, we obtain

$$M_W = \frac{1}{2}gv, \tag{1.11}$$

$$M_Z = \frac{1}{2}\sqrt{g^2+g'^2}\,v, \tag{1.12}$$

$$M_A = 0. \tag{1.13}$$

The last piece in the Lagrangian is the Yukawa interaction of the Higgs field with the fermions, given by

$$\mathcal{L}_{Yukawa} = -\Gamma_u^{ij}\overline{Q}_L^i\epsilon\phi^* u_R^j - \Gamma_d^{ij}\overline{Q}_L^i\phi d_R^j - \Gamma_e^{ij}\overline{L}_L^i\phi e_R^j + h.c., \tag{1.14}$$

where ϵ is the unitary antisymmetric tensor in two dimensions, required to ensure each term separately to be electrically neutral, and the coefficients Γ_u, Γ_d, Γ_e are 3×3 complex matrices in generation space. Replacing the Higgs field with its vacuum-expactation value in Eq. (1.14) yields to the expression of fermion masses

$$M^{ij} = \Gamma^{ij}\frac{v}{\sqrt{2}} \tag{1.15}$$

To make the fermion masses manifest, a unitary field redefinition can be performed in order to diagonalize the mass matrices. Given A_{u_L} and A_{d_L} the transformation matrices for respectively u_L^i and d_L^i quark fields, it is defined CKM (Cabibbo-Kobayashi-Maskawa) matrix the quantity $V \equiv A_{d_L}^\dagger A_{u_L}$, which contains four free parameters, three mixing angles and one CP-violating phase. I want to conclude this section noting that although Standard Model Higgs mechanism gives an explanation for the masses of the particles, it does not explain the large difference, for example, between quarks masses and between fermions and bosons masses, neither it explains the origin of the small mixing angles in the CKM matrix. This suggests that there is a deeper structure underlying the Yukawa sector of the Standard Model, which is investigated in the so called "beyond the Standard Model" theories.

Chapter 2

LHC and CMS Detector

2.1 Introduction

The Large Hadron Collider (LHC) at CERN [5] is a two-ring superconducting proton-proton collider situated in the 27 km tunnel previously constructed for the large electron positron collider (LEP). It is designed to provide proton-proton collisions with unprecedented luminosity ($10^{34}\mathrm{cm}^{-2}\mathrm{s}^{-1}$) and a centre-of-mass energy of 14 TeV for the study of rare events such as the production of the Higgs particle if it exists. The LHC has two general purpose experiments, aiming to collect data with high luminosity, ATLAS [6] and CMS [7] and two experiments working at lower luminosity, LHCb [8] for B-physics ($10^{32}\mathrm{cm}^{-2}\mathrm{s}^{-1}$) and TOTEM [9] for the detection of protons from elastic scattering at small angles ($10^{29}\mathrm{cm}^{-2}\mathrm{s}^{-1}$). In addition to pp operation, the LHC is able to collide heavy nuclei (Pb-Pb) with a total centre-of-mass energy of 1150 TeV (2.76 TeV/nucleon) and for this it has one dedicated ion experiment, ALICE [10], aiming at a peak luminosity of $10^{27}\mathrm{cm}^{-2}\mathrm{s}^{-1}$.

The LHC presents many innovative features and a number of challenges which push the art of safely manipulating intense proton beams to extreme limits. The beams are injected into the LHC from the super proton synchrotron (SPS) at an energy of 450 GeV. After the two rings are filled, the machine is ramped to its nominal energy of 7 TeV over about 28 min. In order to reach this energy, the dipole field must reach the unprecedented level for accelerator magnets of 8.3 T. This high field can only be achieved using ”conventional” and affordable superconducting material (NbTi), by cooling the magnets in superfluid helium at 1.9 K. The cryogenic equipment needed to produce the about 100 tons of superfluid helium is unprecedented in scale and complexity. The tunnel diameter in the regular arc is only 3.8 m, insufficient for the installation of two separate rings. The two rings are therefore incorporated into a single magnetic structure with two sets of coils in a common yoke and cryostat, leading to a lowering of the production costs.

The LHC operations successfully started on September 10, 2008, but few days later, on September 19, an accident which caused substantial damage to the magnets and to the beam pipe imposed an intervention of repairs and improvements before another attempt for proton-proton collisions. Since further studies revealed that the accident was mainly due to the poor quality of electrical contacts between magnets, the CERN management

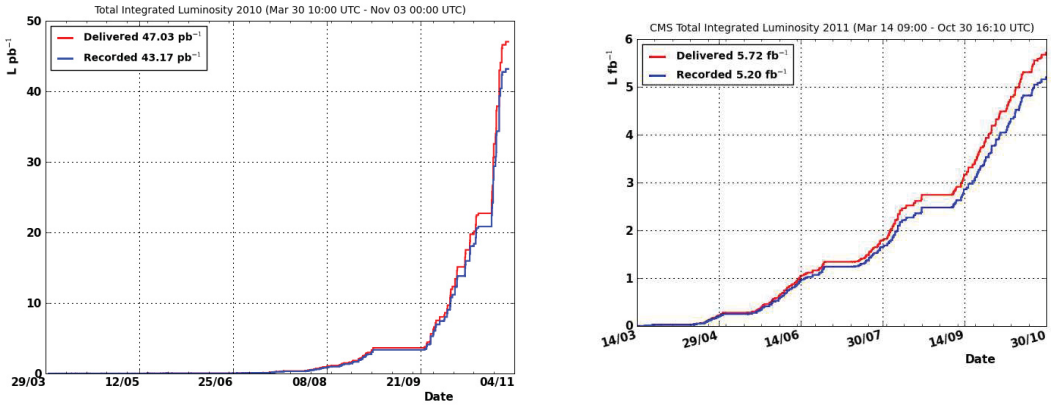

(a) (b)

Figure 2.1: Integrated luminosity versus time delivered to and recorded by CMS during stable beams at 7 TeV centre-of-mass energy, in 2010 (a) and 2011 (b).

decided to repair only the electrical contacts with the highest resistivities and operate the LHC for two years at a reduced beam energy of 3.5 TeV.

After the pilot runs at 0.9 and 2.36 TeV collision energies, LHC performed its first 7 TeV collisions on March 30, 2010, initially at very low luminosity, in the range of $\mathcal{L} = 1 \times 10^{27}\mathrm{cm}^{-2}\mathrm{s}^{-1}$. The aim of the machine operators in 2010 was to increase the number of protons per bunch, and successively throughout the year the number of bunches and the total stored energy. The instantaneous luminosity grew immediately exceeding $\mathcal{L} = 2 \times 10^{32}\mathrm{cm}^{-2}\mathrm{s}^{-1}$ at the end of the proton run on November 4, and then up to $\mathcal{L} = 3.6 \times 10^{33}\mathrm{cm}^{-2}\mathrm{s}^{-1}$ in October 2011. The experiments recorded data with a total integrated luminosity of about 50 pb^{-1} in 2010 and 5 fb^{-1} in 2011 (Fig. 2.1).

After a fast switch from proton to ion operation, the first lead-lead collisions in the LHC at a nucleon-nucleon center of mass energy of 2.76 TeV were observed on November 8, 2010. In the following heavy-ion run until December 6, the experiments recorded data corresponding to an integrated luminosity of about 10 $\mu\mathrm{b}^{-1}$.

2.2 The Large Hadron Collider

2.2.1 Machine Design

The LHC is supplied with protons from the injector chain Linac2 - Proton Synchrotron Booster (PSB) - Proton Synchrotron (PS) - Super Proton Synchrotron (SPS), as shown in Fig. 2.2.

At nominal luminosity, the energy stored in each beam is more than 350 MJ and this is more than two orders of magnitude than in any other previous machine (Fig. 2.3). It imposes unprecedented conditions on the reliability of the safety systems which must abort the beams cleanly if necessary as well as on the collimation systems which protect the machine and detectors from halo particles.

The number of events per second generated in the LHC collisions is given by:

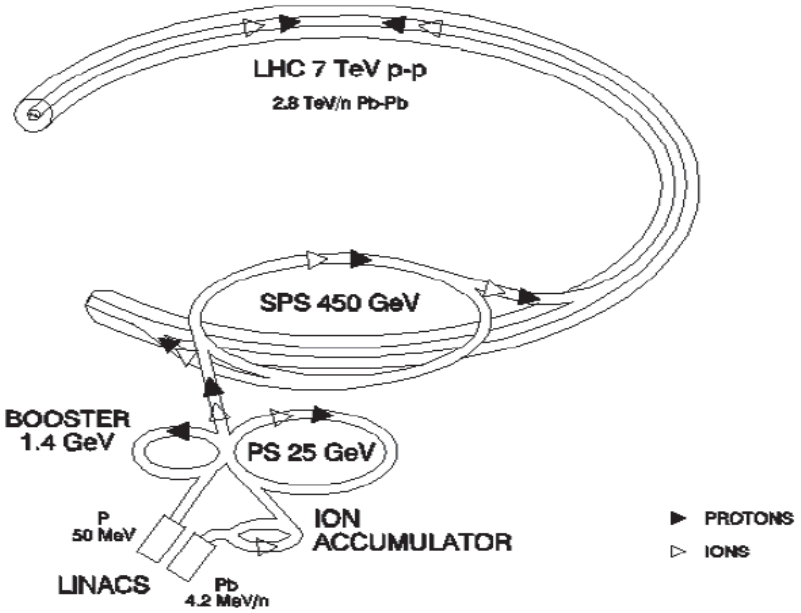

Figure 2.2: The LHC injector complex.

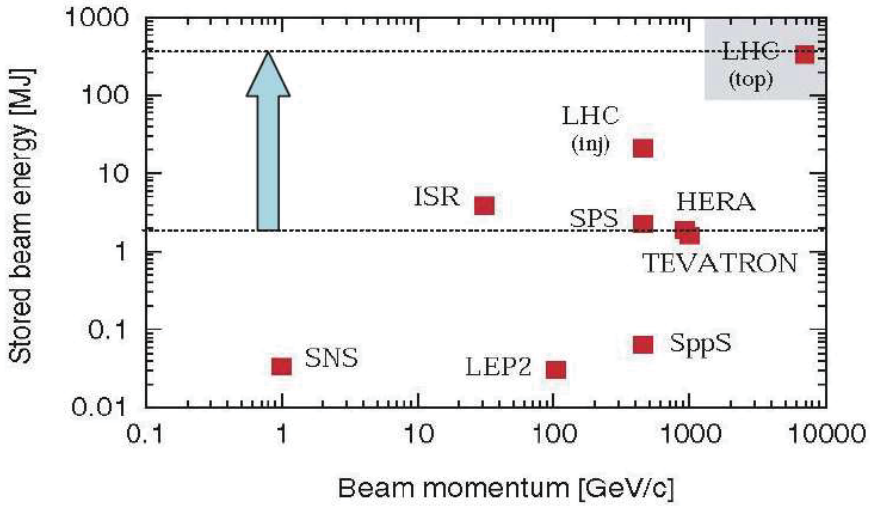

Figure 2.3: Energy stored in the accelerator beam, as a function of beam momentum. At less than 1% of nominal intensity LHC enters new territory.

$$N_{event} = L\sigma_{event} \tag{2.1}$$

where σ_{event} is the cross section for the event under study and L the machine luminosity. The luminosity depends only on the beam parameters and can be written for a Gaussian beam distribution as:

$$L = \frac{N_b^2 n_b f_{rev} \gamma_r}{4\pi\epsilon_n \beta^\star} F \tag{2.2}$$

where N_b is the number of particles per bunch, n_b the number of bunches per beam, f_{rev} the revolution frequency (11.245 kHz), γ_r the relativistic gamma factor, ϵ_n the normalized transverse beam emittance, $\beta^\star$ the beta function at the collision point, and F the geometric luminosity reduction factor due to the crossing angle at the interaction point (IP):

$$F = \left(1 + \left(\frac{\theta_c \sigma_z}{2\sigma^\star}\right)^2\right)^{-1/2} \tag{2.3}$$

θ_c is the full crossing angle at the IP, σ_z the RMS bunch length and $\sigma^\star$ the transverse RMS beam size at the IP.

Table 2.1 shows the main parameters required to reach the peak luminosity of 10^{34} $\mathrm{cm}^{-2}\mathrm{s}^{-1}$ for proton-proton collisions at 14 TeV centre-of-mass energy. It can be seen from the table that for the first time in a hadron machine, the synchrotron radiation at top energy is not negligible: a power of 3.6 kW per beam is radiated into a cryogenic environment and this strongly influences the design of the vacuum and cryogenic systems.

Circumference	26.7 km
Beam energy at collision	7 TeV
Beam energy at injection	0.45 TeV
Dipole field at 7 TeV	8.33 T
Luminosity	$10^{34} cm^{-2} s^{-1}$
Beam current	0.56A
Protons per bunch	1.1×10^{11}
Number of bunches	2808
Nominal bunch spacing	24.95 ns
Normalized emittance	$3.75 \mu m$
Total crossing angle	$300 \mu rad$
Energy loss per turn	6.7 keV
Critical synchrotron energy	44.1 eV
Radiated power per beam	3.8 kW
Stored energy per beam	350 MJ
Stored energy in magnets	11 GJ
Operating temperature	1.9K

Table 2.1: LHC design parameters.

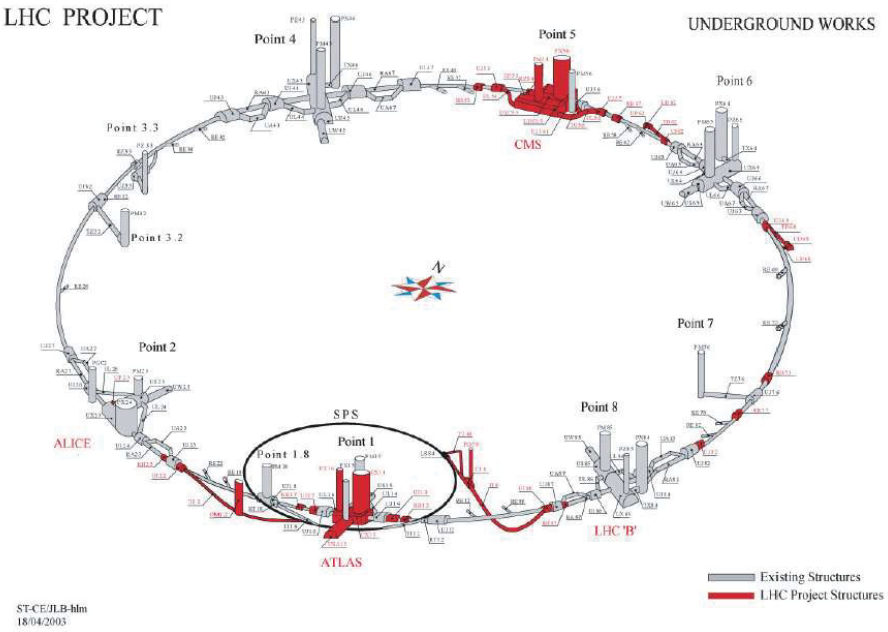

Figure 2.4: LHC layout.

2.2.2 Machine Layout

The basic layout of the LHC follows the LEP tunnel geometry and is shown in Fig. 2.4. The machine has eight arcs and straight sections, the last being approximately 528m long. Four of the straight sections house the LHC detectors while the other four are used for machine utilities, radio frequency and collimation systems, and beam dump insertions. The two high luminosity detectors are located at diametrically opposite straight sections. The ATLAS detector is located at point 1 and CMS at point 5, which also incorporates the small angle scattering experiment TOTEM. Two more detectors are located at point 2 (ALICE) and at point 8 (LHCb), which also contain the injection systems for the two rings. The beams only cross from one ring to the other at these four locations.

The straight section at point 3 is designed to capture off-momentum particles (momentum collimation) and the section at point 7 for removing the beam halo (betatron collimation). Point 4 contains the two radio frequency systems and finally point 6 contains the two abort systems which allow the beams to be extracted safely and dumped onto external absorbers.

The regular LHC lattice was designed to maximize the amount of bending power in the arc by making the dipoles as long as reasonably possible. This minimizes the amount of dead space between interconnects as well as the number of dipoles to be manufactured, tested and interconnected. After careful optimization, the dipole length was chosen to be 14.2m with a total of 23 regular arc cells. The two apertures of rings 1 and 2 are separated by 194 mm.

The transition from the arc to the straight section contains a dispersion suppressor consisting of two perturbed lattice periods (quadrupoles). In the arcs there are short straight sections containing the main quadrupoles and also the correction sextupoles for chromati-

city control and the orbit correction dipoles. Depending on their location, they can also contain skew quadrupoles or Landau damping octupoles. In the end, the optics of the long straight sections differ according to their functionality: at points 1 and 5 a small β (0.5)is required for collisions, at points 2 and 8 a different optics is required for 450 GeV beam and for 7 TeV beams and so on for the other points.

2.2.3 Magnets

The LHC contains more than 7000 superconducting magnets ranging from the 15m long main dipoles to the 10 cm octupole/decapole correctors inside the dipole cold masses as well as more than 100 conventional warm magnets and the about 500 conventional magnets in the two 2.6 km long transfer lines between the SPS and the LHC . The LHC magnet system, while still making use of the well-proven technology based on NbTi Rutherford cables, cools the magnets to a temperature of 1.8 K, using superfluid helium, and operates at fields above 8 T. This so low temperature with respect, for example, to the other large superconducting accelerators, Tevatron, HERA and RHIC which cools the magnets down to 4.5 K, brings a decrease of the heat capacity of the superconductor by an order of magnitude, making the magnets more sensitive to quenches.

A twin aperture dipole consists of two dipoles in a common iron yoke (Fig. 2.5). The two coils are clamped with austenitic steel collars with very low permeability surrounded by a yoke of low carbon steel which carries the magnetic flux. The stored energy of 500 $\mathrm{kJ\,m^{-1}}$ in the magnet at nominal field requires active quench protection. The coil is wound in two layers in six blocks separated with copper wedges and its geometry has been carefully optimized to achieve as pure a dipole field as possible, minimizing the higher harmonics of the field distribution.

The main arc quadrupoles, 3.25 m long, are made with the same superconducting cable as the outer layer of the dipoles. They are integrated into the small straight section (SSS), each containing a sextupole for chromaticity correction and a closed orbit correction dipole. Depending on its position in the arc, a SSS can also contain a trim quadrupole or a Landau octupole.

In addition to the main arc magnets, the LHC contains many more elements for correction of dipole imperfections, matching of the optics and in the final focus.

2.2.4 Cryogenics

The LHC magnets are cooled with pressurized superfluid helium, which has some interesting properties that make it a unique material. Best known is the very low viscosity which allows it to permeate the smallest cracks and in particular enabling the fluid to be in contact with the strands of the superconductor. The large specific heat (typically 10^5 times that of the superconductor per unit mass), combined with the enormous heat conductivity at moderate flux (3000 times that of cryogenic-grade OFHC copper, peaking at 1.9 K) can have a powerful stabilising action on thermal disturbances.

The machine is cooled using 8 cryogenics plants located in pairs at the even points except for point 2. At the tunnel level the conventional refrigerators are supplemented by

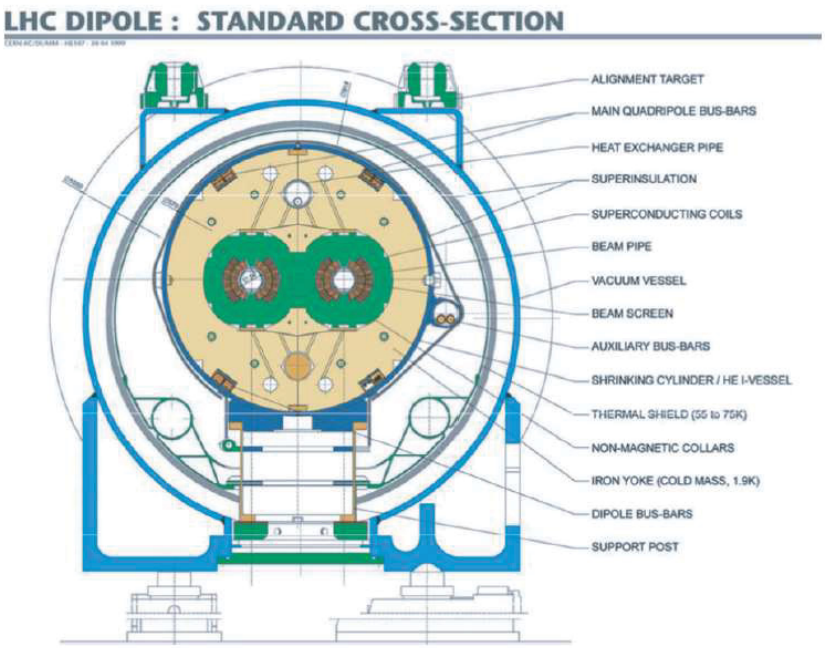

Figure 2.5: Dipole cross-section.

cold compressors. These multi-stage axial centrifugal compressors pump the cold helium gas producing the 15 mbar pressure in the linear heat exchangers inside the magnets in order to produce the primary superfluid. The connection to the magnets is made through a cryogenic distribution line running in the tunnel parallel to the machine.

2.2.5 The radiofrequency (RF) acceleration system

The RF system is located at point 4. Two independent sets of cavities operating at 400 MHz (twice the frequency of the SPS injector) allow independent control of the two beams. The superconducting cavities are made from copper whose internal surface is sputtered with a thin film of a few microns of niobium. In order to combat the intrabeam scattering (see below), each RF system must provide 16 MV during coast while at injection 8 MV is needed. Although the RF hardware required is much smaller than LEP due to the very small synchrotron radiation power loss, the real challenges are in controlling beam loading and RF noise.

2.2.6 The vacuum system

The design of the beam vacuum system takes into account the requirements of 1.9 K operation and the need to shield the cryogenic system from heat sources, as well as the usual constraints set by chamber impedances. The main heat sources are the synchrotron light radiated by the beam, the image currents, the development of electron clouds and the energy loss by nuclear scattering. Intercepting these heat sources at a temperature above 1.9 K has necessitated the introduction of a beam screen cooled to between 5 and 20 K (Fig. 2.6). This beam screen is perforated in about 4% of the surface area to allow the

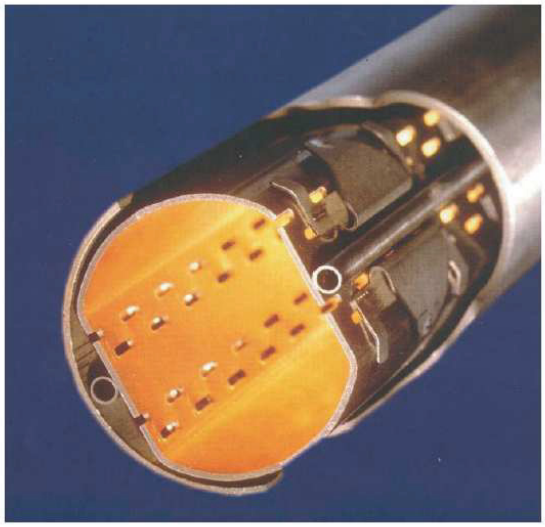

Figure 2.6: LHC beam screen.

cold bore of the magnets at 1.9K to act as a distributed cryopump. The slots in the beam screen are displaced in a pseudorandom pattern to avoid periodic perturbations which can induce resonant beam modes.

2.2.7 Accelerator physics issues

This part is devoted to a brief review of the different effects that could limit machine performance and the remedies been adopted.

Dynamic aperture

In superconducting magnets of the type used in the LHC, the field quality is determined by the precision of the positioning of the superconductor. It has been shown that the aperture inside which particles orbits are stable, is much smaller than the physical aperture of the beam pipe. It is called dynamic aperture and is limited mainly by the unwanted higher field harmonics due to magnet imperfections. Although sophisticated computer simulations take into account these effects, it is not possible to perform the full scale simulation over 4×10^7 turns, which correspond to 1 h of storage time. So, in order to insure a dynamic aperture of 6 sigmas, it has been decided to use the tracked dynamic aperture evaluated over 10^6 turns multiplied by a factor of 2.

The beam-beam interaction

The maximum particle density per bunch is limited by the nonlinear beam-beam interaction that each particle experiences when the bunches of both beams collide with each other. It produces two main effects: a variation of the tune with amplitude, and, because of the periodic nature of the force, the excitation of nonlinear resonances. The linear tune shift can be expressed by:

$$\xi = \frac{N_b r_p}{4\pi\epsilon_n} \tag{2.4}$$

in which r_p is the classical proton radius $r_p = e^2/(4\pi\epsilon_0 m_p c^2)$. Experience with hadron colliders indicates that the total linear tune shift summed over all IPs should not exceed 0.015, and in the LHC case, the tune shift must be $\xi < 0.005$. The long range beam-beam interactions between successive bunches are also reduced by colliding the beams with a small crossing angle of about 400 μrad.

Coherent instabilities

The interaction of the beam with its environment generates electromagnetic fields which can react back on it and drive it unstable. The first action is to design the vacuum chamber to reduce this coupling as much as possible, for example making the chamber smooth without discontinuities or reducing the resistivity of the copper in the beam screen by cooling it to between 5 and 20 K.

Nevertheless reducing the impedance of the environment can reduce but not definitely eliminate the growth of the instabilities. The two main instabilities to be kept under control are the transverse coupled bunch instability (resistive wall) and the single bunch head-tail instability.

Without entering in too much detail, the first is due to image currents in the beam screen and its main unstable modes are damped through the action of a pair of electrostatic deflectors. The head-tail effect is an instability due to the short range wakefields acting between the tail and the head of the bunch. It is taken under control by the action of sextupoles integrated into the short straight sections. Finally, the Landau damping, which acts on very high frequency oscillation modes, is provided with two families of strong octupoles without need for feedback and, for this reason, it is particularly important when the transverse feedback system has noise problems.

Electron cloud effects

A significant number of electrons can accumulate in the LHC vacuum chamber through ionization of residual gas molecules or by the impact of synchrotron radiation on the beam screen. When a proton bunch passes, these electrons receive an impulse and can hit the beam screen with energies of several hundred electron volts. The primary electrons produce secondaries and if the transit time of electrons through the chamber is equal to the

25 ns of bunch separation, the so called beam-induced multipacting effect takes place and the electron cloud grows exponentially. The main effect is an additional heat load in the cryogenic system and can also lead to instabilities. Simulations and experiments on the SPS have shown that, like a sort of auto-induced effect, a moderate scrubbing of the surface of the beam screen by electron bombardment quickly reduces the secondary emission yield (SEY) to a low enough value to allow design luminosity to be reached.

2.3 The Compact Muon Solenoid

The Compact Muon Solenoid (CMS) detector is a multi-purpose apparatus operating at the Large Hadron Collider at CERN. The total proton-proton cross-section at $\sqrt{s} = 14$ TeV is expected to be roughly 100 mb. At design luminosity the general-purpose detectors will therefore observe an event rate of approximately 10^9 inelastic events / s, leading to a number of formidable experimental challenges. The online event selection (*trigger*) must reduce the huge rate to about 100 events / s for storage and analysis. Furthermore, at design luminosity we expect a mean of about 20 inelastic collisions per bunch crossing and so around 1000 charged particles will emerge from the interaction region every 25 ns (time between two successive bunch crossing). The superimposition of other events on the event of interest, the so called pile-up effect, can be reduced by using high granularity detectors with good time resolution and low occupancy. This would inevitably require the use of millions of detector electronic channels which need very good synchronization.

The coordinate system adopted by CMS has the origin centered at the nominal collision point, the y-axis pointing vertically upward, the x-axis pointing radially inward toward the center of the LHC and the z-axis pointing along the beam direction. The azimuthal angle ϕ is measured from the x-axis in the $x - y$ plane, while the polar angle, θ, is measured form the z-axis. Pseudorapidity is defined as $\eta = -\ln\tan(\theta/2)$. Thus, the momentum and energy transverse to the beam direction, denoted by p_{T} and E_{T} (with $\not{E}_{\mathrm{T}}$ the energy imbalance in the transverse plane) are computed from the x and y components.

2.3.1 Detector Overview

The detector design and layout 2.7 is mainly driven by the choice of the magnetic field configuration, needing for large bending power to precisely measure high energy particles momentum. The heart of CMS detector is the big 4 T superconducting solenoid which accommodates the inner tracker and calorimetry inside and is situated immediately before the muon detectors. Schematically the detector layout, from the closest to the interaction point, is the following:

- 3 layers of silicon pixel detectors for measurement of the impact parameter and position of secondary vertices, and 10 layers of silicon microstrip detectors with high granularity and precision;
- electromagnetic calorimeter (ECAL) made of lead tungstate ($\mathrm{PbWO_4}$) crystals, with coverage in pseudorapidity up to $|\eta| < 3.0$. A preshower system is installed in front of the endcap ECAL for π^0 rejection;

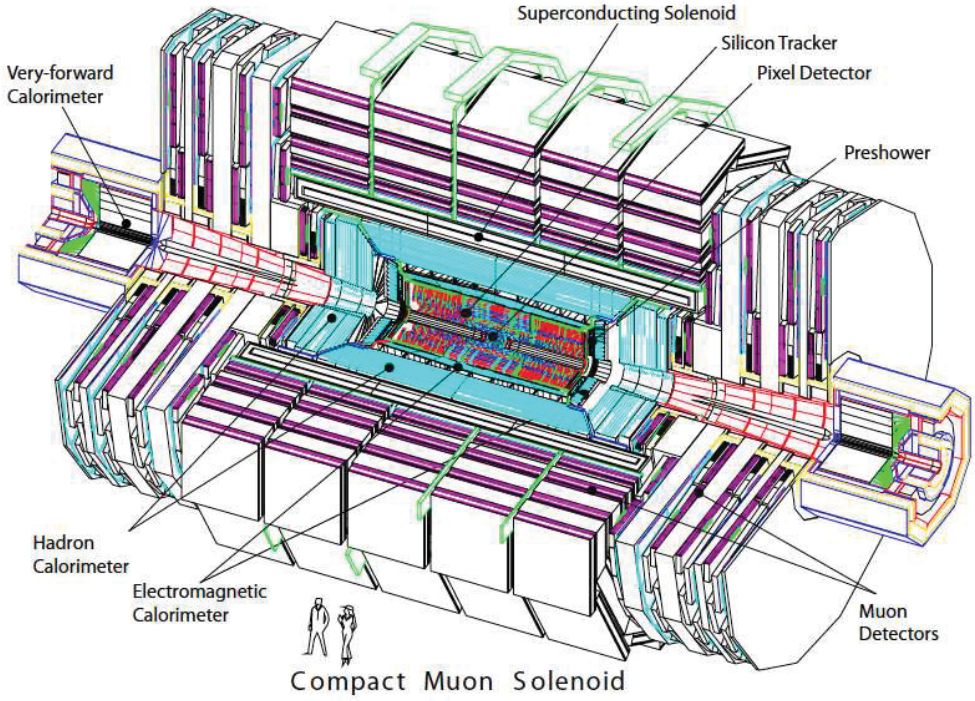

Figure 2.7: Perspective view of the CMS detector.

- brass / scintillator sampling hadron calorimeter (HCAL) with coverage up to $|\eta| < 3.0$, complemented by a $tail-catcher$ in the barrel region (HO) for better sampling of hadronic showers. Coverage up to a pseudorapidity of 5.0 is provided by an iron/quartz-fibre calorimeter. An even higher forward coverage is obtained with additional dedicated calorimeters (CASTOR, ZDC) and with the TOTEM tracking detectors;

- 4 muon stations consisting of several layers of aluminium drift tubes (DT) in the barrel region and cathode strip chambers (CSC) in the endcap region, complemented by resistive plate chambers (RPC).

The expected muon momentum resolution using only the muon system, using only the inner tracker, and using both sub-detectors is shown in Fig. 2.8, while Fig. 2.9 shows the jet transverse energy resolution in different pseudorapidity ranges.

2.3.2 Superconducting magnet

The CMS superconducting solenoid 2.10 has been designed to reach a 4 T field in a free bore of 6 m diameter and 12.5 m length with a stored energy of 2.6 GJ at full current. The flux is returned through a 10000-t yoke comprising 5 wheels and 2 endcaps. The distinctive feature of the 1.8 K, 220-t cold mass is the 4-layer winding made from a stabilized reinforced NbTi conductor, needed to be able to reach the desired 4 T magnetic field. The ratio between stored energy and cold mass is high (11.6 KJ/kg), causing a large mechanical deformation (0.15%) during energizing.

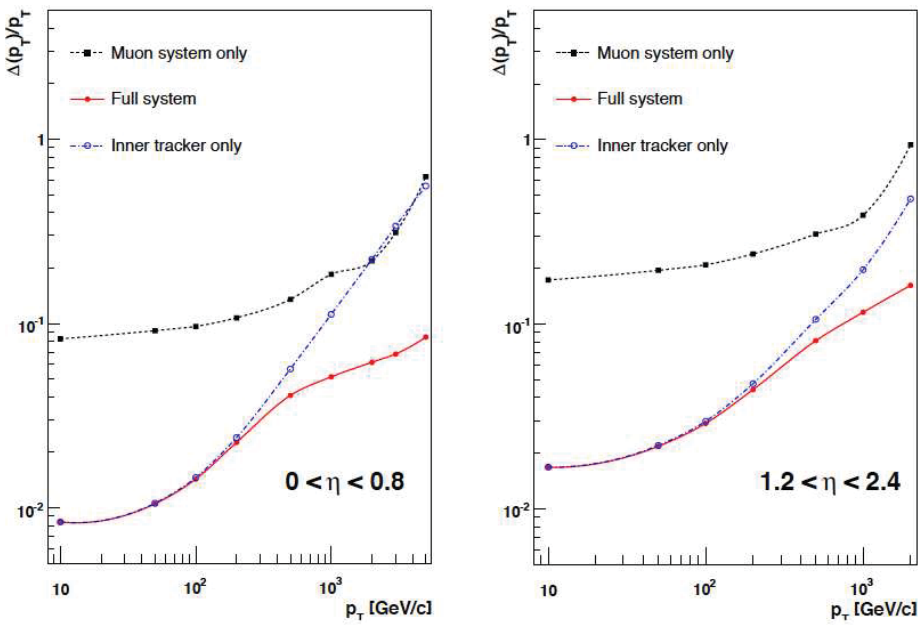

Figure 2.8: The muon transverse momentum resolution as a function of the transverse momentum (p_{T}) using the muon system only, using the inner tracking only, and both, for $|\eta| < 0.8$ (left) and $1.2 < |\eta| < 2.4$ (right).

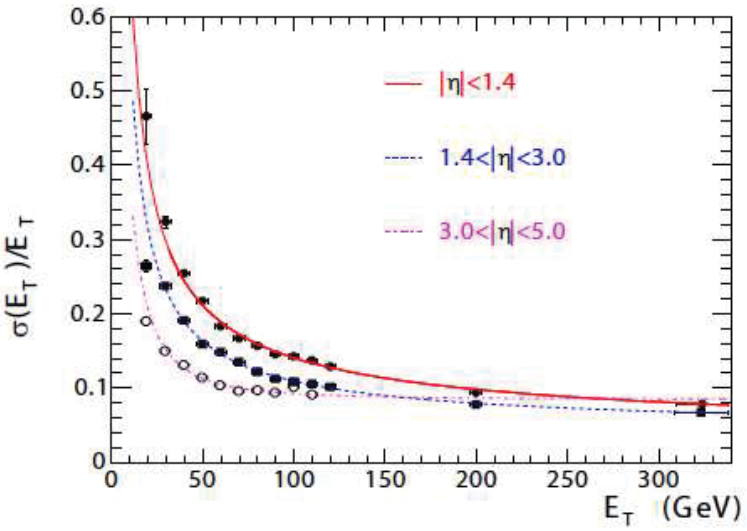

Figure 2.9: Jet transverse energy resolution as function of the jet transverse energy, in different pseudorapidity ranges.

2.3.3 Inner tracking system

The inner tracking system of CMS is designed to provide a precise and efficient measurement of the trajectories of charged particles emerging from the LHC collisions, as well as a precise reconstruction of secondary vertices. The tracker, fully covered by the solenoid magnetic field, surrounds the interaction region and has a length of 5.8 m and a diameter of 2.5 m. As already said, the high rate of interactions requires high granularity

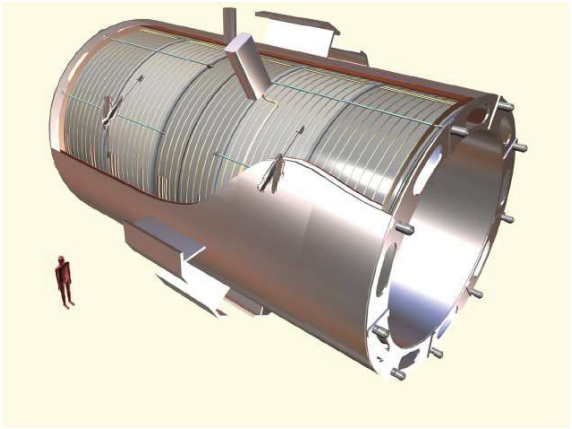

Figure 2.10: Artistic view of the 5 modules composing the cold mass inside the cryostat, with details of the supporting system.

and fast response as well as efficient cooling system and radiation hardness, aspects which led to the silicon technology choice. A schematic drawing of the CMS tracker is shown in Fig. 2.11.

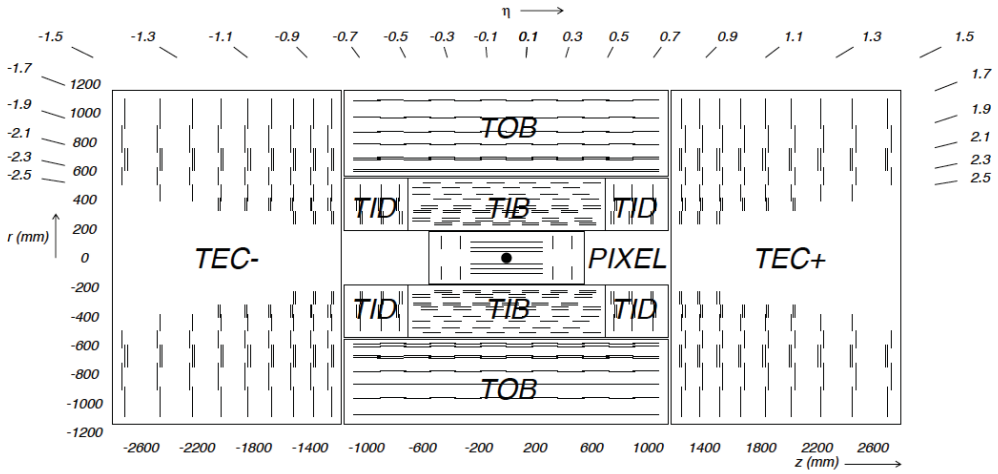

Figure 2.11: Schematic cross section through the CMS tracker. Each line represents a detector module. Double lines indicate back-to-back modules which deliver stereo hits.

The **pixel system** is the closest to interaction region part of the tracking system and is essential for the reconstruction of secondary vertices from b and τ decays, and forming seed tracks for the outer track reconstruction and high level triggering. At radii of 4.4, 7.3 and 10.2 cm, three cylindrical layers of hybrid pixel detector modules surround the interaction point, complemented by two disks of pixel modules on each side. Each pixel cell covers an area of $100 \times 150 \mu\mathrm{m}^2$, covering a total of $1\ \mathrm{m}^2$ with about 66 million pixels. Its pseudorapidity coverage goes from $\eta = -2.5$ to $\eta = 2.5$ (Fig. 2.12). The pixel detector delivers 3 high precision space points on each charged particle trajectory with a spatial resolution in the range of 15-20 $\mu\mathrm{m}$.

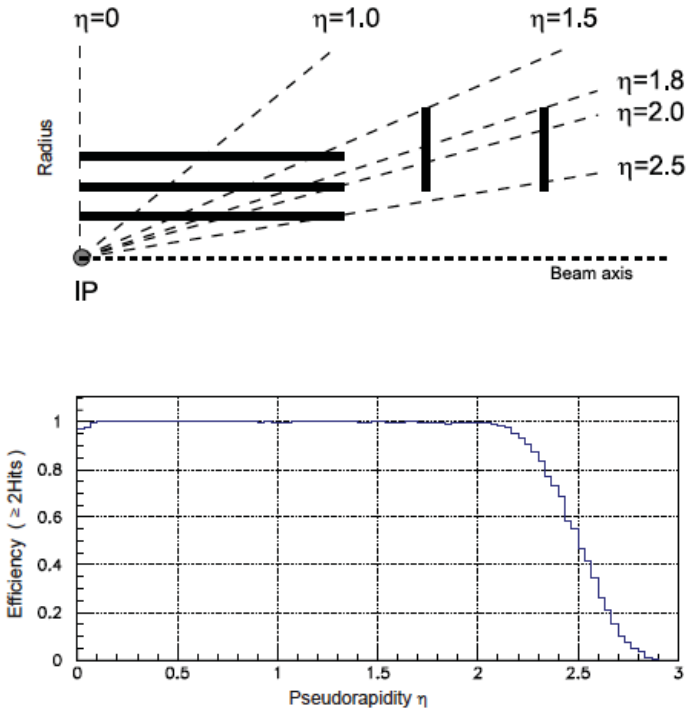

Figure 2.12: Geometrical layout of the pixel detector and hit coverage as a function of pseudorapidity.

The region between 20 cm and 116 cm is occupied by the **silicon strip tracker**, which is composed of three different subsystems: TIB/TID, TOB and TEC+/TEC-. The Tracker Inner Barrel and Disks (TIB/TID) are composed of 4 barrel layers and 3 disks at the end. They deliver up to 4 measurement in the r-ϕ plane on a trajectory, using 320 μm thick silicon micro-strip sensors. The single point resolution, depending on the strip pitch, in the is 23 μm for the first two layers and 35 μm for the third and fourth layer in the TIB, and extends from 100 μm to 141μm in the TID. The Tracker Outer Barrel (TOB) which surrounds the TIB/TID has an outer radius of 116 cm and consist of 6 barrel layers 500 μm thick. It provides another 6 points in $r - \phi$ plane with a single point resolution of 53 μm for the first 4 layers and 35 μm for the other two. The Tracker EndCaps (TEC+ and TEC-, where the sign indicate the position along the z axis) cover a region of 124 cm $< |z| <$ 282 cm and 22.5 cm $< |r| <$ 113.5 cm. Each TEC is composed of 9 disks, carrying up to 7 rings of silicon micro-strip-detectors with radial strips of 97 μm to 184 μm average pitch, providing up to 9 ϕ measurement per trajectory.

Furthermore some modules and rings of TIB, TID, TOB and TEC carry a second micro-strip detector module which is mounted back-to-back with a stereo angle of 100 mrad in order to provide a measurement of the second co-ordinate (z in the barrel and r on the disks). The single point resolution of this measurement varies with pitch and it is for example 230 μm and 530 μm in TIB and TOB. In conclusion the tracker ensures at least $\approx$ 9 hits in the silicon strip tracker in the full range of $|\eta| < 2.4$ with at least $\approx$ 4 of them being two-dimensional measurements.

2.3.4 Electromagnetic calorimeter

The electromagnetic calorimeter of CMS (ECAL) is a hermetic homogeneous calorimeter made of 61200 lead tungstate ($PbWO_4$) crystals mounted in the central barrel part, 7324 crystals in each of the two endcaps and a preshower detector placed in front of the endcap crystals (mainly for π^0 identification). Avalanche photodiodes (APDs) are used as photodetectors in the barrel and vacuum phototriodes (VPTs) in the endcaps. The high density of crystals give the calorimeter the characteristics of fast response, fine granularity and radiation resistance, as well as a good capability to detect the decay to two photons of the postulated Higgs boson.

The main radiation damage which the crystals undergo is a wavelength-dependent loss of light transmission. This damage can be tracked and corrected for by monitoring the optical transparency of the crystals with injected laser light [11, 12].

The energy resolution of the ECAL, for incident electrons as measured in a beam test, is shown in Fig. 2.13; the stochastic (S), noise (N), and constant (C) terms given in the figure are determined by fitting the measured points to the function:

$$\left(\frac{\sigma}{E}\right)^2 = \left(\frac{S}{\sqrt{E}}\right)^2 + \left(\frac{N}{E}\right)^2 + C^2. \tag{2.5}$$

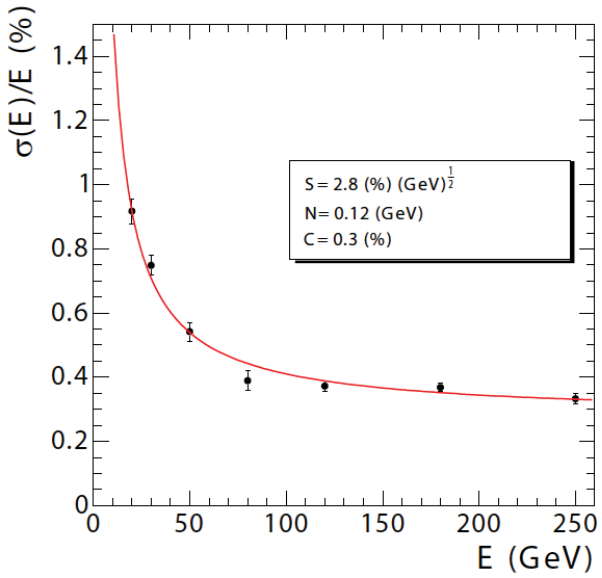

Figure 2.13: ECAL energy resolution, $\sigma(E)/E$, as a function of electron energy as measured from a beam test. The stochastic (S), noise (N) and constant (C) terms are given.

The **barrel** part of the ECAL (**EB**) covers the pseudorapidity range $|\eta| < 1.479$. The crystals are mounted in a quasi-projective geometry to avoid cracks aligned with particle trajectories, so that their axes make a small angle (3 °) with respect to the vector from the nominal interaction vertex, in both the ϕ and η projections. The crystal cross-section

corresponds to approximately 22×22 mm^2 at the front face of crystal and 26×26 mm^2 at the rear face, while its length is 230 mm corresponding to 25.8 X_0. The centres of the front faces of the crystals are at a radius 1.29 m. The crystals are contained in a thin-walled alveolar structure, submodules, which are assembled into modules of different types according to the position in η, each containing 400 or 500 crystals. Lastly four modules are assembled in a supermodule which contains 1700 crystals.

The **endcaps** (**EE**) cover the pseudorapidity range $1.479 < |\eta| < 3.0$. The longitudinal distance between the interaction point and the endcap envelope is 315.4 cm, taking account of the estimated shift toward the interaction point by 1.6 cm when the 4 T magnetic field is switched on. The endcap, which is divided into 2 halves, or *Dees*, consist of identically shaped crystals grouped in mechanical units of 5 × 5 crystals, the supercrystals (SCs), consisting of carbon-fibre alveolar structure. The crystals and SCs are arranged in a rectangular $x - y$ grid, with the crystals pointing at a focus 1300 mm beyond the interaction point, giving off-pointing angles ranging from 2 to 8 degrees. The crystals have a rear face cross section of 30 × 30 mm^2, a front face cross section 28.62 × 28.62 mm^2 and a length of 220 mm (24.7 X_0).

It is worth mentioning that the number of scintillation photons emitted by the crystals and the amplification of the signal are both temperature dependent, resulting in an overall variation of the response to incident electrons estimated $(-3.8 \pm 0.4)\%\,^{\circ}\mathrm{C}^{-1}$. Therefore the temperature of the system has to be maintained constant with high precision, within ±0.05 °C to preserve energy resolution, requiring a cooling system capable of extracting the heat dissipated by the read-out electronics. This system employs water which, flowing through thermal screens (which decouple crystals from the silicon tracker), pipes and aluminum cooling bars placed in close contact with the very front end electronics cards, is supplied at a temperature of 18 °C to each supermodule in the barrel, independently.

The principal aim of the CMS **Preshower detector** (**ES**) is to identify neutral pions in the endcaps within a fiducial region $1.653 < |\eta| < 2.6$. It also helps the electron identification and improve position determination with high granularity. The Preshower is a sampling calorimeter with two layers: lead radiators initiate electromagnetic showers from photons/electrons while silicon strip sensors placed after the radiator measure the deposited energy and the transverse shower profile. The material thickness traversed before reaching the first sensor plane is $2X_0$ plus a further $1X_0$ before reaching the second plane, making about 95% of single incident photons start showering before the second plane. Each silicon sensor has an active area of 61 × 61 mm^2 and the nominal thickness of 320 μm, so that a MIP (minimum ionizing particle) deposits 3.6 fC of charge in this thickness (at normal incidence).

The layout of the calorimeter is shown in Fig. 2.14, while Fig. 2.15 (a) and (b) show the barrel as mounted inside the hadron calorimeter and the supercrystal structure of one of the endcap dees, respectively.

2.3.5 Hadron calorimeter

The hadron calorimeters (HCAL) are particularly important for the measurement of hadron jets and neutrinos or exotic particles resulting in apparent missing transverse en-

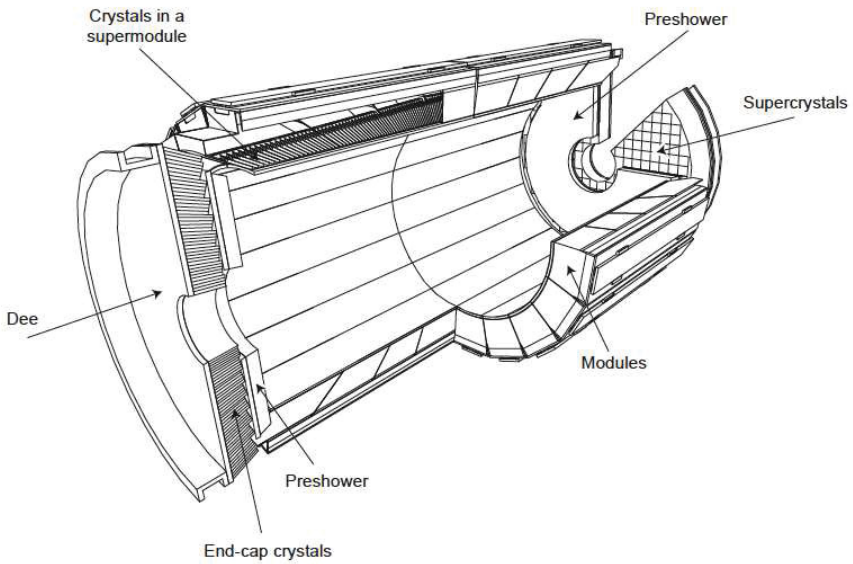

Figure 2.14: Layout of the CMS electromagnetic calorimeter showing the arrangement of crystal modules, supermodules and endcaps, with the preshower in front.

ergy. In Fig. 2.16 a longitudinal view of CMS detector is shown, with the HCAL in evidence. The hadron calorimeter barrel (HB) and endcaps (HE) sit behind the tracker and electromagnetic calorimeter as seen from the interaction point. The HB is radially restricted between the outer extent of the electromagnetic calorimeter (r = 1.77 m) and the inner extent of the magnet coil (r = 2.95 m). Thus, an outer hadron calorimeter (HO) or *tail catcher* is placed outside the solenoid complementing the barrel calorimeter, and forward calorimeters (HF) placed at 11.2 m from the IP guarantee a coverage in$|\eta|$ from 3 up to 5.2, using a Cherenkov-based, radiation-hard technology.

The **HB calorimeter** is a sampling calorimeter covering the pseudorapidity range $|\eta| < 1.3$. The HB is divided in two half-barrel sections (HB+ and HB-) consisting of 36 identical azimuthal wedges. The wedges are constructed out of flat brass absorber plates aligned parallel to the beam axis and bolted together in a such a way that each wedge contains no projective dead material. The total absorber thickness at 90 ° is 5.82 interaction lengths (λ_I) but increases with polar angle up to 10.6 λ_I at $|\eta| = 1.3$. The active medium uses the tile and wavelength shifting fibre concept to bring out the light. It is used the 3.7 mm thick Kuraray SCSN81 plastic scintillator for its long-term stability and moderate radiation hardness.

The hadron **calorimeter endcaps HE** cover a substantial portion of the pseudorapidity range, $1.3 < |\eta| < 3$ (13.2% of the solid angle), a region containing about 34% of the particles produced in the final state. The needed high radiation tolerance, non magnetic properties of the absorber material, sufficient high number or radiation length, good mechanical properties and reasonable cost led to the choice of C26000 cartridge brass. The HE is placed between the electromagnetic calorimeters EE and ES, and the muon endcap yoke. The design of the absorber is chosen in order to minimize the cracks between HB and HE. The brass plates, arranged in a staggered geometry with no projective dead

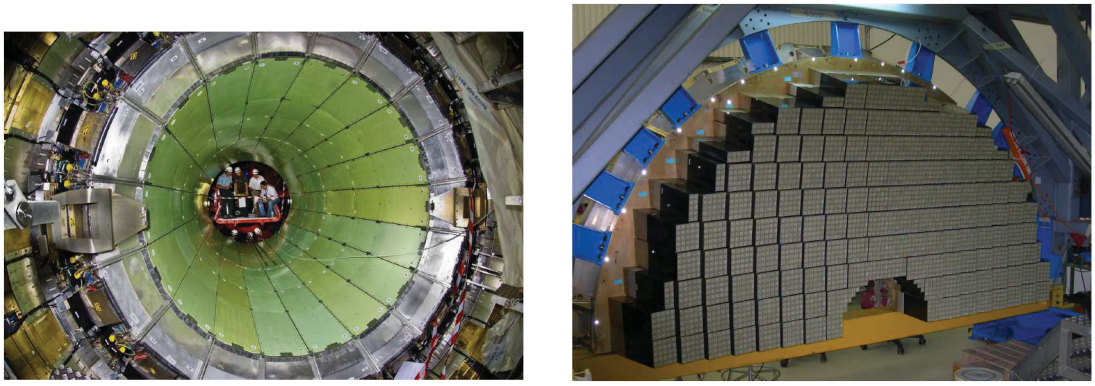

(a) (b)

Figure 2.15: (a) The barrel positioned inside the hadron calorimeter. (b) An endcap Dee, fully equipped with supercrystals

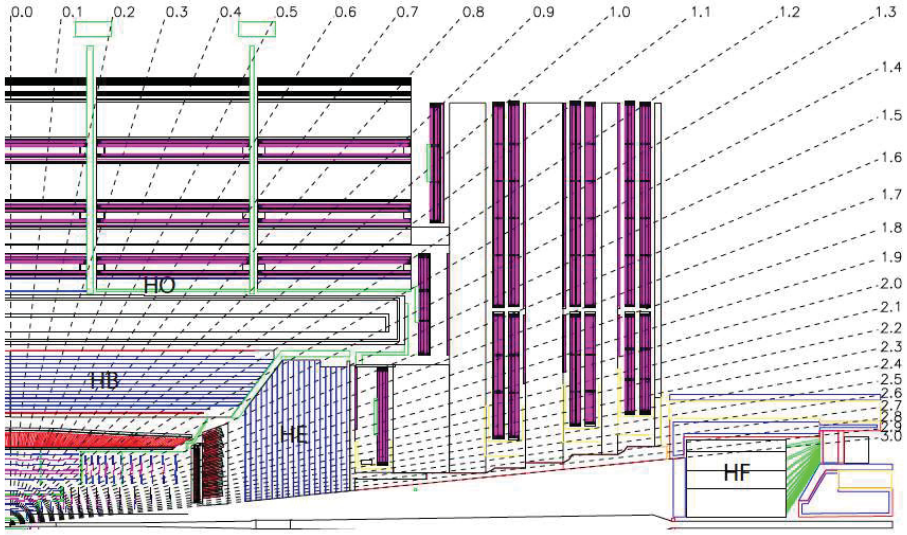

Figure 2.16: Longitudinal view of the CMS detector showing the locations of the hadron barrel (HB), endcap (HE), outer (HO) and forward (HF) calorimeters.

material, are 79 mm thick with 9 mm gaps for scintillators accommodation and result in about 10 interaction length (including electromagnetic crystals). The trapezoidal shaped scintillators are organized in trays inserted into the gaps in the absorber and have grooves in which the wavelength shifting fibres collecting scintillation light are inserted. Multipixel hybrid photodiodes (HPDs) are used as photodetectors for their low sensitivity to magnetic fields and their large dynamical range.

Since the combined stopping power of EB plus HB does not provide sufficient containment for hadron showers, in the central pseudorapidity region the hadron calorimeter is extended outside the solenoid coil with a tail catcher called **HO** or **outer calorimeter** (Fig. 2.17. The magnetic field, outside the vacuum tank of the solenoid, is returned through an iron yoke organized in five rings (the tail catcher iron), in which the HO is

placed as the first sensitive layer (in the central ring there are two layers of HO on either side, because of the lower coverage of the HB). The total depth of the calorimeter system is thus extended to a minimum of 11.8 λ_I except at the barrel-endcap boundary region. In detail, the HO consists of one or two layers of scintillator tiles located in front of the first layer of the barrel muon detector. Scintillation light from the tiles is collected using wavelength shifting fibres and transported to the photodetectors located on the structure of the return yoke. Studies using simulations of the CMS detector have shown that the physics impact of the HO detector is to recover the leakage in the central pseudorapidity region due to the small HB coverage.

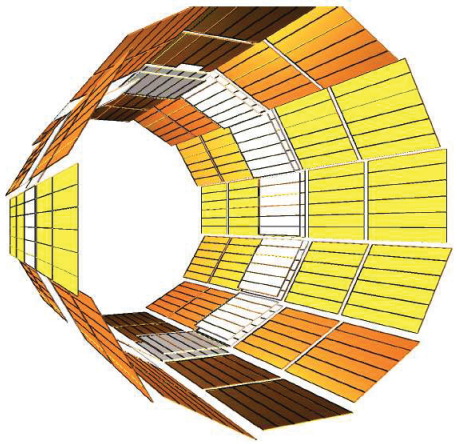

Figure 2.17: Layout of all the HO trays in the CMS detector.

The **forward calorimeter HF** experiences unprecedented particle fluxes. On average 760 GeV per proton-proton interaction is deposited into the two forward calorimeters, compared to only 100 GeV for the rest of the detector. Furthermore, this energy is concentrated at high rapidities, so that at $|\eta| = 5$ with an integrated luminosity of 500 fb^{-1} (≈10 years of LHC operations) the HF will experience ≈ 10 MGy and an extremely high rate of charged hadrons (at 125 cm from the beam-line the rate will exceed 10^{11} per cm^{-2}). For these reasons the radiation hardness of the active material is essential for successful operations, which led to the choice of quartz fibres (fused-silica core and polymer hard-cladding). The signal is generated when charged shower particles generate Cherenkov light, thereby rendering the calorimeter mostly sensitive to the electromagnetic component of showers.

The HF calorimeter consists of steel absorber structure that is composed of 5 mm thick grooved plates in which the fibres are inserted. To distinguish showers generated by electrons and photons from those generated by hadrons, two sets of fibres are read out separately: the first half runs over the full depth of the absorber (165 cm ≈ $10\lambda_I$) while the other half starts at a depth of 22 cm from the front of the detector, accordingly to the fact that electrons and photons lose a large part of their energy in the first 22 cm of the material. The whole structure is essentially cylindrical with outer radius of 130 cm, placed at 11.2 m from the interaction point, and is housed in a hermetic radiation shielding which consists of layers of 40 cm thick steel, 40 cm of concrete, and 5 cm of polyethylene.

The HF calorimeter is also used for the CMS real-time luminosity measurement, within 1% statistical accuracy (5 % of systematic uncertainty for offline analyses) with an update rate of 1 Hz. Two methods has been studied: the *zero counting* method considers the average fraction of empty towers to infer the mean number of interactions per bunch crossing, while the second exploits the linear relationship between the average transverse energy per tower and the luminosity.

2.3.6 Forward detectors

The **CASTOR** (**Centauro And Strange Object Research**) **detector** is a quartz - tungsten sampling calorimeter, with characteristics of radiation hardness, fast response and compact dimensions, designed for the very forward rapidity region in heavy ion and proton-proton collisions at the LHC. Its physics motivation is to complement the nucleus-nucleus physics program and also to study the diffractive and low-x physics in pp collisions. CASTOR is placed at 14.38 m from the interaction point, covering the pseudorapidity range $5.2 < |\eta| < 6.6$. The total and electromagnetic energy resolution in the typical acceptance range is around 1%. As the HF, it is a Cherenkov based calorimeter constructed from layers of tungsten plates as absorber and fused silica quartz plates as active medium. In the electromagnetic section it reaches 20.1 X_0, while in the hadronic section it has a total of 9.24 λ_I.

The **zero degree calorimeter** (**ZDC**), providing pseudorapidity coverage of $|\eta| \geqslant 8.3$ for neutral particles, is designed to complement the CMS very forward region, especially for heavy ion and pp diffractive studies. Two identical ZDCs are located between the two LHC beam pipes at $\approx$ 140 m on each side of the CMS interaction region, inside the neutral particle absorber TAN, designed to protect magnets and detectors against debris generated in the pp collisions and against beam halo and beam losses. The expected energy resolution on spectator neutrons is around 10-15%. As in the HF and CASTOR, the ZDC active material is made of tungsten-quartz fibres. The total depth of the calorimeter is $\approx$ 7.5 λ_I, divided in 6.5 λ_I for the hadronic section and 19 X_0 for the electromagnetic part.

2.3.7 The muon system

Muon detection is a very important tool to recognize signatures of interesting processes over the very high background rate expected at the LHC with full luminosity. An example can be the Standard Model Higgs boson decay in the full leptonic channel $H \rightarrow ZZ$ (or $ZZ^{\star}$) $\rightarrow 4l$, which, in case the leptons are muons, is called "gold plated" channel; or the large variety of BSM theories which predict the presence of muons among the final states. So, precise and robust muon measurement has been a central theme since from CMS earliest design stages (just think to the name given to the detector).

The muon system provides muon identification, momentum measurement and triggering. Good momentum resolution and trigger capability are achievable with the high solenoidal magnetic field and the flux return yoke (this serving also as hadron absorber for muon identification), while the identification of muons is provided through three dif-

ferent types of gaseous particle detectors (DT, CSC and RPC, see below and Fig. 2.18). Due to the shape of the solenoid magnet, the muon system was naturally driven to have a cylindrical barrel section and 2 planar endcap regions.

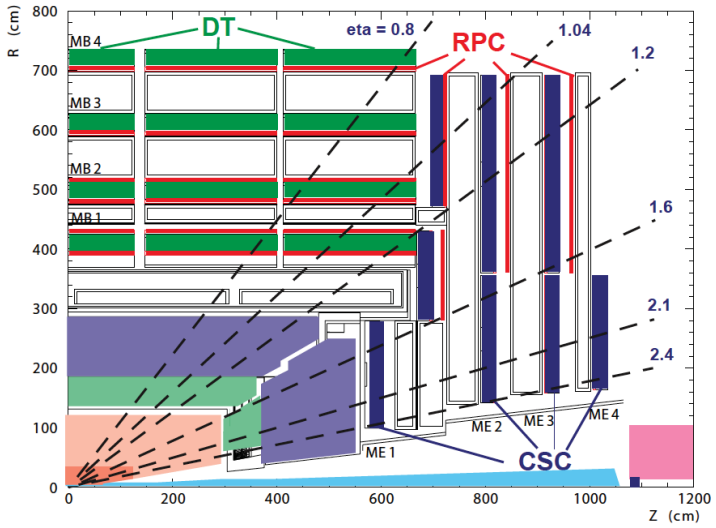

Figure 2.18: Layout of one quadrant of CMS , with DT, CSC and RPC in evidence.

In the barrel region where the muon rate is slow and the magnetic field is uniform and mostly contained in the steel yoke, **drift tube chambers** (**DT**) with rectangular drift cells are used. The chambers cover a pseudorapidity region $|\eta| < 1.2$ and are organized in 4 stations. The drift cells of each chamber are offset by a half-cell width with respect to their neighbor to eliminate dead spots in the efficiency. This design also allows to measure the muon time with excellent time resolution for efficient bunch crossing identification.

In the 2 endcap regions, where the muon rates and background levels are very high and the magnetic field is not uniform, the muon system uses **cathode strip chambers** (**CSC**). They are characterized by fast response time, fine segmentation and radiation resistance, identify muons with $|\eta|$ between 0.9 and 2.4 and also provide a precision measurement in the $r - \phi$ bending plane.

The offline reconstruction efficiency of simulated single muon samples (Fig. 2.19) is typically 95-99%. Due to the multiple scattering in the detectors before the first muon station, the offline muon momentum resolution of the standalone muon system is about 9% for small η and p values at 200 GeV (improved by an order of magnitude using also the inner tracker) and is between 15% and 40% at 1 TeV, depending on $|\eta|$ (improved to 5% using information from tracker system), Fig. 2.8. The most important characteristic of the DT and CSC is that they can each trigger on the p_T of muons with good efficiency and high background rejection, independent of the rest of the detector.

A complementary, dedicated trigger system consisting of **resistive plate chambers** (**RPC**) was added in both the barrel and endcap regions, providing independent and highly segmented trigger with a sharp p_{T} threshold (up to $|\eta| < 1.6$). They produce fast response with good time resolution but worst position resolution respect to DTs and CSCs. There are a total of 6 layers of RPCs in the barrel and a plane of RPCs in each of the first 3

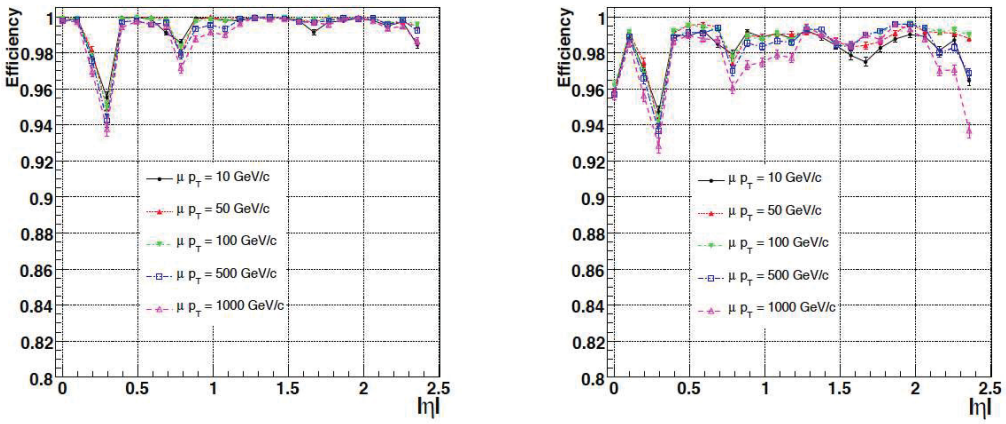

Figure 2.19: Muon reconstruction efficiency as a function of pseudorapidity for different values of p_{T}. Left panel: standalone reconstruction (using only hits from the muon system with a vertex constraint). Right panel: global reconstruction (using hits from both the muon system and the tracker).

stations in the endcaps.

Finally a sophisticated alignment system measures the positions of the muon detectors with respect to each other and to the inner tracker, in order to minimize the muon momentum resolution. Now, some more details follow about the three muons detectors.

The material thickness crossed by muons, as a function of pseudorapidity, is shown in Fig. 2.20.

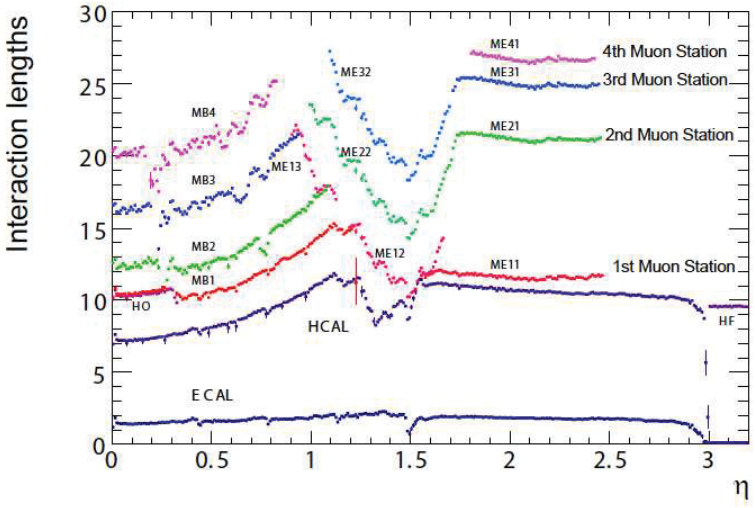

Figure 2.20: Material thickness in interaction lengths at various depths, as a function of pseudorapidity.

Drift tube system

The drift chambers containing more than 172000 sensitive wires are accommodated in the four muon stations in the CMS barrel, in a concentric cylindrical geometry around the beam line. The maximum path and time of drift is 21 mm and 380 ns in a gas mixture of Ar and CO_2, values suitable to produce negligible occupancy and also limit the number of active channels to an affordable value. In each of the 12 sectors of the yoke there are 4 muon chambers per wheel, labeled MB1, MB2, MB3, and MB4 (FIg. 2.21). A drift-tube chamber is made of 3 or 2 superlayers (SL, Fig. 2.22) each made of 4 layers of rectangular drift cells. The chamber structure use an aluminum honeycomb plate that separates the outer superlayer(s) from the inner one. The SLs are glued to the outer faces of the honeycomb. The cell design includes 5 electrodes, 1 anode wire, 2 field shaping strips, and 2 cathode strips. In each drift cell the anode is a 50 μm diameter gold-plated stainless steel wire. The field electrode is made of a 16 mm wide, 50 μm thick aluminum tape glued on a mylar tape that insulates the electrode with respect to the aluminum plate set to ground. Cathodes consists of a 50 μm thick, 11.5 mm wide aluminum tape placed on both sides of the I-beam and from it insulated. The multi-electrode design also ensures this performance in the presence of the stray magnetic field present in some regions of the chambers.

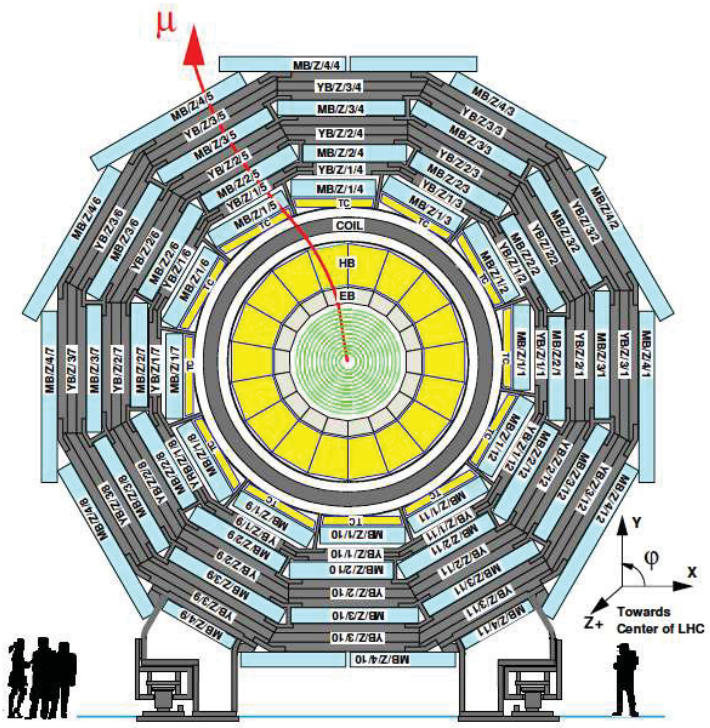

Figure 2.21: Layout of the CMS barrel muon DT chambers in one of the 5 wheels. The chambers in each wheel are identical with the exception of wheels -1 and +1 where the presence of cryogenic chimneys for the magnet shortens the chambers in 2 sectors.

A muon coming from the interaction point first encounters a ϕ-measuring SL, passes through the honeycomb plate, then crosses the z-measuring SL and the second ϕ-measuring

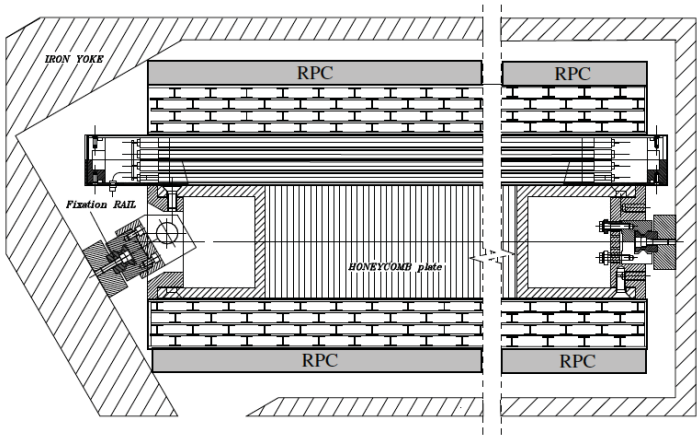

Figure 2.22: A DT chamber inside the iron yoke; the view is in the $(r-\phi)$ plane. One can see the 2 SLs with wires along the beam direction and the other perpendicular to it. In between is a honeycomb plate with supports attached to the iron yoke.

SL. At high momenta (greater than 40 GeV) the probability of electromagnetic cascades accompanying the parent muon becomes relevant. The redundancy needed to separate the electromagnetic component giving a good tracking efficiency and to cope with the background of neutrons and photons (whose rate is much larger than that from prompt muons) is obtained by having several layers of enough-separated drift cells per station. This design gives an efficiency to reconstruct a high p_T muon track with a momentum measurement delivered by the barrel muon system alone better than 95% in the pseudorapidity range covered by 4 stations, i.e., $\eta < 0.8$.

It's worth saying that the DTs also act as muon triggers. Briefly, the wire signals are the input to the so-called "Bunch and Track Identifiers" (BTIs), which through special algorithms obtain a trigger signal with bunch crossing identification. The BTIs search for coincidences which can correspond to certain track patterns. Then the trigger candidates in each chamber are selected and propagated to subsequent levels. The final selection of the DT muon trigger propagates the best four muon candidates per bunch crossing to the Global Muon Trigger.

Cathode strip chambers

The CMS Endcap Muon system consists of 468 cathode strip chambers (CSC) (Fig. 2.23). The chambers are trapezoidal and through overlapping provide contiguous ϕ-coverage. A muon in the pseudorapidity range $1.2 < |\eta| < 2.4$ crosses 3 or 4 CSCs, in the range $0.9 < |\eta| < 1.2$ is detected by both the barrel drift tubes and endcaps CSCs. In the baseline design, muons with $|\eta| < 2.1$ are also detected by resistive plate chambers (RPC).

The CSCs are multiwire proportional chambers comprised of 6 anode wire planes (filled with gas) interleaved among 7 cathode panels running in radial direction. The overall area covered by the sensitive planes of all chambers is about 5000 m^2, the gas volume is $> 50\mathrm{m}^3$, and the number of wires is about 2 million. The cathode chambers can

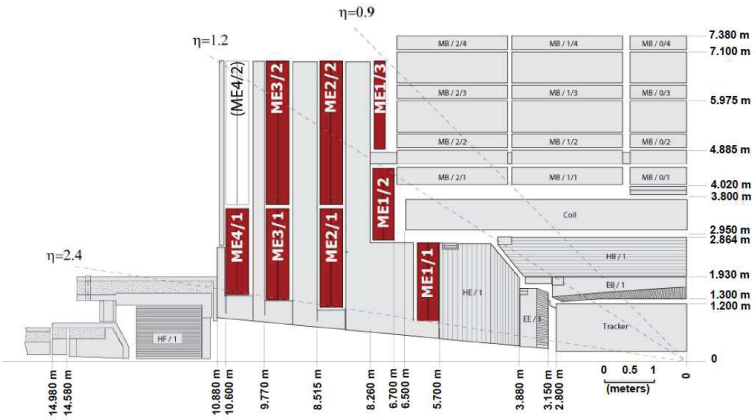

Figure 2.23: Quarter-view of the CMS detector. Cathode strip chambers of the Endcap Muon system (ME) are highlighted.

operate at high rates and in large non-uniform magnetic fields, providing precision muon measurement and trigger in one device. Each crossing muon can provide up to six spatial points per chamber, obtained combining the cathode strips and anode wire signals. The cathode strips collect the charge induced in the gas by the crossing muon, and by charge interpolation in three-strip clusters a very precise measurement is obtained. The anode coordinate is provided by the combined readout of wire groups. Among the performances of the CSCs we include the 99% efficiency per chamber, about 2 mm resolution in $r - \phi$ at the first level trigger and between 75 and 150 μm for offline reconstruction.

As for the DTs, CSC also work as trigger detectors. The trigger signal in a chamber depends on the presence of a local charged track (LCT) trigger, combining anode LCT and cathode LCT. The two signals are sent to the CSC track finder, which selects muon tracks in a 60° sector. Finally the CSC muon sorter selects four muons per bunch crossing and transmits them to the Global Muon Trigger.

Resistive plate chambers

Resistive Plate Chambers (RPC) are gaseous parallel-plate detectors that combine adequate spatial resolution with a time resolution comparable to that of the scintillators. An RPC is capable of tagging the time of an ionizing event in a much shorter time than the 25 ns between 2 consecutive LHC bunch crossings (BX), reaching a time resolution of 1.5 ns. Therefore, a fast dedicated muon trigger device based on RPCs can identify unambiguously the relevant BX to which a muon track is associated even in presence of high rate background expected at the LHC (rates may reach $10^3 \mathrm{Hz/cm^2}$). The RPC basic double gap module consists of 2 gaseous gaps, operating in avalanche mode with common strips in between (Fig. 2.24). Each gap is formed by two bakelite plates separated by insulating spacers. The bakelite plates are coated with conductive graphite paint acting as an electrode, insulated from the readout strips. Since the total induced signal is the sum of the 2 single-gap signals, the module can operate at lower voltage with an higher effective

detector efficiency.

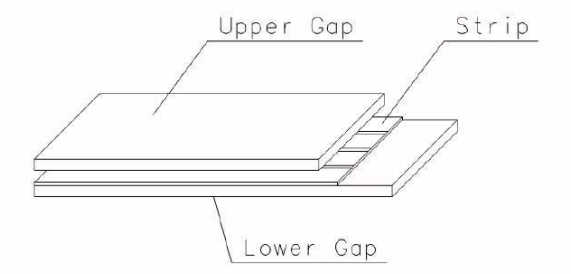

Figure 2.24: Layout of a double-gap RPC.

Six layers of RPC chambers are embedded in the barrel iron yoke. Redundancy present in the first 2 stations allows the trigger algorithm to perform the reconstruction always on the basis of 4 layers, even for low p_T particles, which may stop inside the iron yoke. In the endcap region, three layers of RPC are embedded in the iron yoke, covering the region up to $\eta = 1.6$.

Chapter 3

Physics at the LHC

3.1 Introduction

The Standard Model of particle physics and the Standard Cosmological Model synthesize four centuries of steady progress in understanding our world. Even if they describe the fundamental aspects governing the microscopic and macroscopic phenomena there are still open questions which need to find an answer. We know that about a quarter of the universe is matter and, and that about a fifth of the matter is made of quark and leptons. We know the universe is made almost entirely of matter and not antimatter, even though they were produced during the big bang in equal amounts. Certain observations, in conclusion, seem to suggest that the big bang was followed by a period of rapid space-time expansion, called inflation, and we don't know what the actual physical cause was. So, although some information from cosmology can still constrain the answers to these basic questions, it can not definitively solve these fundamental issues. The CERN Large Hadron Collider (LHC) is the tool that could provide, through its discoveries, what is needed to construct a more comprehensive theory which possibly explains the origin of the phenomena described in the Standard Models. In that sense we can regard the LHC as a "why machine", designed to discover signals of new physics testing supersymmetric models, string theories, etc.

This chapter is dedicated to the most significant physics results collected by the LHC experiments in the first year of data taking with some interesting updates using 2011 data. The physics program in the first two years was guided by the cross-sections of various reference processes as shown in Fig. 3.1.

With increasing luminosity throughout 2010 and 2011 the experiments have published results from high cross-section to lower cross-section processes, from multi-particle production, J/Ψ and Y, W and Z bosons, to top quark production and particle searches.

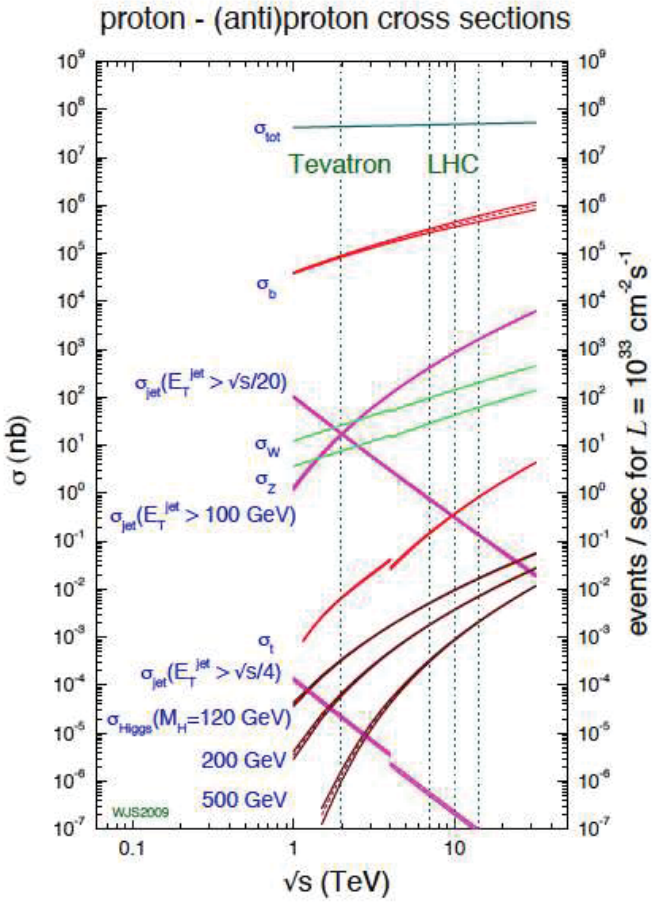

Figure 3.1: Cross-sections for Standard Model processes at hadron colliders as function of the center-of-mass energy.

3.2 Recent Physics results at the LHC

3.2.1 Charged particle multiplicity

The multi-particle production events are modeled by inelastic proton-proton collisions and diffraction at small momentum transfer, and are often referred to as minimum bias events, since the trigger requires only a minimal energy deposition in the forward and backward region of the detector. An interesting result shown by the CMS Collaboration concerns the particle correlations in the two dimensional $\Delta\eta$ and $\Delta\phi$ plane (Fig. 3.2) [13]. The observed structure in the correlation function at $\Delta\eta \approx 0$ and $\Delta\phi \approx 0$ can be interpreted as the manifestation of jet production and Bose-Einstein correlations. The backward ridge at $\Delta\phi \approx \pi$ is due to momentum conservation. The new observation of CMS is the appearance of a ridge at $\Delta\phi \approx 0$ in high multiplicity events with the number of charged particles larger than 110 and 1 GeV $< p_\perp <$ 3 GeV. A similar effect has already been observed at RHIC (Relativistic Heavy Ion Collider) in heavy ion collisions [14], but it is the first time the effect is observed in proton-proton collisions. The physical interpretation of the ridge is subject to further investigations.

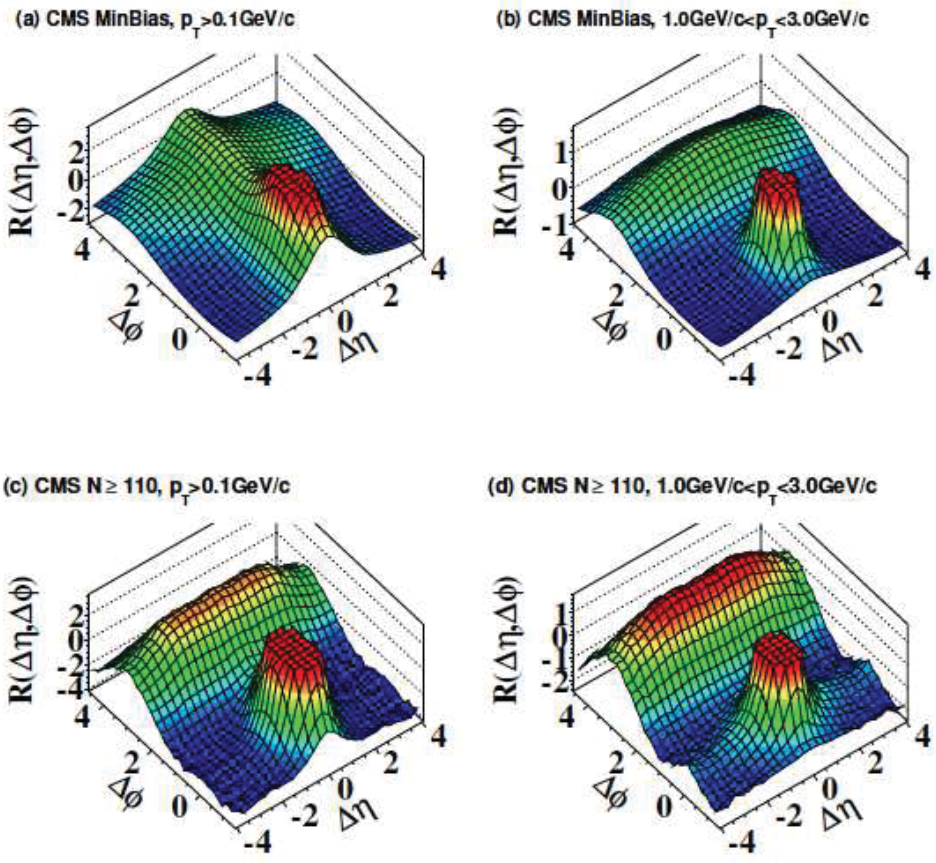

Figure 3.2: (a),(b) CMS measurement of 2D two particle correlations for minimum bias events, and (c), (d) high multiplicity events ($n_{track} > 110$).

3.2.2 Bottom quark production

The LHC is a factory of b-flavored hadrons. The LHCb detector is dedicated for the study of c- and b-quarks, having among its main goals the measurement of CP violation and the study of rare decays. First, the total cross section for $b\bar{b}X$ production has been measured, as well as the production cross sections of b-flavored hadrons as J/ψ, Y and B.

LHCb has obtained first results on the branching ratio $B_s \to \mu^+\mu^-$ analyzing 37 pb^{-1} of 2010 data. The Standard Model predicts a value of $(0.32 \pm 0.02) \times 10^{-8}$, but new resonant states, for example supersymmetric particles, could increase this branching ratio substantially. A precise measurement of the branching ratio is therefore one of the best tests for new physics in B meson decays. The 95% C.L. limits [15] obtained

$$\mathcal{B}(B_s^0 \to \mu^+\mu^-) < 5.6 \times 10^{-8}, \quad (3.1)$$
$$\mathcal{B}(B_d^0 \to \mu^+\mu^-) < 1.5 \times 10^{-8}. \quad (3.2)$$

are comparable to limits found at Tevatron with about 6 fb^{-1}. More recent measurements performed by the CMS experiment with 1.14 fb^{-1} of 2011 data lead to more strict limits on the branching rations [16]

$$\mathcal{B}(B_s^0 \to \mu^+\mu^-) < 1.9 \times 10^{-8}, \quad (3.3)$$
$$\mathcal{B}(B_d^0 \to \mu^+\mu^-) < 4.6 \times 10^{-9}. \quad (3.4)$$

3.2.3 Intermediate Vector Bosons and Top Quark

An important milestone for the LHC experiments in 2010 was the measurement of the production cross-sections of W and Z bosons. Notably if we consider that the Higgs boson is expected to decay with high branching fractions into pairs of W and Z and, in general, the intermediate vector bosons are among the main sources of background to new physics processes. The main background of QCD multi-jet events is rejected by the requirement of a charged lepton with high transverse momentum and significant missing transverse energy (for W) or a second oppositely charged lepton (for Z). The results are reported in Fig. 3.3, where the LHC measurements are compared to results at lower energies [17].

ATLAS and CMS have also measured the charge asymmetry of inclusive semi-leptonic W decays and the first measurement of the W polarization at hadron colliders. In particular, in Fig. 3.4 the recent CMS results are shown [18]. The values of charge asymmetry measured with electrons and muons are in good agreement with each other and provide useful information on the u- and d-quark momentum fractions in the proton. The latter

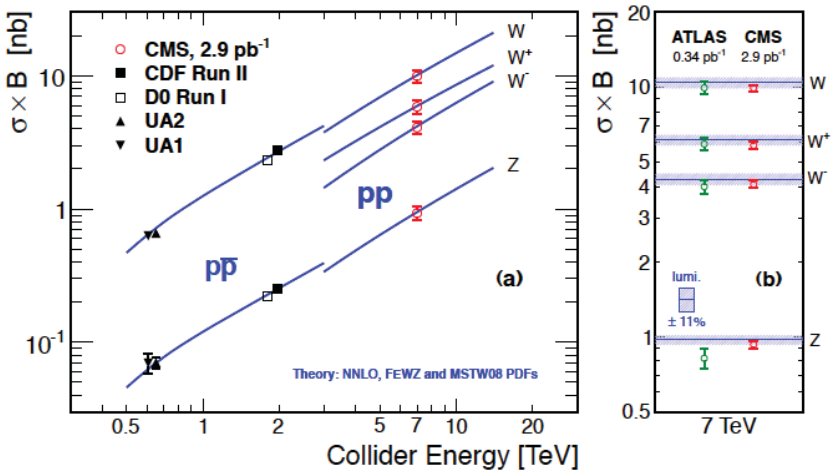

Figure 3.3: (a) Measurements of inclusive W and Z production cross-sections times branching ratio as a function of center-of-mass energy for CMS and experiments at lower-energy colliders. The lines are the NNLO predictions. (b) Comparison of the ATLAS and CMS W and Z production cross-sections times branching ratios. The error bars are the statistical and systematic uncertainties added in quadrature.

and the measurement of the W polarization, that confirms the preferably left handed production of both W^+ and W^-, prove that the LHC is ready to complex and challenging precision electroweak tests as additional data are available. A recent update on electroweak cross section measurements in shown in Fig. 3.5.

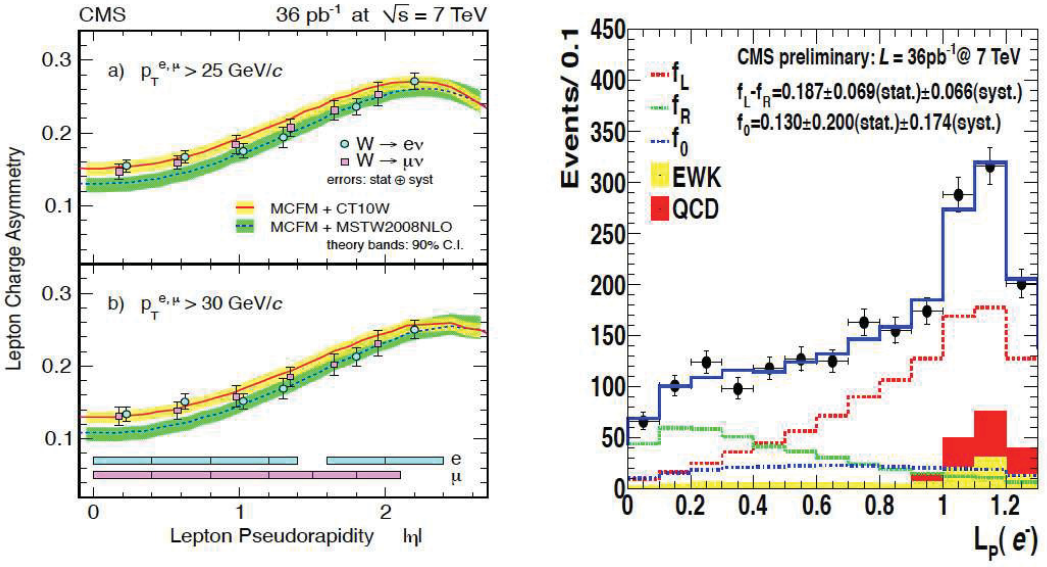

Figure 3.4: Measurement of the lepton charge asymmetry in W events (left) and of the W polarization (right), in CMS .

The selection of top candidates is particularly challenging since it requires a complete understanding of all major physics objects as detected by the experiments. The first top

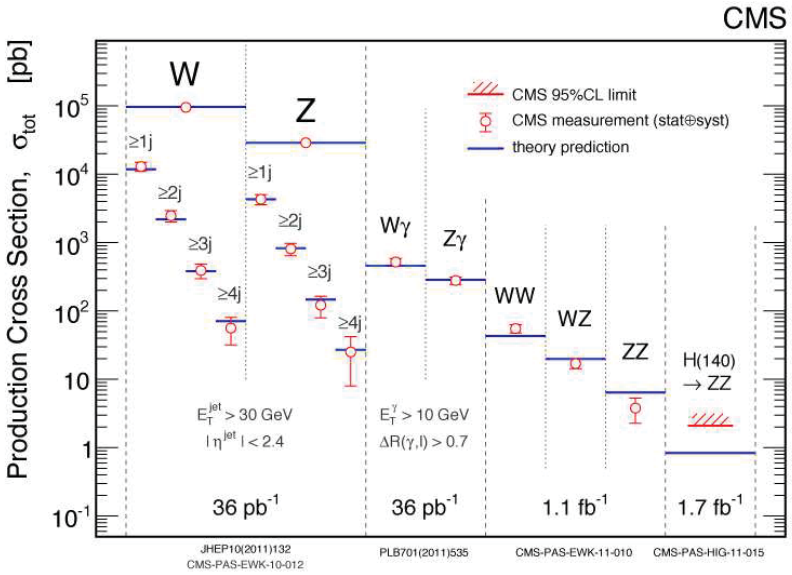

Figure 3.5: CMS precision tests of electroweak processes.

quark evidence has been obtained studying the strong $t\bar{t}$ production, whose cross section benefits from its steep increase with center-of-mass energy respect to lower energy colliders. The events are selected requiring high transverse momentum leptons or di-leptons, jets with at least 1 jet b-tagged and missing energy. As shown in Fig. 3.6 the measurements are in agreement with the most recent NLO and approximate NNLO predictions.

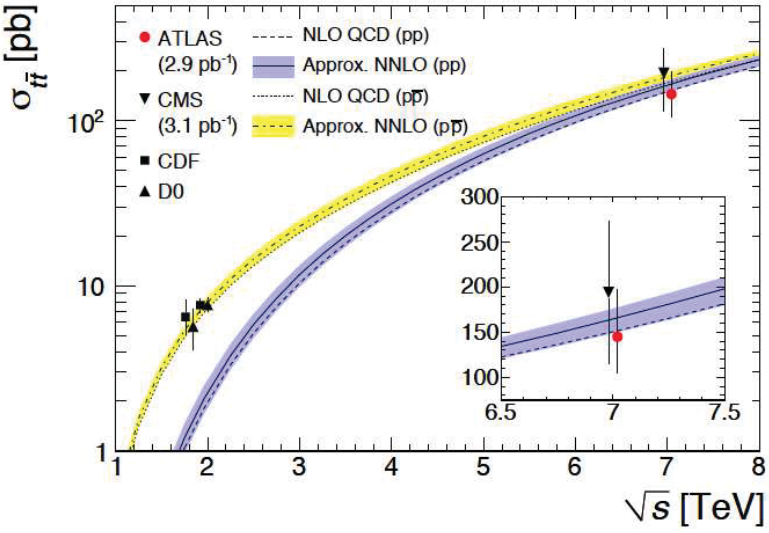

Figure 3.6: Top quark pair-production cross-section at hadron colliders as measured by CDF and D0 at Tevatron, CMS and ATLAS at LHC . The theoretical predictions for pp and $p\bar{p}$ collisions include the scale and parton density function uncertainties.

The complete mastering of all tools needed to reconstruct and understand top quarks at LHC has been successfully proven through the first measurement of single top pro-

duction cross section. Using only 36.1 pb^{-1} of LHC data, CMS experiment has been able to measure the single top production cross section in the t-channel as $\sigma_t = 83.6 \pm 29.8(stat + syst) \pm 3.3(lumi)$ pb, despite the tiny expected value and the presence of important backgrounds as W+jets and $t\bar{t}$ (more details in Sec. 4.6 and Chapters 5 and 6).

3.2.4 Higgs boson

The search for the Higgs Boson is one of the most ambitious goals of the LHC experiments. The direct lower limit on the Higgs boson mass comes from electron-positron collision data at LEP, and it is $m_H > 114.4$ GeV at 95% C.L.. Recent results from Tevatron with up to 6.7 fb^{-1} of $p\bar{p}$ data exclude also a mass window of $158 < m_H < 175$ GeV. The main modes for the Standard Model Higgs production at the proton-proton collider are gluon-gluon fusion, with a cross section form 1 to 10 pb for Higgs masses of 400 and 110 GeV (Fig. 3.7, left), while the main decay paths are $b\bar{b}$ and $\tau\tau$ below threshold for decay to vector boson pair, and WW and ZZ above (Fig. 3.7, right).

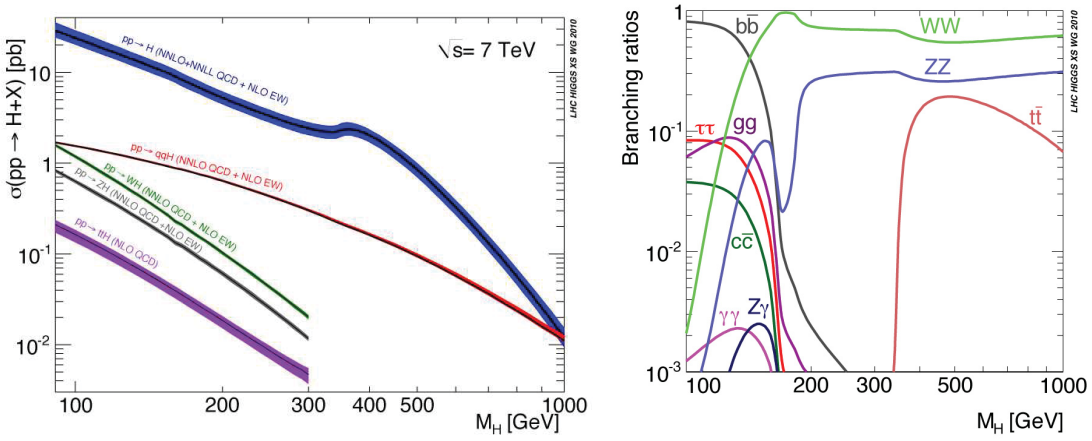

Figure 3.7: Standard Model Higgs boson production cross sections for 7 TeV pp collisions (left), and decay branching ratios (right).

The amount of data collected in 2010 at the LHC was not large enough to perform an exhaustive search that can yield, in general, to competitive results with respect to the Tevatron collider. Considering CMS as example, this was only possible, so far, for a couple of analysis: Standard Model Higgs in W^+W^-, whose cross section is enhanced by the presence of a fourth generation of quarks and supersymmetric Higgs (MSSM) decaying in τ pairs [19]. Since leptons originating from $H \to W^+W^-$ decays tend to have a relatively small opening angle, while those from WW backgrounds are preferentially emitted back-to-back, the angle between the two leptons, $\Delta\phi_{ll}$, is a variable with high discriminating power. No excess has been found above the Standard Model expectation, in the lower $\Delta\phi_{ll}$ region (Fig. 3.8, left) and so exclusion at 95% C.L. has been set for Higgs masses between 144 and 207 GeV.

The second analysis studies the τ pair decays of the neutral Higgs bosons, in a picture (the minimal supersymmetric extension to the Standard Model) with five massive Higgs

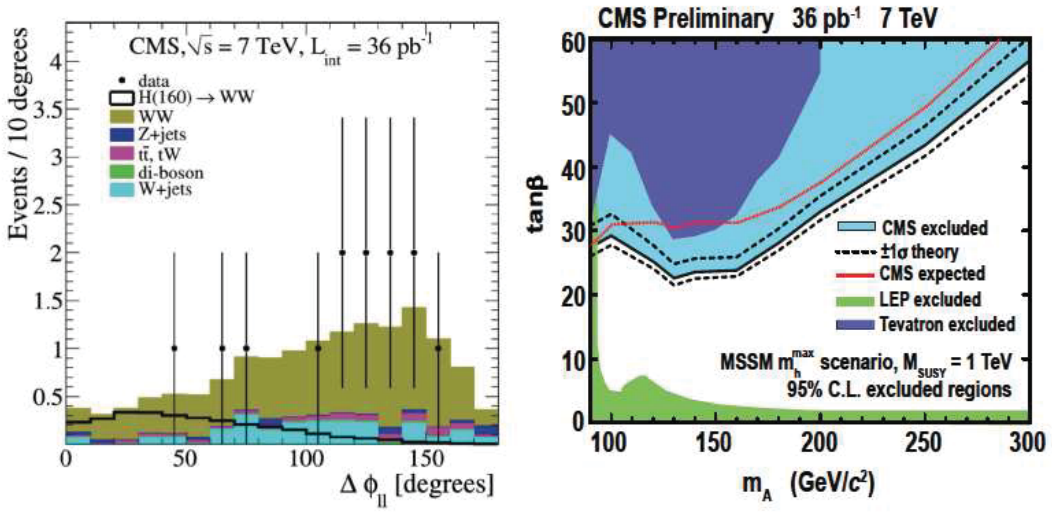

Figure 3.8: Distribution of the opening angle between the two leptons, $\Delta\phi_{ll}$, in WW event candidates (left). Exclusion limits on MSSM natural Higgs decaying to τ pairs (right).

particles. The observed τ pair mass spectrum reveals no evidence for neutral Higgs boson production and the results can be translated into exclusion regions in the MSSM parameter space (Fig. 3.8, right). Extrapolations considering the combined measurements in all decay channels from ATLAS and CMS, estimate that with 5-10 fb^{-1} (so already in the next months) we'll be able to definitely exclude or discover the Higgs boson in the mass range between 120 and 600 GeV. The most recent limits on the expected Higgs boson mass obtained using 1.0-2.3 fb^{-1} from combining CMS and ATLAS measurements are shown in Fig. 3.9.

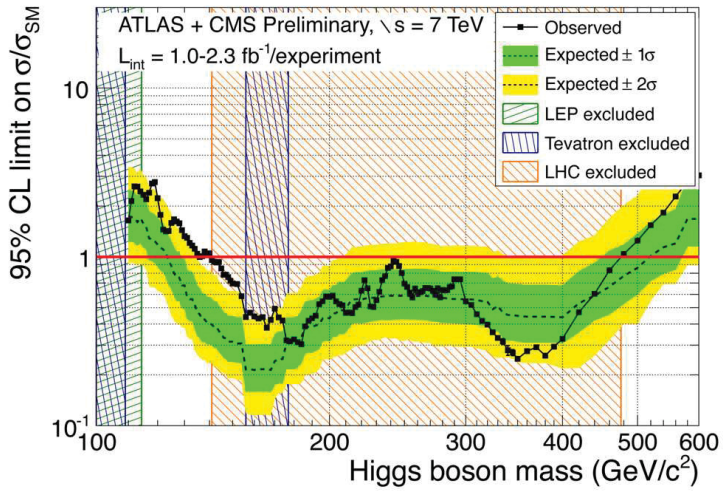

Figure 3.9: ATLAS and CMS combined limits on Higgs boson mass.

3.2.5 Beyond Standard Model theories

One of the theoretically favored theories beyond the Standard Model is supersymmetry [20, 21], being able to solve the hierarchy problem by the introduction of supersymmetric particles (called ”sparticles”) with the same quantum numbers as the SM particles, but differing by half a unit of spin. The dominant production channels of heavy colored sparticles at the LHC are squark-squark, squark-gluino and gluino-gluino pair production. These sparticles decay into quarks, gluons and other SM particles, as well as neutralinos which escape undetected, leading to final states with several hadronic jets and large missing transverse energy [22]. No excess with respect to the Standard Model predictions has been observed and consequently 95% C.L. limits on the parameter space of SUSY models have been set (Fig. 3.10). Based on the results obtained from the analysis performed, it has been extrapolated that, if supersymmetry is really a symmetry of nature, it would be definitely possible to detect SUSY signals with an amount of data 100 times larger than 2010 statistics. Since up to November 2011 LHC delivered ≈ 5 fb^{-1}, soon in the next months we'll have the answer to this meaningful and full of expectations question.

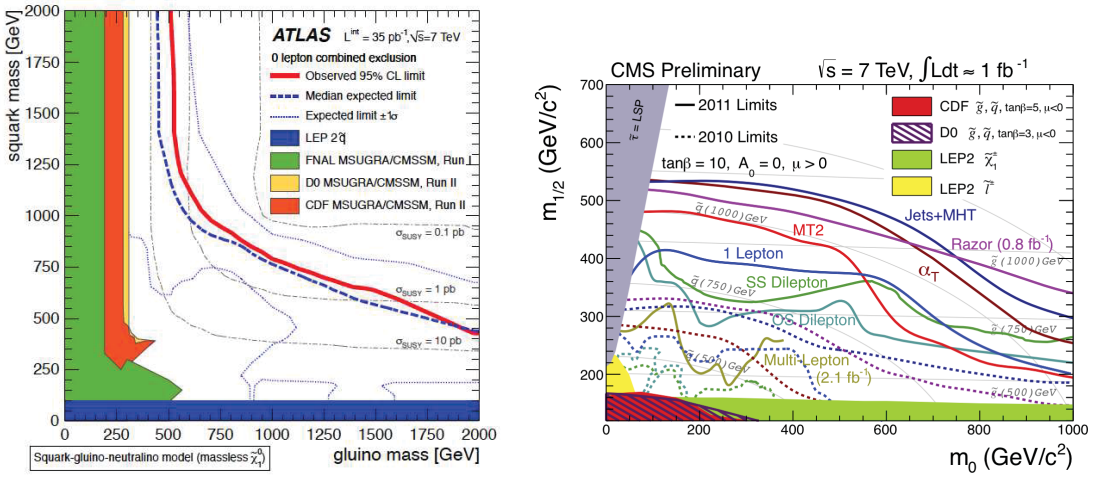

Figure 3.10: 95% C.L. exclusion limits in the (gluino, squark) mass plane for ATLAS experiment (a) and in the (m_0, $m_{1/2}$) mass plane for CMS experiment (b). m_0 and $m_{1/2}$ are the masses of the superparticles with spin 0 and 1/2, respectively.

Among the new physics searches at the LHC it's worth mention the search for quark compositeness and for new strongly coupled heavy bosons (W', Z') [23]. The first could be revealed through deviations from di-jets angular distribution as predicted by perturbative QCD, the second as data excess in the tails of reconstructed W transverse mass or Z invariant mass distributions (Fig. 3.11). Since no new physics signals have been observed, LHC established lower limits (at 95% C.L.) on contact interactions scale, W' and Z' masses. The values found for example by CMS are: $\Lambda = 5.6$ TeV, $M_{W'} = 1.58$ TeV and $M_{Z'} = 855$ GeV [24, 25, 26].

To conclude this part I want to mention the recent results on extra-dimensions and microscopic black holes searches. Extra-dimensions theories proposed to solve the hierarchy

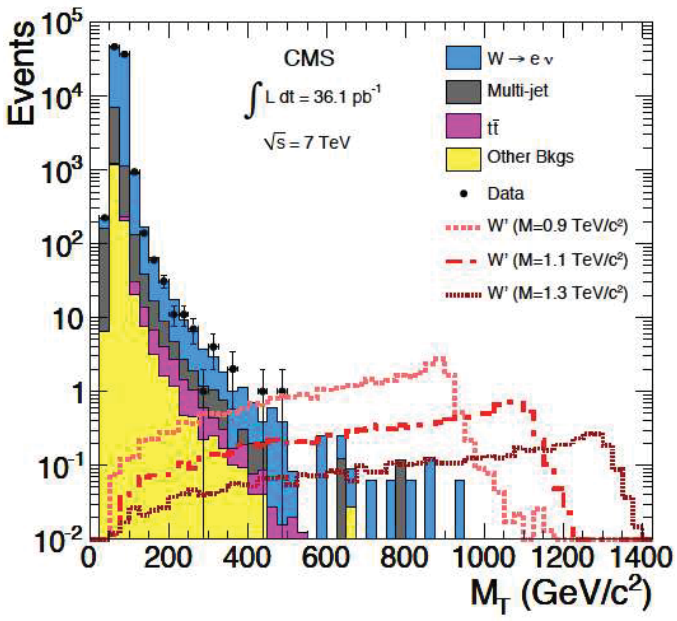

Figure 3.11: Transverse mass for $W \rightarrow e + \nu$ events.

problem assume a scenario where the SM is constrained to the common 3+1 space-time dimensions, while gravity is free to propagate through the entire multidimensional space. Because of this, the gravitational force is effectively diluted. The phenomenological effect would be the production of massive Kaluza-Klein graviton states, which decay into a di-photon final state [27]. So a search for large extra-dimensions could be performed looking for an excess of events in the high mass tail of the distribution of the di-photon invariant mass. In Fig. 3.12 (left) the results obtained by CMS are shown, which lead to graviton mass lower limits in the range 1.6 - 2.3 TeV (depending on the number of extra-dimensions hypothesized) and consequently to the most restrictive limits on the existence of large extra-dimensions to date (for dimensions greater than 6).

Another possible manifestation of the presence of compactified extra dimensions could be the production of microscopic black holes [28]. Once the partons colliding in LHC approach each other to a distance comparable to the size of extra-dimensions, they could feel the full strength of gravity and may collapse into a microscopic black hole. These black holes should then immediately evaporate emitting energetic quarks and gluons, as well as leptons, photons and W / Z bosons. In a recently published result [29], CMS searched for events with high multiplicity of energetic objects, studying the distribution of the variable, S_T defined as scalar sum of transverse momenta of most energetic particles (Fig. 3.12, right). CMS has been able to exclude black holes with the minimum masses between 3.5 and 4.5 TeV.

3.2.6 Heavy Ion Physics

At the end of 2010 proton-proton run, lead ions were collided in the LHC at a center-of-mass energy of $\sqrt{s_{NN}}$ = 2.76 TeV, this representing a significant boost in energy with

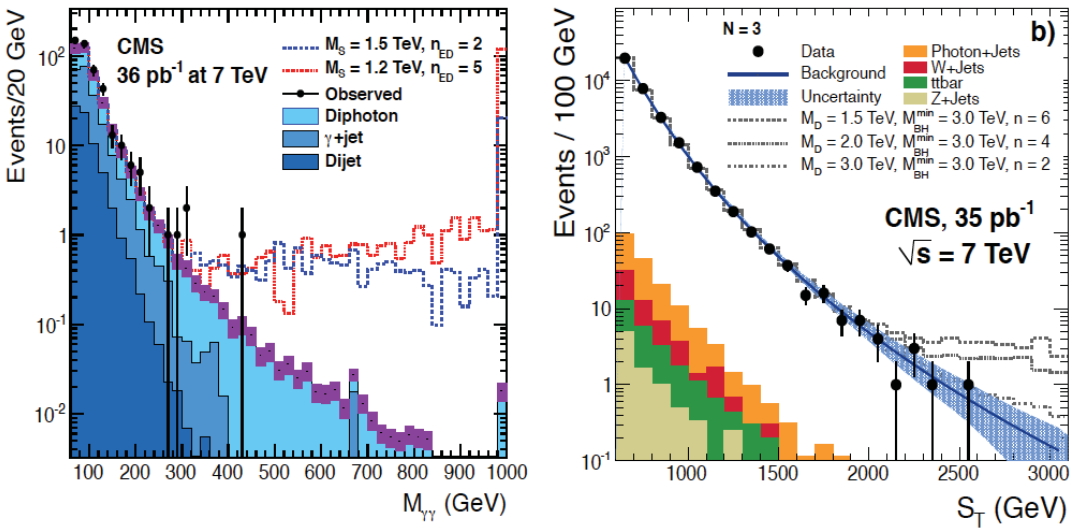

Figure 3.12: Invariant mass distribution of di-photon events with simulation of the excess foreseen in a couple of extra-dimensional models (left). Distribution of the variable S_T and simulation of the excess due to the production of microscopic black holes in different models (right).

respect to $\sqrt{s_{NN}}$ = 0.2 TeV at RHIC. The ALICE experiment at LHC is specialized on the investigation of heavy-ion collisions, but also ATLAS and CMS were expected to provide important complementary results. Apart from the first measurements performed by ALICE, i.e. the multiplicity density of primary charged particles and the charged particle elliptical flow in central rapidity region, two very interesting results have been obtained and confirmed by ATLAS and CMS experiments: jet quenching and the suppression of J/ψ production.

A measure of jet-quenching is the asymmetry in transverse energies of two jets $A_j = (E_{T_1} - E_{T_2})/(E_{T_1} + E_{T_2})$, for $\Delta\phi > \pi/2$. A deviation from asymmetry predicted in models like Hijing [30], which do not include jet-quenching effects, could indicate the formation of a very dense medium, the quark-gluon plasma, whose interactions make one of the jets lose a lot of energy. In Fig. 3.13 the results obtained by ATLAS and CMS are shown [31, 32]; confirmation of the observed phenomenon comes also from ALICE.

Lastly, the observation of J/ψ production suppression too is in total agreement with prediction of formation of dense media with colored constituents [33].

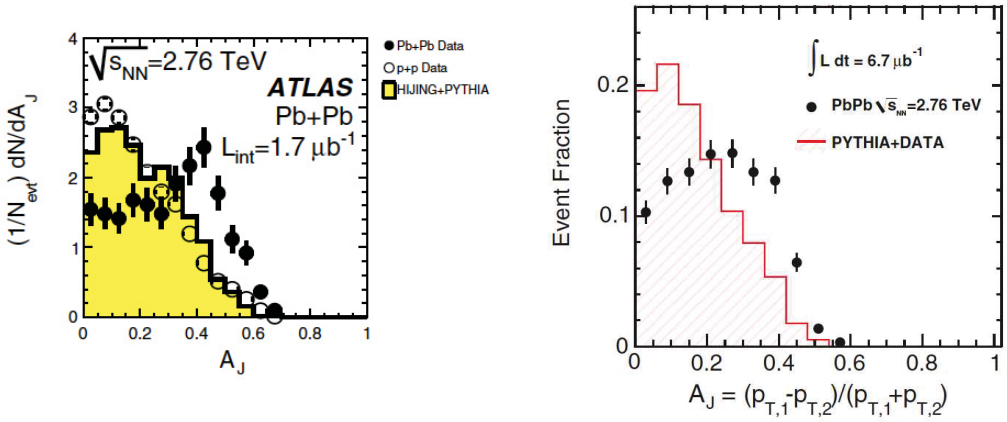

Figure 3.13: Measurement of the asymmetry in the transverse energy of two jets for the most central collisions, in ATLAS (a) and CMS (b).

Chapter 4

The Top Quark

4.1 Introduction

The top quark plays a special role in the Standard Model (SM) of particle physics and constitutes a very promising sector for new physics searches. This is supported by the following theoretical considerations:

- The top quark has the largest mass and Yukawa coupling among the elementary SM fermions. So, it is naturally related to the electroweak symmetry breaking and may reveal new strong dynamics.
- The quadratic divergence of the SM Higgs boson mass involves a top quark loop. For this reason it could be related to the new physics at Terascale, as in SUSY [34] and little Higgs [35] models, which should reestablish the naturalness of the EW theory.
- Thanks to the high mass, its decays in heavy states (as Wb, Zq, H^0q, etc.) are characterized by very large phase space.
- The top quark prompt decay offers the unique opportunity to explore the properties of a "bare quark", such as its spin and mass.

In this chapter, after an introduction on the top quark theoretical background in the Standard Model, the production (through strong and electroweak interactions) and decay modes will be discussed in detail. At the end, a section is dedicated to a historic overview over top quark searches in the past years, and recent results are presented.

4.2 Top quark in the Standard Model

In the SM, the top quark and its interactions may be described by the following lagrangian:

$$\mathcal{L}_{SM} = m_t\bar{t}t + \frac{m_t}{v}H\bar{t}t + g_s\bar{t}\gamma^\mu T^a t G^a_\mu + eQ_t\bar{t}\gamma^\mu t A_\mu + \frac{g}{\cos\theta_w}\bar{t}\gamma^\mu(g_V + g_A\gamma^5)tZ_\mu + \frac{g}{\sqrt{2}}\sum_q^{d,s,b} V_{tq}\bar{t}\gamma^\mu P_L q W^-_\mu + h.c. \tag{4.1}$$

where, in addition to the definitions given in Sec. 1.2 we introduce $g_V = T_3/2 - Q\sin^2\theta_W$ and $g_A = -T_3/2$; the $left$ projector P_L, which essentially choices the left component of the quark fields on its right; A_μ, Z_μ and $W^\pm_\mu$ which represents the physical photon, Z and W bosons fields obtained through a rotation of the gauge fields W^i_μ and B_μ with mixing angle θ_w ($\sin\theta_w \approx 0.23$). In detail $W^\pm_\mu = 1/2\sqrt{2}\ (W^1_\mu \pm W^2_\mu)$, $A_\mu = B_\mu\cos\theta_w + W^3_\mu\sin\theta_w$ and $Z_\mu = -B_\mu\sin\theta_w + W^3_\mu\cos\theta_w$. Furthermore the g and g' used in Eq. 1.4 are related to the electric charge e through the relation $g\sin\theta_w = g'\cos\theta_w = |e|$. Besides the well-determined gauge couplings at the electroweak scale, the recent estimations of the other parameters are listed in Tab. 4.1 [36] (these also include the recent results from Tevatron).

m_t (GeV)	$\lvert V_{tb}\rvert$	$\lvert V_{ts}\rvert$	$\lvert V_{td}\rvert$
173.2 ± 0.9	> 0.79	$(40.0 \pm 0.9) \times 10^{-3}$	$(8.5 \pm 0.3) \times 10^{-3}$

Table 4.1: Recent experimental values for the top quark parameters. The limit on V_{tb} is obtained imposing the constraint $|V_{tb}| < 1$.

A precise determination of the top quark mass is also important since it contributes significantly to the radiative one-loop corrections. Consider for example the one loop corrections to the electroweak gauge bosons mass (Fig. 4.1). The W mass, for example, could be written as

$$m^2_W = \frac{\frac{\pi\alpha}{\sqrt{2}G_F}}{\sin^2\theta_w(1-\Delta r)}, \tag{4.2}$$

where G_F is the fermi constant. Since both the top quark and the Higgs boson can contribute to the loop, the correction Δr can be expressed in the following form:

$$\Delta r = -\frac{3G_F m^2_t}{8\sqrt{2}\pi^2\tan^2\theta_w} + \frac{3G_F M^2_W}{8\sqrt{2}\pi^2}\left(\ln\frac{m^2_H}{M^2_Z} - \frac{5}{6}\right). \tag{4.3}$$

resulting in a relation between top and Higgs masses. In this relation m_t, M_W, M_Z, m_H are respectively the top, W, Z and Higgs masses. It is from the predicted radiative corrections that was obtained one of the first indirect estimations of the Higgs boson mass.

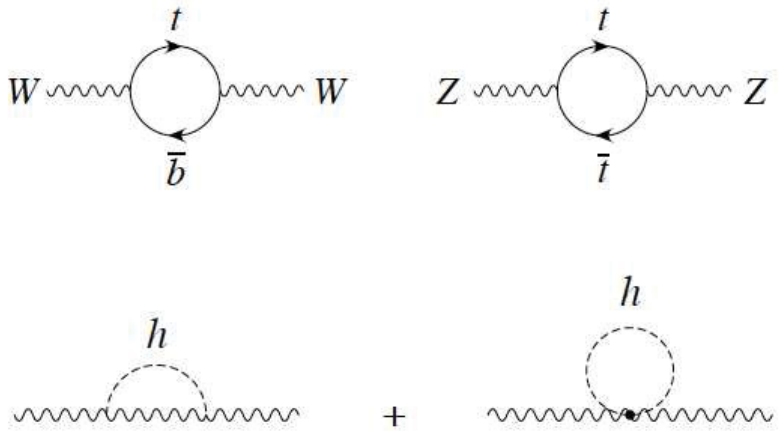

Figure 4.1: Virtual top quark and Higgs boson loops contribute to the W and Z masses.

4.3 Top quark decay

Due to the absence of the flavor-changing neutral currents at tree level in the SM, and having a mass above the Wb threshold, the decay width of the top quark could be written as:

$$\Gamma(t \to W^+ q) = \frac{|V_{tq}|^2 m_t^3}{16\pi v^2}\left(1 - \frac{M_W^2}{m_t^2}\right)^2\left(1 + 2\frac{M_W^2}{m_t^2}\right)\left[1 - \frac{2\alpha_s}{3\pi}\left(\frac{2\pi^2}{3} - \frac{5}{2}\right)\right] \tag{4.4}$$

where α_s is the QCD coupling constant and $q = d, s, b$. We can notice that since $|V_{tb}| \gg |V_{td}|$, $|V_{ts}|$, the decay is expected to be dominated by the two-body channel $t \to Wb$. Moreover this decay allows us to measure $|V_{tb}|$ while $|V_{td}|$ and $|V_{ts}|$ may not be practically measured via the top decay processes[1], evaluating the ratio:

$$\frac{B(t \to Wb)}{B(t \to Wq)} = \frac{|V_{tb}|^2}{|V_{td}|^2 + |V_{ts}|^2 + |V_{tb}|^2} \tag{4.5}$$

This relation allows to measure the absolute magnitude of $|V_{tb}|$ if we assume three generations of quarks (i.e. $|V_{td}|^2 + |V_{ts}|^2 + |V_{tb}|^2 = 1$). The way to measure $|V_{tb}|$ directly, with no assumptions about the number of generations, is to measure single top quark production via the weak interaction (see Sec. 5.6.2 and Sec. 6.7). However, the measurement of $|V_{tb}|$ at hadron colliders is challenging and represents an example of the coordinate effort that is often required to measure fundamental SM parameters, since it requires input from a variety of sources: deep-inelastic scattering (for the parton distribution functions), theory (for precise QCD calculations), and of course the actual experiment.

[1] $|V_{td}|$ may be determined indirectly from $B_d^0 \bar{B}_d^0$ mixing and $|V_{ts}|$ from $B_s^0 \bar{B}_s^0$ mixing.

The most important aspect of equation 4.4 is that:

$$\Gamma(t \to W^+ q) \approx 1.3\,\text{GeV} \approx \frac{1}{0.5 \times 10^{-24} s} > \Lambda_{QCD} \sim 200\,\text{MeV}. \tag{4.6}$$

implying that the top quark will promptly decay via weak interaction before hadronization and so before top-flavoured hadrons or $t\bar{t}$-quarkonium bound states can form. Thus the "bare quark" properties may be accessible for scrutiny.

4.4 Top quark strong production

The leading process for strong top quark production at the high energy interactions of a $p\bar{p}$ or pp collision at the Tevatron or LHC, respectively, is the open flavor pair production described by perturbative QCD. In this picture, a hard process between two hadrons is the result of an interaction between the quarks and gluons the incoming hadrons are constituted of. The description of the collision can be separated into a short distance (hard scattering) partonic cross section for the participating partons of type i and j, $\hat{\sigma}^{ij}$, and into long distance terms factored together in the parton distribution functions (PDFs) $f_i(x_i, \mu_F^2)$ (x_i is the hadron longitudinal momentum fraction carried by the parton i). The separation is called factorization of the interaction (Fig. 4.2) and is set by the factorization scale μ_F^2.

The hard process involves only high momentum transfer, is calculable with perturbative QCD and is almost insensitive to low momentum scale. The factorization is valid to all orders of the perturbative theory, getting weaker dependence on the arbitrary scale μ_F^2 as more perturbative terms are added in the expansion.

The parton distribution functions (PDFs) $f_i(x_i, \mu_F^2)$ can be interpreted as the probability density to observe the parton i with the longitudinal momentum fraction x_i, when the hadron is probed at a scale of μ_F^2. The PDFs can not be calculated in perturbative QCD, so are extracted by global fits from deep-inelastic scattering and other data. In Fig. 4.3 the PDFs are shown in the CTEQ [37] parameterization, for two different values of $Q^2 = \mu_F^2$ scales.

The total top quark pair production cross section for hard scattering processes, in pp or $p\bar{p}$ collisions at a centre of mass energy $\sqrt{s}$ can be written as:

$$\begin{aligned}\sigma^{t\bar{t}}(\sqrt{s}, m_t) = \sum_{i,j=q,\bar{q},g} \int dx_i dx_j f_i(x_i, \mu^2) \bar{f}_j(x_j, \mu^2) \\ \times \hat{\sigma}^{ij \to t\bar{t}}(\rho, m_t^2, x_i, x_j, \alpha_s(\mu^2), \mu^2).\end{aligned} \tag{4.7}$$

where $f_i(x_i, \mu^2)$ and $\bar{f}_j(x_j, \mu^2)$ are the PDFs for the proton and anti-proton, ij runs over all the parton pairs $q\bar{q}$, gg, qg and $\bar{q}g$, $\rho = 4m_t^2/\sqrt{\hat{s}}$ and $\hat{s} = x_i x_j s$.The scale μ^2 is commonly chosen to represent both the factorization and the renormalization scale (the last one is introduced during the renormalization procedure to remove the divergences arising in perturbative calculations). The corresponding Feynman diagrams at the leading

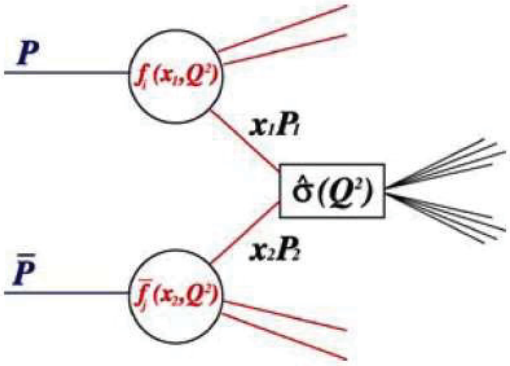

Figure 4.2: Parton model description of a hard process using the factorization approach.

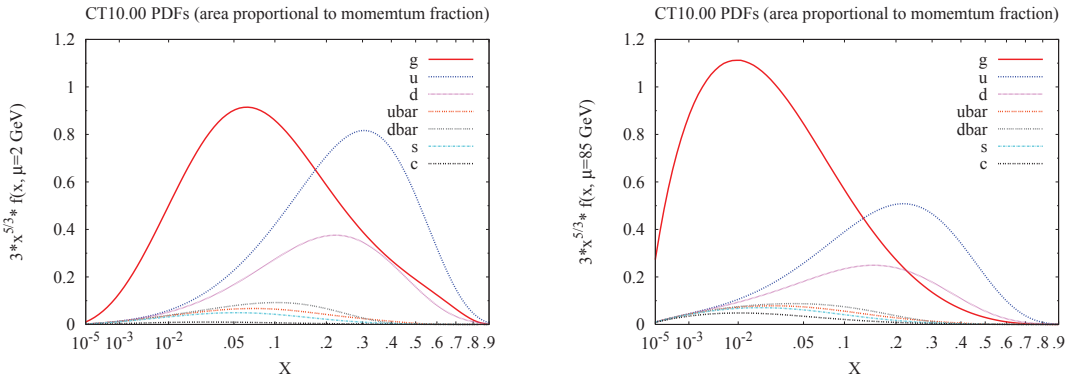

Figure 4.3: The quark, antiquark and gluon momentum densities as function of the fraction x of proton longitudinal momentum carried in the recent CT10 parameterization. Left: $Q^2 = (2\,\mathrm{GeV})^2$. Right: $Q^2 = (85\,\mathrm{GeV})^2$.

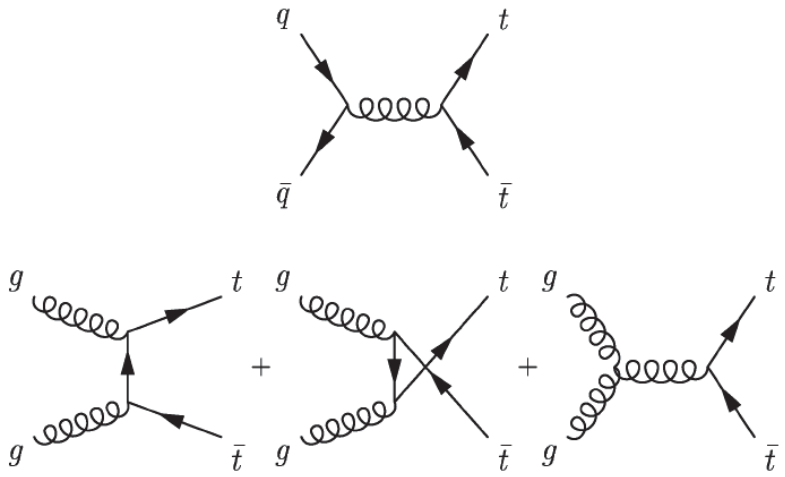

Figure 4.4: Top pair production at hadron colliders proceeds at lowest order through quark antiquark annihilation (*top*) and gluon fusion (*bottom*).

order are shown in Fig. 4.4.

The minimum $\hat{s}$ in the process is $4m_t^2$ and so $x_i x_j = \hat{s}/s \geqslant 4m_t^2/s$. Now, since the probability of finding a parton with fraction x decrease with increasing x, the typical value of $x_i x_j$ will be near the threshold for the $t\bar{t}$ production. That is, considering $x_i \approx x_j \equiv x$, $x \approx 2m_t/\sqrt{s}$ = 0.18 at Tevatron and = 0.025 at the LHC. Therefore, looking at PDFs in Fig. 4.3, we immediately understand why at Tevatron dominates the quark-antiquark annihilation while at LHC the gluon-gluon fusion. The top quark pair production cross section has been recently calculated at the NNLO (next-to-next-to-leading order) in QCD, including threshold resummations, by N. Kidonakis [38].

Table 4.2 summarizes the $t\bar{t}$ cross section calculations for Tevatron and LHC energies. The LHC is truly a "top factory", producing, at design energy and luminosity more than $\approx$ 1 top pair per second. An accurate evaluation of the production cross section is a necessary ingredient for the measurement of $|V_{tb}|$ since $t\bar{t}$ production is an important background to the electroweak single top production. Moreover, this cross section is also sensitive to new physics in top quark production and/or decay. A new source of top quarks (such as gluino production, followed by the decay $\tilde{g} \to t\bar{t}$) would appear as an enhancement of the cross section and a new decay mode (such as $t \to \tilde{t}\tilde{\chi}^0$) as a suppression. Finally, new resonances in $t\bar{t}$ production would both increase the top quark cross section and be visible as bumps in the system invariant mass distribution.

	$\sigma_{NNLO}(pb)$	$q\bar{q} \to t\bar{t}$	$gg \to t\bar{t}$
Tevatron ($\sqrt{s}$ = 1.96 TeV, $p\bar{p}$)	7.2	85%	15%
LHC ($\sqrt{s}$ = 14 TeV, pp)	894	10%	90%

Table 4.2: Cross sections, at next-to-next-to-leading order in QCD including gluon resummation corrections, for $t\bar{t}$ production via the strong interaction at the Tevatron and the LHC for $m_t = 173 GeV$.

4.5 Top quark electroweak production

The charged-current weak interaction, besides being responsible for the top quark decay, also significantly contributes to its production. The best way to study the properties of the Wtb vertex, and so to measure directly $|V_{tb}|$ at hadron colliders, is studying the single top electroweak production. The three classes of production processes are the following: Drell-Yan quark-antiquark annihilation or$s$-channel, Wb fusion or t-channel, which is similar to heavy-flavor production via charged-current deep-inelastic scattering, and associated tW production (Fig. 4.5).

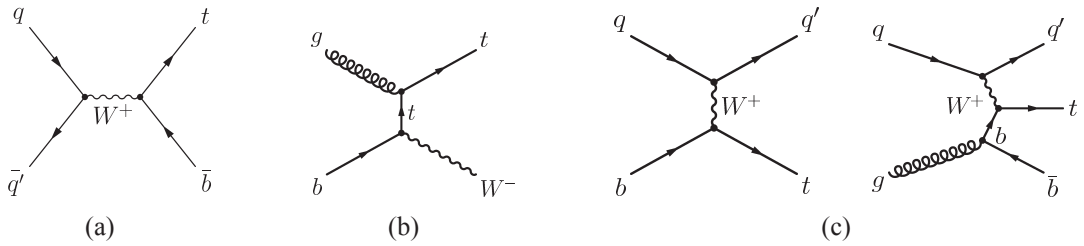

Figure 4.5: Leading order Feynman diagrams for single top quark production in s-channel (a), W-associated or tW (b), and t-channel production (c), the latter is shown in the LO description together with the dominating NLO diagram.

So far, the electroweak single top production has been observed at Tevatron in s- and t-channels and at LHC in tW- and t-channel (see Sec. 4.6). Calculations of fully-differential NNLO or NLO single top quark cross sections have been performed in [39, 40] and the results for Tevatron and LHC energies are shown in Tab. 4.3. We see the typical change of the production rate from the Tevatron to the LHC : a valence-induced process as s-channel is increased by about an order of magnitude, while the gluon or b-induced processes (t-channel) are enhanced by about a factor of 100.For its small cross section and the presence of large backgrounds the tW-channel has never been observed at Tevatron, as well as the s-channel has not yet been observed at the LHC .

	s-channel	tW production	t-channel
Tevatron ($\sqrt{s}$ = 1.96 TeV, $p\bar{p}$)	1.04	0.22	2.08
LHC ($\sqrt{s}$ = 7 TeV, pp)	4.59	15.6	63.2
LHC ($\sqrt{s}$ = 14 TeV, pp)	11.9	83.6	243

Table 4.3: Cross sections, at the next-to-leading order (for s-channel) or the next-to-next-to-leading order (for tW- and t-channels), for top quark production via the electroweak interaction, at the Tevatron and LHC, for $m_t = 173$ GeV.

In conclusion, the quark top sector is full of expectations for possible manifestation of new physics beyond the Standard Model. Interesting signatures include: decays into charged Higgs boson or decays through flavor changing neutral currents (in the SUSY or technicolor model); resonant $t\bar{t}$ production including among resonant states the Higgs boson, Kaluza- Klein excitation of gluons and gravitons, and technicolor states; $T\bar{T}$ or single T top quark partner production and decay in the Little Higgs model; multiple top

quarks and W' coming from theories of electroweak symmetry braking or an extended top quark sector.

4.6 Historic overview and recent results

The top quark, expected as the weak isospin partner of the b-quark discovered in 1977 at Fermilab, was searched for since 1979 at the e^+e^- colliders PETRA at DESY, at KEK, SLAC and LEP till 1990 (all searching for $e^+e^- \rightarrow t\bar{t}$). They didn't find any signal and set a lower limit on the top quark mass (45.8 GeV at SLAC [41] and LEP [42]). In the eighties the search was also brought by the hadron colliders at CERN ($Sp\bar{p}S$ up to $\sqrt{s} = 630$ GeV) and at Fermilab (Tevatron, $\sqrt{s} = 1.8$ TeV). The dominant mechanism for the production of top quarks was expected to be the production of W bosons with subsequent decay $W \rightarrow tb$ for a top mass up to 77 GeV, while it was the pair production with subsequent decay $t \rightarrow Wb$ for a higher top mass. In 1989 the $Sp\bar{p}S$ set lower limits to the top mass up to 69 GeV [43], but as soon as CDF at Tevatron began the data taking, in 1989, this limit was immediately overcome. In 1992, when the D0 experiment was commissioned, the lower limit was 91 GeV [44]. After some improvements and higher precision measurements of the top production cross section, in 1995 both CDF and D0 published the discovery of the top quark in strong $t\bar{t}$ production [45], marking the begin of a new era, moving on from searches to studies of top quark properties and back again to new physics searches in the top quark sector.

The Tevatron has recently published results on top production cross section, mass and properties precise measurements. In Fig. 4.6 it is shown the $t\bar{t}$ cross section measurement performed by D0 [46] and the top mass measurement combination of D0 and CDF results [47]. The mass of the top quark is known with a relative precision of 0.54%, and for the first time the total uncertainty of the combination is below 1 GeV. With the current level of precision, the exact renormalization scheme definition corresponding to the current top mass measurements could be studied theoretically in more detail. Among other interesting measurements it's worth quoting the top-antitop mass difference, the top quark width, the first evidence of spin correlation in top decay products, the W boson helicity and the forward-backward asymmetry in $t\bar{t}$ production.

With increasing statistics the LHC is becoming competitive with Tevatron, even if some measurements are not yet as precise as Tevatron ones. This is the case, for example, for the top mass shown in Fig. 4.7 [48], while for the $t\bar{t}$ cross section the measurement performed by CMS and ATLAS is already very precise (Fig. 4.8) [49]. At the LHC also the top quark properties are studied, especially to find evidence of new physics beyond the Standard Model. Measurements of top quark charge, search for FCNC, top-antitop mass differences (important for testing the CPT symmetry) need more statistics to be able to unveil new phenomena in top quark sector. However, recently published by CMS , the most precise measurement to date of the top-antitop mass difference is [50]:

$$\Delta m_t^{measured} = m_t - m_{\bar{t}} = -1.20 \pm 1.21(stat.) \pm 0.47(syst.) \text{ GeV}/c^2 \qquad (4.8)$$

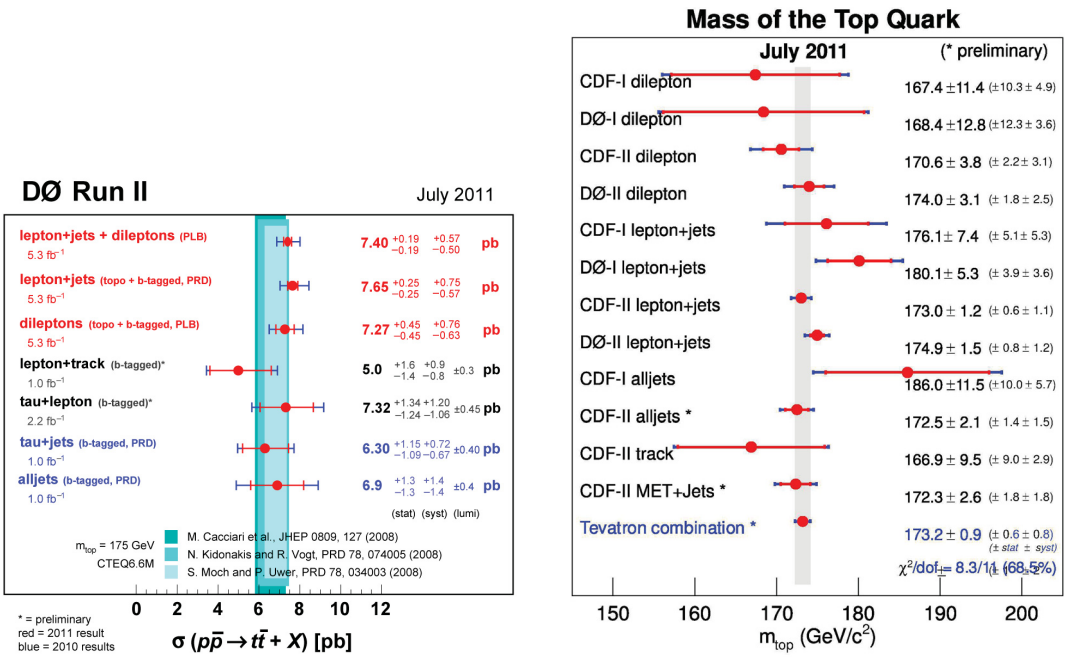

Figure 4.6: $t\bar{t}$ production cross section measured by D0 experiment (a) and Tevatron top mass measurement combination (b).

As far as the single top quark production is concerned, it was only in 2009 that there was the first claim for observation in t- and s-channels together at Tevatron [51] (with observation in the t-channel alone in 2011), and in the middle 2010 the first evidence of the t-channel production in CMS at LHC [52] (and observation in the t-channel with the ATLAS detector in 2011 [55]).

The most recent results published by Tevatron are shown in Fig. 4.9. The t- and s-channel cross section measurements are the most precise ones up to now, with a cross section of $\sigma(t\text{-ch}) = 2.90 \pm 0.59$ pb [53] and $\sigma(s\text{-ch}) = 1.8^{+0.7}_{-0.5}$ pb [54] respectively, and a significance higher than 5σ and higher than 3σ respectively. In Fig. 4.10 are also shown the latest results on the measurement of CKM V_{tb} element, for the D0 collaboration.

At the LHC, the most recent result on t-channel published by ATLAS is shown in Fig. 4.11. With 0.7 fb^{-1} of 2011 LHC collision data they find a cross section of $\sigma(\text{cut}) = 90 \pm 9^{+31}_{-20}$ pb and $\sigma(\text{NN}) = 105 \pm 7^{+36}_{-30}$ pb for a simple cut and count analysis and a more complex, neural network based analysis respectively. All the measurements in the t-channel are perfectly in agreement with each other taking into account the evolution of single top cross section from Tevatron to LHC, Fig. 4.12.

An other interesting recent result obtained at LHC is the challenging measurement of single top tW-production. The huge backgrounds and low production cross section led to a measurement with 2.1 fb^{-1} in CMS [56] which is 2.7 σ far from the background-only hypothesis $\sigma(tW\text{-chan}) = 22^{+9}_{-7}$ pb (Fig. 4.13). Extrapolations show that with a simple cut and count analysis like the past one the signal significance is quite saturating with

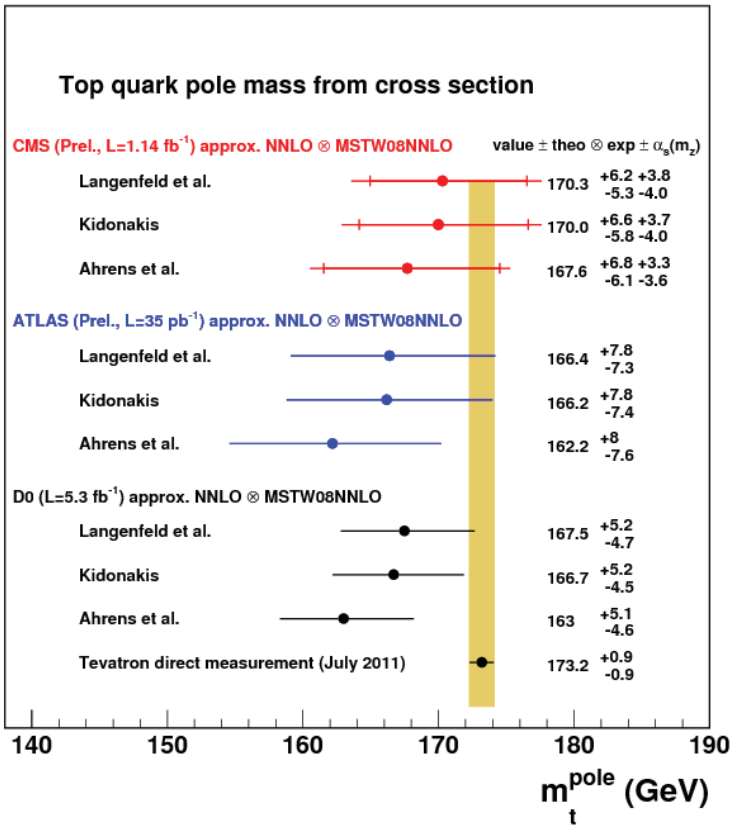

Figure 4.7: Comparison between top mass measurements at LHC and Tevatron.

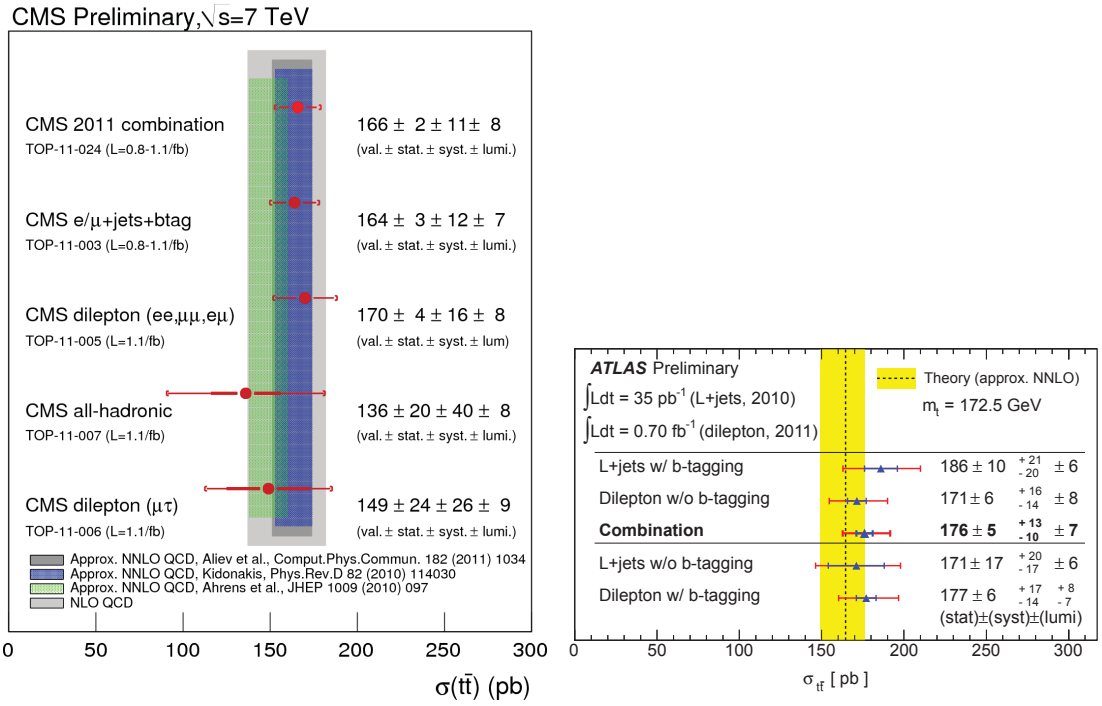

Figure 4.8: $t\bar{t}$ production cross section measured by CMS (a) and ATLAS (b).

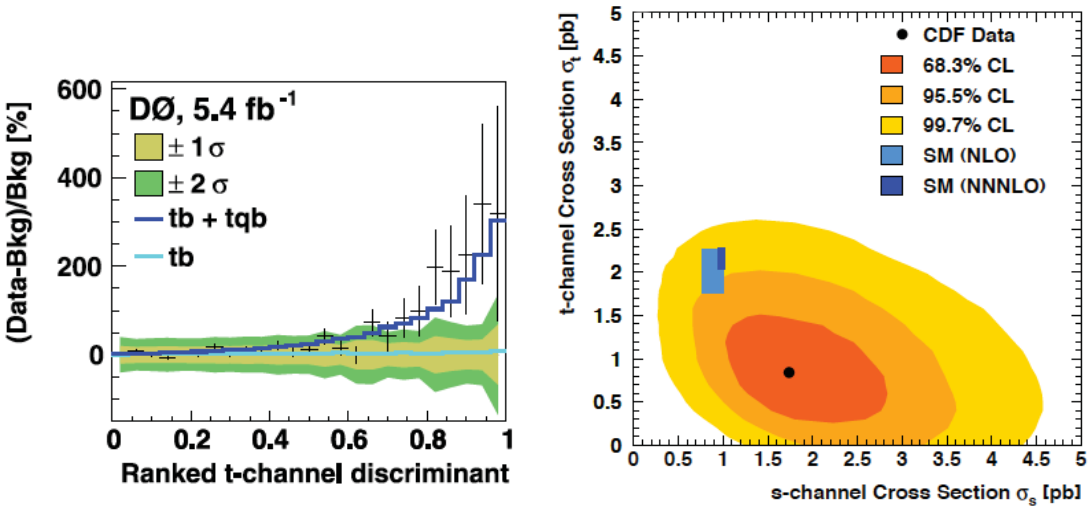

Figure 4.9: t-channel cross section measurement by D0 (a) and scatter plot for t,s-channel measurements in CDF (b).

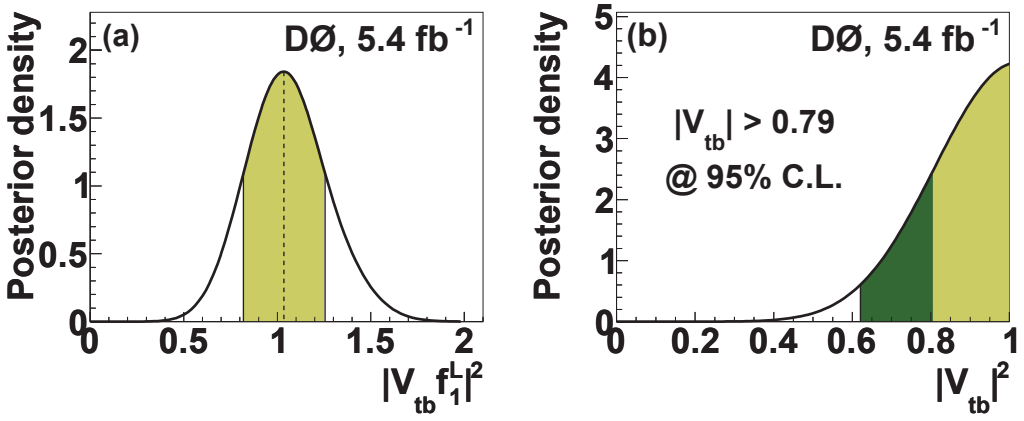

Figure 4.10: V_{tb} measurement in D0 with two different methods: without assuming the unitarity of the CKM matrix (a) or assuming the unitarity and giving a lower limit for V_{tb} (b).

luminosity, and reaches the 3 σ only with more than 10 fb^{-1}. So new strategies have to be set up in order to gain the much possible from the statistics available.

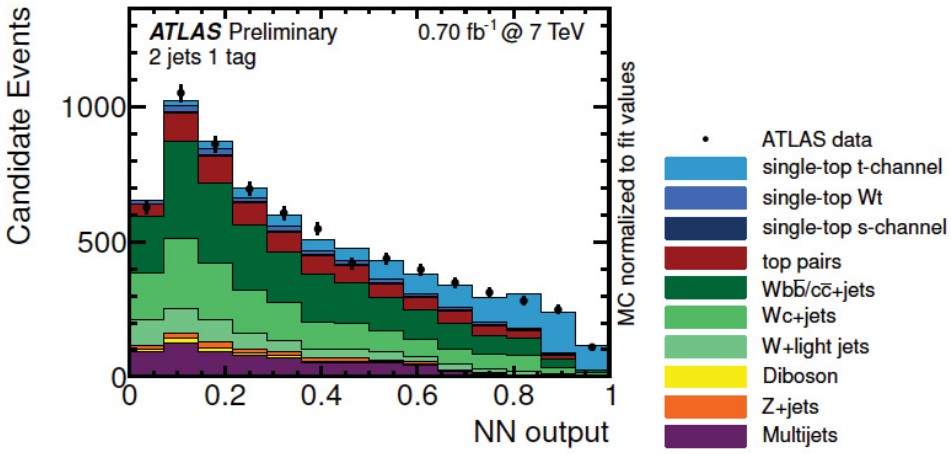

Figure 4.11: Neural network output distribution for the ATLAS measurement of the signal top t-channel production cross section.

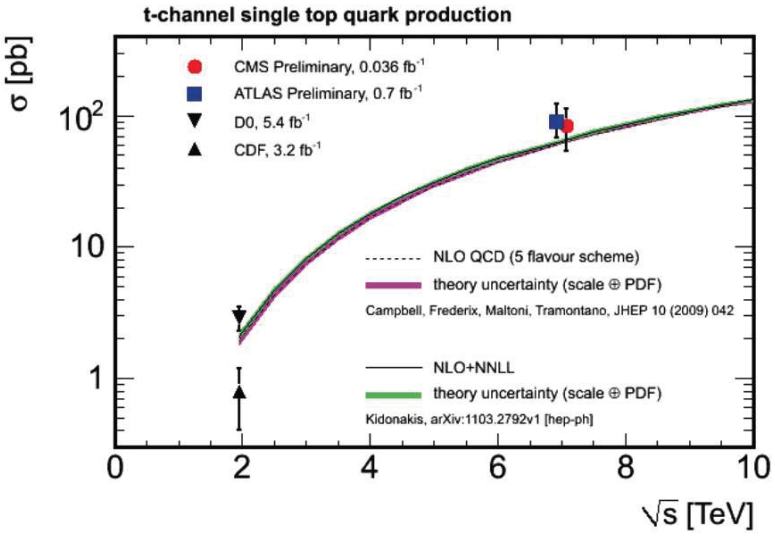

Figure 4.12: Single top t-channel production cross sections as measured by Tevatron and LHC and NLO,NNLL theoretical predictions.

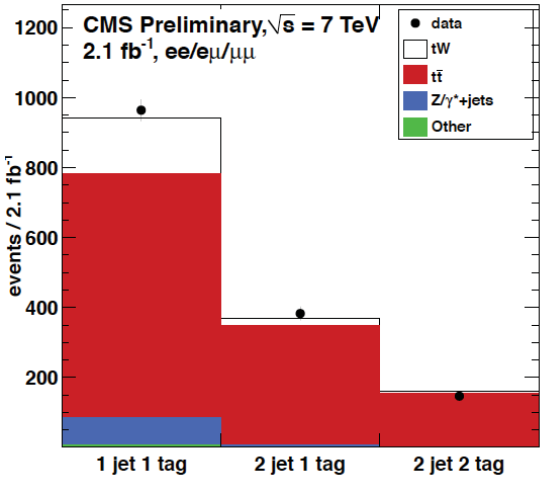

Figure 4.13: Event yields in data and simulation in the signal region (where two jets are required, one of which is a b-tagged jet) and the two $t\bar{t}$-enriched control regions for the CMS measurement of the signal top tW-channel production cross section.

Chapter 5

Single top t-channel cross section measurement with 2010 data

5.1 Introduction

In this chapter it is presented the measure of the single top t-channel cross section in the decay channel $t \to bW \to bl\nu$ ($\mathcal{B}$ = 0.1080). This measure has been performed analyzing 36.1 pb^{-1} collected by CMS during the 2010 data taking. The topology of the process and the spin correlations between the particles involved allow to perform a very tight selection, rejecting the large part of backgrounds. In particular, the two most important variables coming into the picture are the pseudorapidity of the jet produced with top quark, η_{lj} (quantity related to the angle between the beam direction and this jet) and the cosine of the angle between the lepton and the jet in the top rest frame, $\cos\theta^*_{lj}$. The signal extraction is obtained from a fit to the above mentioned variables, using as signal and background fit functions the distributions taken either from simulation or from data-driven estimations (template-fit). In the end, several sources of systematic uncertainties has been taken into account, and the statistical significance of the measurement has been evaluated.

The first part is dedicated to the event selection and the Monte Carlo simulation of the main background and signal processes. Then the data-driven techniques for QCD and W+light jets background estimation will be illustrated. Afterwards the two variable (2D) fit method and the statistical evaluation are presented, and in the end there is the description of systematic uncertainties and the final results obtained.

5.2 Samples and Event Selection

5.2.1 Data and Monte Carlo samples

The dataset used in this analysis, corresponding to a luminosity of 36.1 pb^{-1} known with 4% [57] uncertainty, makes use of the whole 2010 statistics (43.2 pb^{-1}) excluding those runs flagged as bad by the Data Quality Monitoring (DQM) or by the Physics Performance Group (DPG). In fact, the single top signature requires reconstruction of

physical objects in all parts of the CMS detector (muon system, calorimeters, forward detectors, etc.).

Monte Carlo simulations of the signal and of the main backgrounds are used, including the simulation of the full detector response which is based on the software GEANT 4. The t-channel events are simulated with the MadGraph event generator and then normalized to the NLO cross section 62.7 pb times $3 \cdot \mathcal{B}(t \rightarrow l\nu b)$ since only leptonic decays are simulated. The several backgrounds taken into account are summarized in table 5.1 with the respective cross sections.

It's worth saying that certain degree of double counting coming from the use together of W + jets, $VQ\bar{Q}$ and Wc is avoided by using a particular tool that separates the different parton flavours associated to the jets at the Monte Carlo Truth (generator) level [58] and splits these samples in three categories: $Wb\bar{b}$, $Wc\bar{c}$, W + light partons, excluding Wc which is taken from a dedicated sample. The whole W background will be also referred to as W+light flavours or partons (u, d, s, g) and W + heavy flavours or partons (c, b). In more detail the events where there are two jets associated to c, b partons from the Matrix Element (ME) are taken from the $VQ\bar{Q}$ ($Q = c, b$) MC sample. The events where there are two jets associated to c, b partons from Parton Shower (PS) are taken from the W + jets MC sample. Events with one jet associated to a c quark are taken from the Wc sample if the c quark comes from the ME, and from the W + jets sample if the c quark comes from the PS. The W + light flavor events are entirely extracted from the W + jets sample, vetoing all the heavy flavor components.

A simultaneous extraction of $t\bar{t}$ and of its main background [59] suggests the following scale factors:

$$SF(VQ\bar{Q}) = 2 \pm 1 \quad (5.1)$$

$$SF(Wc) = 1^{+1}_{-0.5} \quad (5.2)$$

5.2.2 Event selection

The events selection is optimized for the final state topology of the t-channel production (see Fig. 4.5 (c)), which is characterized by

- one charged lepton with high transverse momentum and high missing transverse energy coming from escaping neutrino. Both come form the W boson decay stemming in turn form top quark decay;
- one b-flavoured jet with high transverse momentum coming from the hadronization of the b-quark from top decay;
- one low energy b-jet coming from gluon splitting in the NLO process for top production;
- one light jet coming from the hadronization of the light quark recoiling against the massive top quark. As a peculiar feature of the t-channel production, this jet

Process	$\sigma[\mathrm{pb}] \cdot BR$
single top, t channel $(W \to l\nu, l = e, \mu, \tau)$	20.9 (NLO)
single top, s channel $(W \to l\nu, l = e, \mu, \tau)$	1.5 (NNLL)
single top, tW channel (inclusive)	10.6 (NLO)
$t\bar{t}$	165 (NNLL)
$W(\to l\nu) + jets$	31314 (NNLO) †
$W(\to l\nu) + c(+jets)$	3628 (NLO) †, ⋄
$Z/\gamma^*(\to l^+l^-) + jets$ (*)	3048 (NNLO) †
$V(\to l\nu, l^+l^-) + Q\bar{Q}(+jets)$ (**)	35.8 (LO) †, ⋄
WW	43 (NLO)
WZ	18.2 (NLO)
ZZ	5.9 (NLO)
$b/c \to e$, $20 < \hat{p}_T < 30$ GeV	132160 (LO)
$b/c \to e$, $30 < \hat{p}_T < 80$ GeV	136804 (LO)
$b/c \to e$, $80 < \hat{p}_T < 170$ GeV	9360 (LO)
EM-enriched QCD, $20 < \hat{p}_T < 30$ GeV	2454400 (LO)
EM-enriched QCD, $30 < \hat{p}_T < 80$ GeV	3866200 (LO)
EM-enriched QCD, $80 < \hat{p}_T < 170$ GeV	139500 (LO)
γ+jets, $40 < H_T < 100$ GeV	23620 (LO)
γ+jets, $100 < H_T < 200$ GeV	3476 (LO)
γ+jets, $H_T > 200$ GeV	485 (LO)

(*) $m_{ll} > 50$ GeV
(**) $V = W, Z; Q = b, c$
† separated into sub-processes with the technique described in the text
⋄ further multiplied by the scale factors from Ref. [59], see text

Table 5.1: Monte Carlo datasets used in this analysis. The samples are generated either inclusively or with a final state restricted to the leptonic mode, including electrons, muons, and taus.

is produced forward in the collisions, that means at low angle with respect to the beam axis and so with high pseudorapidity values.

Therefore, to enrich the data sample in signal events it is required exactly one lepton (electron in this analysis), one b-jet, and and one light flavoured jet. The lepton selection criteria and the quality cuts for central jets are taken equal to those agreed for $t\bar{t}$ analyses in single-electron channels [60].

The main backgrounds faking the signal of interest are W + jets and $t\bar{t}$ events.

W + jets, and in particular W + heavy flavours background, where the W decays in leptons is strongly reduced by the 2 jets requirement (since its cross section decreases by a factor $\approx 1/\alpha_S \approx 1/10$ for each increase of the number of jets associated). W + light partons is further on suppressed requiring that one of the two jets is a b-jet.

The $t\bar{t}$ background obviously has a topology similar to our signal, especially when one top quark decays leptonically ($t \to bl\nu$) and the other in hadronic modes. Whatever the decay modes are, these events are characterized by the presence of two b-jets stemming from top decay. So, the requirement that the jet not b-tagged should not be b-flavoured (imposing the so called b-veto) helps in reducing this background.

An other dangerous background that has to be taken under control for its very high production cross section is the hadronic multi-jet production in which an electron is present (called QCD background). In these processes the lepton could come from the decay of b and c quarks, from the decay of long-lived hadrons, or from γ + jets events. The tight lepton selection and the quality criteria on the two jets (as the high transverse momentum requirement) cut down this background very much. An ulterior strong suppression is obtained cutting on the reconstructed W transverse mass which sharply separates the QCD background from the processes where a W boson is produced (as the single top channels, $t\bar{t}$, W + jets).

In the following we go into details of each selection step.

Primary vertex, noise cleaning an trigger selections

As first step of the selection at least one primary vertex is required to be reconstructed from at least 4 tracks with $|z_PV| < 24$ cm and $r_PV < 2$ cm. As a further cleaning step, we reject events with very high energy anomalous noise in the HCAL using a different algorithms, either based on the HCAL only or by using coincidence with the ECAL [61]. The single-electron triggers are used, differing from one data taking period to an other, choosing for each period the trigger with the lowest p_T threshold which is unprescaled and is not defined by a quality selection that can bias the background estimation. The trigger requirement is not applied on Monte Carlo samples because many of them were not foreseen at the time of their production and so it is preferred to use a scale factor extracted form data [62].

Electrons

Reconstructed electrons with a transverse energy $E_T > 30$ GeV within $|\eta| < 2.5$ are selected. We exclude the ECAL barrel-endcap transition region ($|\eta|$ of the supercluster between 1.4442 and 1.5660). Further selection is achieved by requiring absolute 2D impact parameter smaller than 0.02 cm with respect to the center of the estimated beam spot position; a distance of less than 1 cm between the z coordinates of the leading primary vertex[1] and of the electron track at the point of closest approach; no missed inner layers; quality cuts, which provide electron identification (ID) criteria, photon-conversion veto and electron isolation at the 70% efficiency working point [63]. This efficiency refers to the fraction of electrons in simulated W events passing these quality cuts after demanding a 25 GeV cut in the electron E_{T}. We define the "relative isolation" (I_{rel}) of a lepton as

$$I_{\mathrm{rel}} = \frac{I_{tk} + I_{calo}}{p_T} \,, \tag{5.3}$$

where I_{tk} (I_{calo}) is the sum of the transverse momenta (transverse energies) of the tracks (ECAL and HCAL deposits) in a cone of size $\Delta R < 0.3$ around the lepton direction, excluding the track (calorimetric footprint) of the lepton itself. ΔR is defined as $\sqrt{\Delta\eta^2 + \Delta\phi^2}$. Tight electrons are selected by the requirement $I_{\mathrm{rel}} < 0.1$. We give also a definition of loose electrons, selected requiring $E_T > 15$ GeV, $|\eta| < 2.5$, and $I_{\mathrm{rel}} < 0.2$.

It is required the presence of exactly one tight electron, vetoing events with additional loose electrons (to reduce contribution of dilepton events, which can come from $t\bar{t}$ or Drell-Yan processes). Moreover, a Z veto is applied, rejecting events where an additional candidate electron forms with the tight electron an invariant mass within the window 76-106 $\mathrm{GeV/c^2}$, has $E_T > 20$ GeV/c, $|\eta| < 2.5$ (excluding the ECAL barrel-endcap transition region as in the tight electron case), $I_{\mathrm{rel}} < 1.0$, and passes the 95% efficiency working point.

Jets

Jets are reconstructed using the anti-k_T algorithm [64] with a cone size of 0.5, using the particle flow algorithm (PF) which is described in detail in Ref. [65]. Briefly it reconstructs and identifies all the physics objects in the event (leptons, photons, hadrons) with a combination of the information from all CMS subdetectors. The redundancy of information allows an optimal determination of the particles direction, energy and type, as well as it reduces the systematic uncertainties and experimental biasses.

The jet energy is scaled by a factor that describes the detector response depending on the transverse energy and the pseudo-rapidity of the jet [66]. We consider only jets whose calibrated transverse momentum is larger than 30 GeV/c, within $|\eta| < 5$. PF jets must have more than one constituent, and if central they must have neutral hadronic, charged electro-magnetic, and neutral electro-magnetic energy fractions smaller

[1] If more than one primary vertex is identified, the one with largest sum of the squared transverse momenta of associated tracks is taken.

than 99%, charged hadronic energy fraction larger than 1% and charged particle multiplicity larger than 0. Furthermore, jets are ignored if they are within $\Delta R < 0.3$ of a tight electron candidate (definition given above apart from the requirements on the number of missed hits and photon-conversion veto). Fig. 5.1 shows the jet multiplicity after the lepton selection, in data and Monte Carlo. As we can see, at this stage of selection the sample is dominated by $W+$ light jets at low multiplicity and $t\bar{t}$ for higher jet multiplicity. The signal sample peaks at 2 jets bin; for this reason we require exactly two jets with the quality criteria above mentioned.

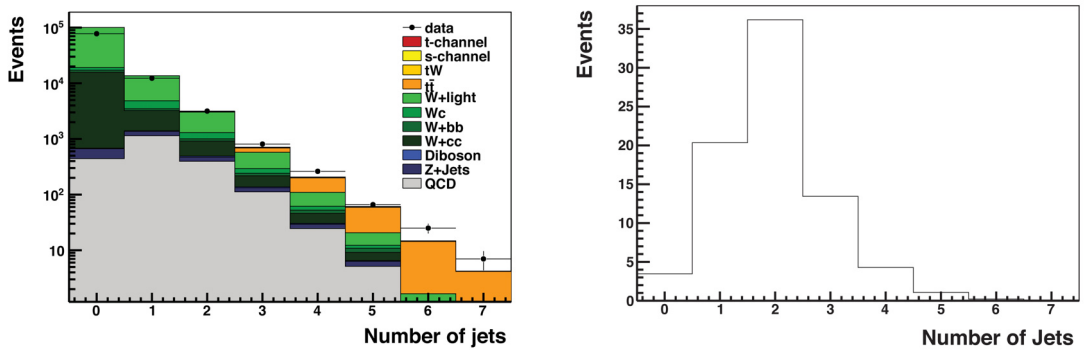

(a) (b)

Figure 5.1: Jet multiplicity after the lepton counting in data and Monte Carlo and for simulated signal events only. Here, and in the following figures, "QCD" is a short-hand notation for multi-jet QCD, $Q = c/b$, and "light" is short-hand for light partons.

Among the several b-tagging algorithms available, some exploiting the long B-hadrons lifetime, others their semi-leptonic decay modes or other else using kinematic variables related to the B meson mass, the "track counting" algorithm was chosen, both in the "high purity" (TCHP) and the "high efficiency" (TCHE) versions. This algorithm makes use of the signed 3D impact parameter significance (IP/σ_{IP}) of all the tracks associated to the jet that pass tight quality criteria, and outputs as jet discriminator the value of IP/σ_{IP} for the second ("high efficiency" version) or the third ("high purity" version) track, ordered by decreasing values of this observable. We indicate the discriminator values in the two versions as D_{TCHP} and D_{TCHE}.

Of the two jets passing selection criteria, exactly one is required to be b-tagged using the tight working point that corresponds to using the high purity algorithm with threshold set to 3.41 (TCHPT). So we require that only one jet has $D_{TCHP} > 3.41$. A looser definition of b-tagged jet is also given, using the loose working point for the track counting algorithm, which requires a threshold of 1.7 on the high-efficiency tagger (TCHEL). As further request we apply a b-veto cut, rejecting events in which the jet which fails the tight b-tagging selection passes the loose one, i.e. has $D_{TCHP} < 3.41$, but $D_{TCHE} > 1.7$. These working points are proposed by the b-tagging physics object group (POG) [80].

The reason for these b-tagging and b-veto choices is motivated by the following argument: as shown in Fig. 4.5(a) and already discussed, the signature of the t-channel single top production includes 3 partons in the final state. One light quark recoiling against the virtual W boson, one b quark from the top quark decay, and a second b quark from the

initial gluon splitting. Since the second b quark is most likely produced at very high rapidities, i.e., outside the tracker acceptance of $|\eta| < 2.5$ and thus not allowing b-tagging to be performed, we expect most signal events to have only one b-tagged jet. The advantage of sticking to these reference points lies mostly in the fact that the data/MC scale factors (and corresponding uncertainties) on efficiencies and mistag rates have been evaluated elsewhere [80].

In simulated signal events with one identified lepton and two jets, using the tight (loose) working point, we find an efficiency of 43% (62%) for jets matched to b quarks within $\Delta R < 0.3$, with $p_T > 30$ GeV and within the tracker acceptance (i.e., $|\eta| < 2.5$).

The b-tagged jet multiplicity in events with two jets is shown in Fig. 5.2 for data and Monte Carlo. The contribution of processes without b quarks in the final state is suppressed in the 1-tag bin, while in the same bin the signal is enhanced. The 2-tag bin instead is dominated by $t\bar{t}$.

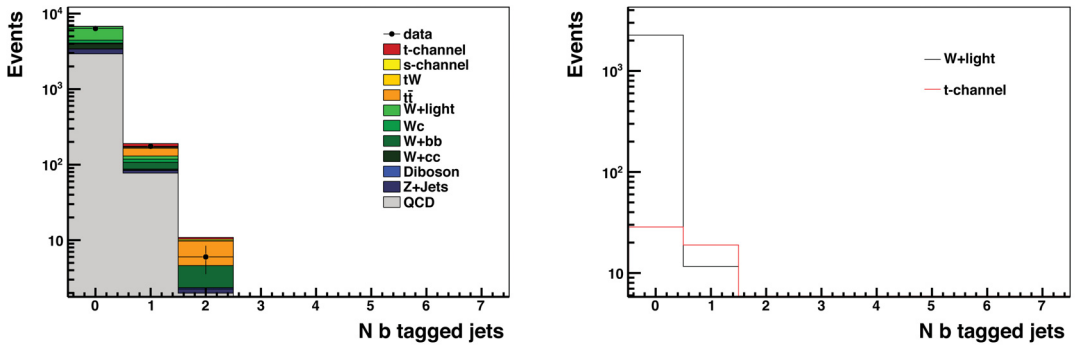

(a) (b)

Figure 5.2: Number of jets with $D_{TCHP} > 3.41$ for data and simulation, and for signal and $W+$ light partons only, after the 2 jets request.

As further request we apply a b-veto, rejecting events in which the jet which fails the tight b-tagging selection passes the loose one. In Fig. 5.3 the number of b-vetoed jets in 2-jets events with one b-tagged is shown.

Transverse W boson mass

To suppress events in which the lepton does not come from the W boson, a further selection is applied on the boson reconstructed transverse mass M_T. It is defined as:

$$M_T = \sqrt{(p_{T,l} + p_{T,\nu})^2 - (p_{x,l} + p_{x,\nu})^2 - (p_{y,l} + p_{y,\nu})^2}\,, \tag{5.4}$$

where the transverse momentum components of the neutrino are approximated by the components of the missing transverse energy, $\vec{\not{E}}_{\mathrm{T}}$. Defined in an analogous way as PF-based jets, PF-based $\not{E}_{\mathrm{T}}$ is the total energy unbalance coming from the vectorial sum of

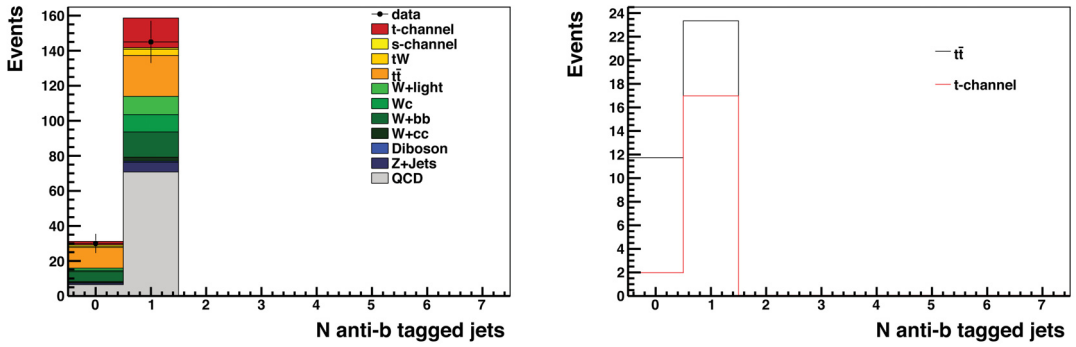

(a) (b)

Figure 5.3: Number of jets with $D_{TCHE} < 1.7$ (b-vetoed jets also called anti-b tagged jets) for data and simulation, and for signal and $t\bar{t}$, after the 2 jets 1 b-tag request.

the transverse momenta of the identified PF particles (in the analysis no explicit cut is applied on $\not\!\!E_{\mathrm{T}}$).

Figure 5.4 shows the shape of the M_T distribution after the preceding selection. The QCD background can be nicely distinguished, since the transverse mass of the alleged W bosons accumulates at low values while all processes with real W bosons tend to cluster around the W mass (this feature is known in the literature as "Jacobian peak"). The M_T variable has been preferred to the simple $\not\!\!E_{\mathrm{T}}$ because of its better separation power between signal and QCD, its better stability to the jet energy scale (see Sec. 5.5) and the fact that its distribution behaves almost similarly for all non QCD events, allowing a very simple extraction of the QCD amount from data (see Sec. 5.3.1).

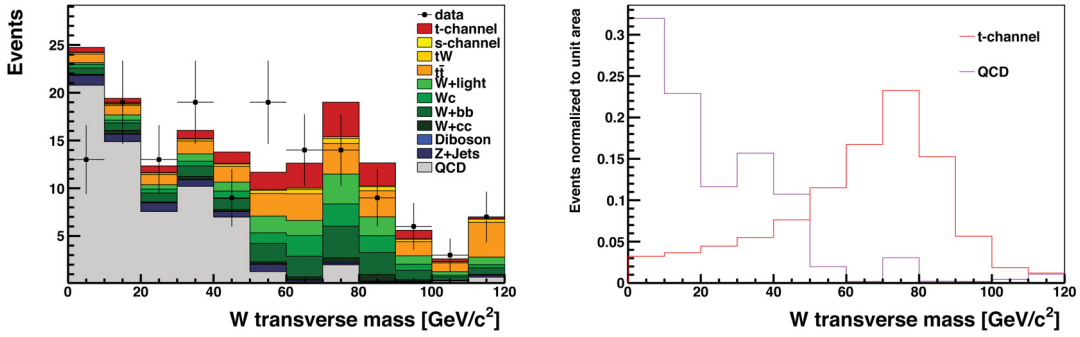

(a) (b)

Figure 5.4: Transverse mass after the entire selection minus the M_T cut, in data and Monte Carlo and for signal and QCD.

The threshold on the M_T variable is chosen by means of a data-driven procedure: applying a selection which is complete apart from the released b-tagging requirement (Fig. 5.5), a template fit to M_T is performed to extract the relative contribution of W-like and QCD events; then we choose the M_T threshold which minimizes the total uncertainty on the fit result. In conclusion the threshold chosen is $M_T > 50$ GeV/c^2.

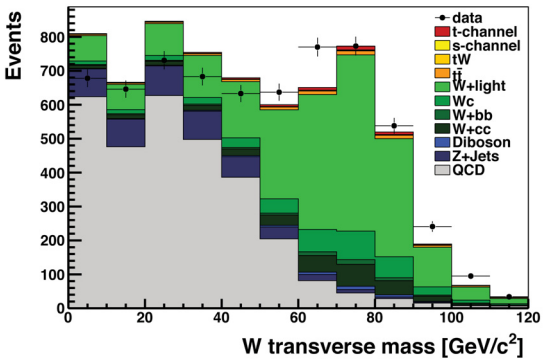

Figure 5.5: Transverse mass after the entire selection minus the M_T cut and the b-tagging requirements.

Selection results

The number of selected events, step by step, in data and Monte Carlo is shown in Table 5.2. After the leptonic selection the sample is still dominated by QCD, despite the isolation requirements on the reconstructed electron. This motivates the use of the combined isolation variable I_{rel}, and an additional selection on the transverse W-boson mass allows a good QCD reduction. Nevertheless, QCD remains one of the most difficult backgrounds to predict (see Sec. 5.3.1). The second most dominating background after the leptonic selection, W+jets, is reduced significantly by the use of b tagging. Among the remaining background contamination, most events contain two b quarks in the final state (e.g., $t\bar{t}$, $Wb\bar{b}$, single top in s-channel) while the presence of just one visible b quark is a specific feature of the signal (shared with tW); thus we further enhance the S/B ratio by a veto on a second b-tagged jet, with a looser threshold. Due to the size of the background contamination with respect to the signal, we would need a very precise control of the backgrounds in order to find an evidence of signal through a simple event counting, in this scenario. Instead, on top of this selection, in Sec. 5.4 the full shapes of a couple of discriminating variables are exploited in order to extract the signal, while minimizing the need of assumptions about the main background processes.

Scale factors for b-tagging and mistagging

For the tight TCHPT and loose TCHEL b-tagging working points used in this analysis respectively for the tagged and veto jets, in order to correct the observed difference between simulated and measured mistagging rates and b-tagging efficiencies we scale the simulated events according to p_T- and η-dependent scale factors taken from the conditions database (the b-tagging efficiency is well approximated by the flat scale factor $SF = (90 \pm 15)\%$). The b-tagging efficiency both on data and simulation is evaluated studying the p_{T} distribution of the muon produced in association with a jet in semileptonic

Process	1 iso e, 0 μ	2 jets	1 tight b tag	loose b veto	$M_T > 50$ GeV
single top, t channel	104.5	48.1	18.95	16.98	12.80 ± 0.14
single top, s channel	7.53	3.71	1.661	0.838	0.616 ± 0.008
single top, tW	34.57	12.09	4.25	3.54	2.58 ± 0.04
$t\bar{t}$	477.6	84.4	35.1	23.4	17.1 ± 0.3
Wc	4143	380	13.4	12.8	10.2 ± 0.4
$W+$ light partons	96383	2260	14.6	13.4	10.5 ± 1.1
$Z+$ X	5663	471	6.4	5.5	1.6 ± 0.3
$V + Q\bar{Q}$	10093	336	14.5	10.8	7.7 ± 0.4
WW	72.48	21.31	0.331	0.309	0.235 ± 0.011
WZ	17.42	5.27	0.370	0.231	0.172 ± 0.005
ZZ	2.326	0.796	0.063	0.0456	0.0120 ± 0.0009
QCD ($b/c \to e$, $20 < \hat{p}_T < 30$ GeV)	221	2	< 6.4 (95% CL)	-	-
QCD ($b/c \to e$, $30 < \hat{p}_T < 80$ GeV)	1478	188	27	25	< 7.4 (95% CL)
QCD ($b/c \to e$, $80 < \hat{p}_T < 170$ GeV)	117	38	5.5	5.2	0.6 ± 0.5
QCD (e/γ-enriched, $20 < \hat{p}_T < 30$ GeV)	2894	14	< 7.2 (95% CL)	-	-
QCD (e/γ-enriched, $30 < \hat{p}_T < 80$ GeV)	17810	1860	29	29	< 9.5 (95% CL)
QCD (e/γ-enriched, $80 < \hat{p}_T < 170$ GeV)	1417	455	8	5.6	3.1 ± 1.4
QCD ($\gamma+$ jets, $40 < \hat{p}_T < 100$ GeV)	2521	141	0.8	0.8	< 1.2 (95% CL)
QCD ($\gamma+$ jets, $100 < \hat{p}_T < 200$ GeV)	562	272	5.6	4.6	0.8 ± 0.3
QCD ($\gamma+$ jets, $\hat{p}_T > 200$ GeV)	94.7	44.8	1.58	1.30	0.46 ± 0.08
Total background	144061	6601	168	142	57 ± 2
Signal + background	144165	6649	187	159	70 ± 2
Data	128128	6536	175	145	72

Table 5.2: Number of events surviving each selection step, in data and Monte Carlo (normalized to 36.1 pb^{-1}).

decays of b-hadrons. Muons coming from a heavy hadron have a relatively hard transverse momentum distribution; therefore from a fit to data using Monte Carlo predictions for the p_{T} distributions of muons in association with heavy or light flavoured jets, the b content of the muon jet sample can be determined. The mistag rate is evaluated from tracks with negative impact parameters, the negative discriminator being obtained by inverting the order of the tracks from the most negative IP significance upwards. More details could be found in [80].

We define the scale factors to be applied for Monte Carlo events reweighting, both for b-tagged and b-vetoed jets as:

$$\begin{aligned} SF &= \epsilon_{data}^{TCHPT}/\epsilon_{MC}^{TCHPT} \\ SF' &= (1-\epsilon_{data}^{TCHEL})/(1-\epsilon_{MC}^{TCHEL}) \end{aligned} \tag{5.5}$$

where $\epsilon_{data,\,MC}^{TCHPT,TCHEL}$ is the efficiency (for b, c quarks) or mistag probability (for g, u, d, s partons) for algorithm TCHPT or TCHEL in data or simulation. Now, given the total number of jets N out of which $N^{b\,tag}$ and $N^{b\,veto}$ pass the b-tag cut and the b-veto cut, respectively, the correction to be applied could be written as in the following

$$\begin{aligned} N^{b\,tag} &= \epsilon_{data}^{TCHPT} \cdot N = \epsilon_{MC}^{TCHPT} \cdot N \cdot SF \\ N^{b\,veto} &= (1-\epsilon_{data}^{TCHEL}) \cdot N = (1-\epsilon_{MC}^{TCHEL}) \cdot N \cdot SF' \end{aligned} \tag{5.6}$$

Here the dependency from η and p_{T} of the jet although taken into account is omitted for clarity reasons. An event with 2 jets where one is heavy-flavoured and the other light-flavoured, has the probability P to pass the b-tagging and b-veto steps of the selection equal to:

$$P(1,2) = P^{b\,tag}(1) \cdot P^{b\,veto}(2) + P^{b\,tag}(2) \cdot P^{b\,veto}(1) \tag{5.7}$$

where $P^{b\,tag}(i)$ is the probability for the i-th jet to be b-tagged and $P^{b\,veto}(i)$ is the probability for the i-th jet to be b-vetoed. Using the convention $p = b, c$ for heavy quarks and $q = g, u, d, s$ for light partons, we define $N_{p,q'}^{MC}$ as the number of MC events in which the p-jet passes the b-tagging requirement and the q-jet passes the b-veto cut and $N_{q,p'}^{MC}$ as the number of MC events in which the q-jet passes the b-tagging requirement and the p-jet passes the b-veto cut. These numbers are expressed in terms of the efficiencies: $N_{p,q'}^{MC} = \epsilon_{MC_p}^{TCHPT}(1-\epsilon_{MC_q}^{TCHEL}) \cdot N$ and $N_{q,p'}^{MC} = \epsilon_{MC_q}^{TCHPT}(1-\epsilon_{MC_p}^{TCHEL}) \cdot N$. In conclusion, combining equations 5.6 and 5.7 and using the relations above introduced, after some

calculation the corrected overall number of events passing the two cuts is:

$$N_{corr} = \Sigma_{p,q}\left(SF_p SF'_q \cdot N^{MC}_{p,q'} + SF_q SF'_p \cdot N^{MC}_{q,p'}\right) \tag{5.8}$$

So what it is done is to apply to each p- and q-jet passing the b-tagging (b-veto) cut a weight of SF (SF'), and in the end weight the event with the products of the two weights.

5.3 Data driven background estimation

5.3.1 Multi-jet QCD

The selection described in 5.2.2 has the advantage to hugely reduce the QCD contamination of the signal region. On the other side, instead, we can not completely trust the QCD simulation since tail effects are not well described in Monte Carlo. Therefore, data-driven techniques need to be adopted in order to give a reliable estimation of the amount of this QCD background.

For this purpose a template fit to the M_T distribution is performed, after all other cuts have been applied, with the following fit function:

$$F(M_T) = N_{sig-like} \cdot S(M_T) + N_{qcd} \cdot B(M_T)\ , \tag{5.9}$$

where $S(M_T)$ and $B(M_T)$ are the assumed M_T distributions for signal-like processes [2] according to Monte Carlo predictions, and QCD events (extracted form data) respectively, leaving $N_{sig-like}$ and N_{qcd} as free parameters. So the number of QCD events in the signal region, N^{SR}_{qcd}, is obtained by integrating the function $B(M_T)$ normalized to the fitted QCD events, for $M_T > 50$ GeV: $N_{qcd} \cdot \int_{50}^{\infty} B(M_T) dM_T$,

To avoid as much as possible model dependent assumptions for QCD, $B(M_T)$ is extracted from a control sample on data, characterized by high statistics and similar kinematics with respect to the selected sample. In particular a QCD-enriched sample is defined by releasing the b-tagging requirement and by an anti-isolation cut ($I_{\rm rel} > 0.2$) which removes the great part of signal events (Tab. 5.3 shows the event yields for this selection). The data / MC agreement between M_T distributions for the QCD enriched sample is not bad and by the way the observed difference in the tail goes in the "conservative" direction (in Fig. 5.6, the data anti-isolated M_T distribution is that used as a template for the $B(M_T)$ shape). In Fig. 5.7 it could be noticed that the M_T shape is similar for W + jets events, for signal, and for $t\bar{t}$ (despite a broadening in the distribution due to events in which there are two final state neutrinos). However, since the detail of single signal-like components turns out to be not critical for our purposes, we consider and fit all together the non-QCD processes, and take the $S(M_T)$ shape from simulation.

[2] Here and in the following, with signal-like events we mean all events where the lepton comes from the decay of a W boson, including for example $t\bar{t}$ and W+jets.

Process	$N_{evtpre-tag}$	$N_{evtafter-tag}$
QCD	$4.8 \cdot 10^4$	$14.9 \cdot 10^2$
$signal$	0.36	0.042
$t\bar{t}$	0.57	0.036
$W + X$	35.3	0.076
Data	$6.0 \cdot 10^4$	$12.8 \cdot 10^2$

Table 5.3: Event yields for the main background and signal processes in the QCD-enriched sample before and after the b-tagging requirement.

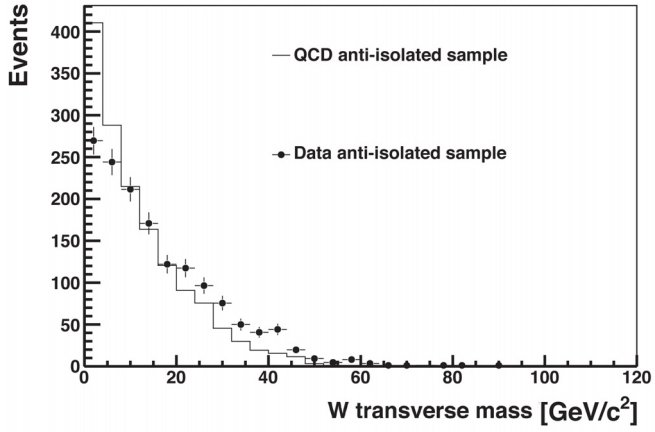

Figure 5.6: M_T distribution for the QCD-enriched control sample, in data and Monte Carlo.

Since the low M_T region is quite critical the fit is performed in the range (30, 200) GeV/c^2. In order to test the stability of the fit we changed the fit range and checked the consistency of the results. The systematics uncertainty is then conservatively estimated as the maximum between 50% and the maximum shift from the central value obtained in these fits. Table 5.4 shows the fit results for the different fit ranges chosen. Moreover, the stability of the fit with respect to variation of the background model has been checked, using as QCD shape the M_T Monte Carlo distribution of the QCD anti-isolated pre-tag sample (plots of fit results and stability checks in Fig. 5.8). The absolute value of the difference between the results of the fits in the two conditions is taken as systematic uncertainty on the QCD yield and summed up to the statistical uncertainty coming from the fit.

Summing up, the number of QCD events above the M_T threshold estimated with the fit procedure described is:

$$N_{qcd} = 2.6 \pm 0.6(stat.) \pm 3.1(shape) \pm 1.2(stability) \tag{5.10}$$

where "$shape$" indicates the systematic uncertainty from QCD template model assumption (using data-driven or Monte Carlo sample) and "$stability$" stands for the maximum variation between the results obtained variating the fit range ($20 < M_T < 200$ GeV/c^2 and $35 < M_T < 200$ GeV/c^2, taking the maximum variation as symmetric uncertainty).

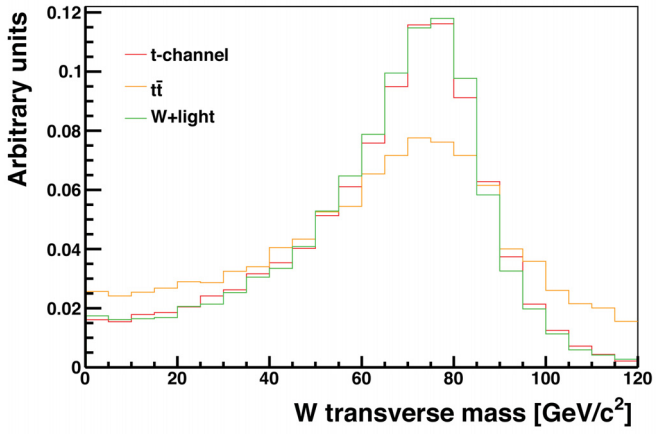

Figure 5.7: M_T distributions for: signal (red), $t\bar{t}$ (yellow) and W + light partons (orange). The selection applied here differs from the nominal one only for the anti-isolation requirement.

QCD Model	N_{qcd}, full fit range	N_{qcd}, M_T cut
data-driven range 30-200	23 ± 9	2.6 ± 0.6
MC pre-tag range 30-200	28 ± 8	5.7 ± 1.4
data-driven range 20-200	26 ± 7	1.4 ± 0.4
data-driven range 35-200	17 ± 6	3.0 ± 1.1

Table 5.4: Result of the fits on M_T using the QCD distribution either from data with anti-isolation requirement or from Monte Carlo sample without applying the b-tagging requirement.

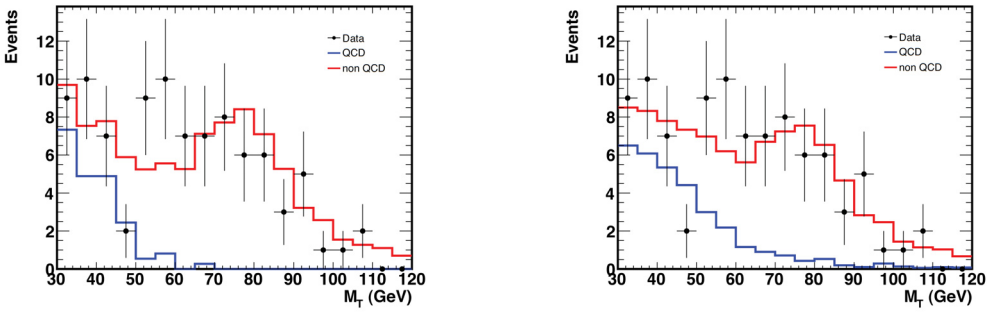

(a) (b)

Figure 5.8: M_T fits with the data-driven QCD template (a) and Monte Carlo QCD template obtained from pre-tag anti-isolated sample (b). The difference between these fit values is summed to the statistics uncertainty on the fit and used as systematics on the QCD prediction.

For the final template-fit used in the extraction of the single top cross section, we will use the QCD control sample taken from data for the fit variables distributions, and normalize them to the prediction above described.

Process	N_{evt}
$W+$ light partons	1731
Wc	296
$Wc\bar{c}$	422
$Wb\bar{b}$	88
$t\bar{t}$	61
QCD	40
signal	36
MC total	3031
Data	3165

Table 5.5: Event yield for the main processes in the W-enriched selection "A".

5.3.2 $W+$ jets

This section is devoted to the treatment of the W + jets component of the backgrounds.

As mentioned in Sec. 5.2.1 we remove double counting and allow for a coherent sum of all W contributions. Since not all W MC samples are calculated at the NNLO, we perform the splitting and remerging considering the LO cross sections; the relative contribution of light and heavy flavour is then fixed and the samples are normalized to the NNLO cross section by rescaling each component with the ratio between the W + jets sample taken without any flavor requirement (which is at NNLO) and the sum of all the flavor-splitted contributions (which are evaluated at LO).

As for multi-jet QCD, since our selection constrains the W + light flavors component to extreme kinematic regions, a partially data-driven method is used to extract the shape of variables used for the analysis for such sample. Two control regions are defined, which are enriched in the W + light flavors background, orthogonal to the signal region and defined by electron passing the standard selection and having exactly two jets:

- control sample "A" is defined by having the highest-TCHP jet failing the tight TCHP threshold;
- control sample "B" is a sub-set of A, where the highest-TCHP jet fails the tight TCHP threshold but passes the loose TCHE threshold.

Tab. 5.5 reports the number of events in the W-enriched control sample "A".

To model the distributions of the variables fitted in this analysis, η_{lj} and $\cos\theta^*_{lj}$ (Sec. 5.4.2) in W + light flavor background events in the signal region, we use the distributions obtained in this W-enriched sample in data, after subtracting the other contributions (including signal, which accounts for roughly 1% of this sample) estimated with simulated samples. No significant distortion of the W + light partons shapes is found when comparing the W-enriched control sample and the sample after full event selection (Fig. 5.9). As it will be explained in Sec. 5.4.1 in the top momentum reconstruction the jet with the highest value of the b-tag TCHE algorithm is used as "b-jet" for the W + light sample.

In the following we show some validation plots in the control region A. Fig. 5.10 shows the distributions of $\cos\theta^*_{lj}$ and η_{lj} for data and Monte Carlo. Figures 5.11, 5.12,

5.13, and 5.14 show the two variables $\cos\theta^*_{lj}$ and η_{lj} for the W+light, $W+bb$, $W+cc$, and $W+c$ channels in the W-enriched sample compared to those after full selection. Fig. 5.9 shows the $\cos\theta^*_{lj}$ and η_{lj} distributions for W+light partons in Monte Carlo compared with the distribution extracted from control sample A in data. The shapes for $W+bb$, $W+cc$ and Wc with this selection are then used as templates for the same variables in the signal region in the fit procedure.

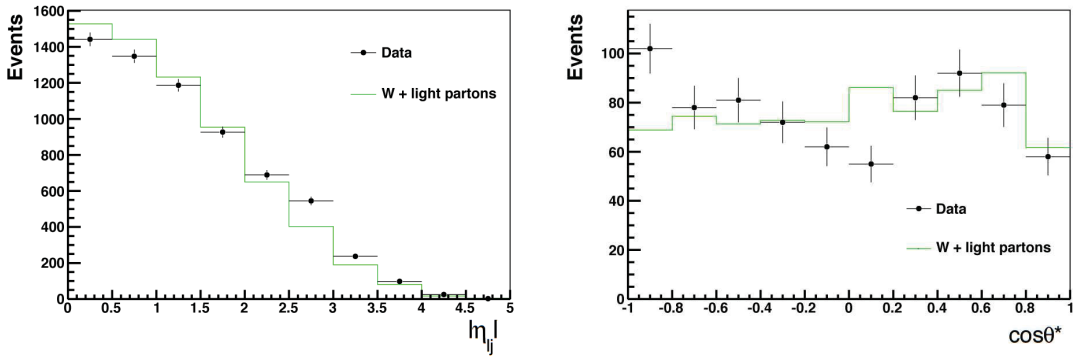

(a) (b)

Figure 5.9: Distributions of η_{lj} (a) and $\cos\theta^*_{lj}$ (b) in the W-enriched sample A for data and W + light flavors Monte Carlo.

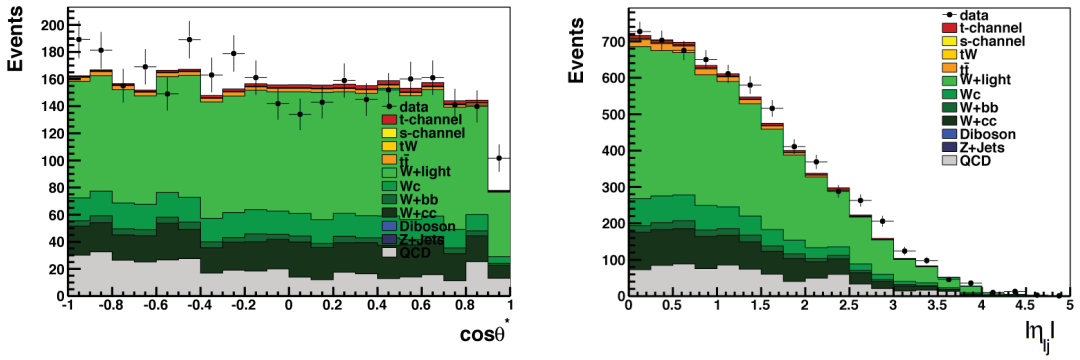

(a) (b)

Figure 5.10: Distributions of η_{lj} (a) and $\cos\theta^*_{lj}$ (b) in the W-enriched sample A for data and Monte Carlo, normalized to the luminosity of data.

We estimate the actual W + light partons component of this W-enriched control sample by performing a fit to the M_T distribution in both control samples A and B. The QCD component is left floating, with template taken from the same selection but inverted isolation cut (as in Sec. 5.3.1), the W + light partons component is kept floating, with template from Monte Carlo, and all other components including W + heavy partons, are fixed to expectations. The fit results are shown in Fig. 5.15 and in Table 5.6.

The scale factor from control sample B are taken as central predictions, upon the argument that it is closer to the signal region, obtaining an expectation of 11.6 $W+$ light parton events in the signal region, and we assign to it a $\pm 20\%$ uncertainty which covers

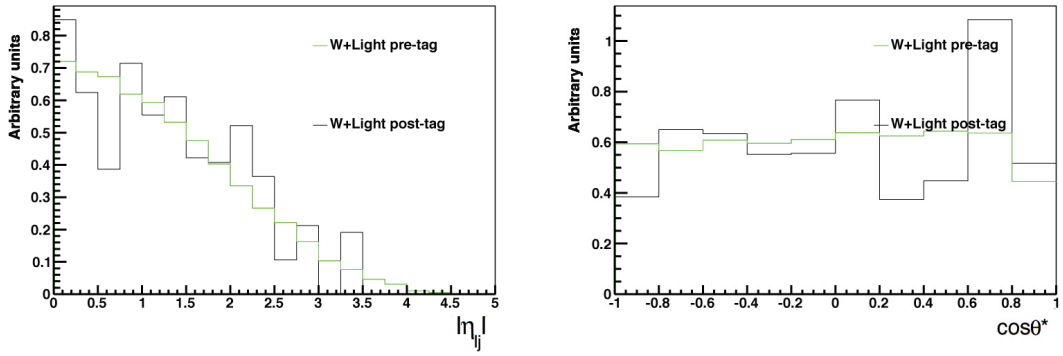

(a) (b)

Figure 5.11: Distributions of η_{lj} (a) and $\cos\theta^*_{lj}$ (b) in the W-enriched sample A and after full selection for W + light flavors Monte Carlo.

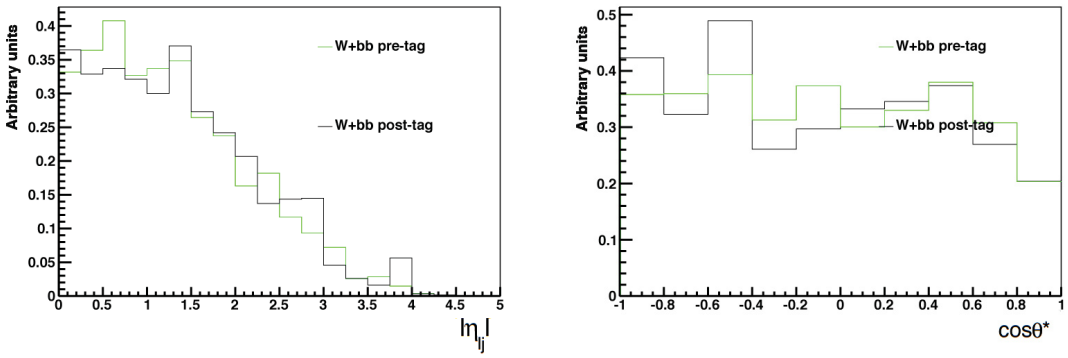

(a) (b)

Figure 5.12: Distributions of η_{lj} (a) and $\cos\theta^*_{lj}$ (b) in the W-enriched sample A and after full selection for $Wb\bar{b}$ Monte Carlo. The parton showering component taken from the W+jets sample is also shown in this plot and is the main responsible for the statistical fluctuation. The shape of the variables for the fit are thus taken from W-enriched sample.

both the statistical uncertainty from the fit and the difference between A and B predictions. This is taken into account as a rate systematic in section 5.5. The same scale factors are applied to $Z+$ jets.

For what concerns the W + heavy flavour component, since advanced studies need more statistics, it is made the assumption that the scale factors obtained by the SHyFT (Simultaneous Heavy Flavor and Top) CMS analysis group [59] with a simultaneous extraction of $t\bar{t}$ and of its main backgrounds, and the corresponding ranges of variation (doubled to be conservative), can be reliably applied to the particular phase-space region of the present analysis. The scale factors applied are those corresponding to equations 5.1 and 5.2. We get confidence in the adequacy of this hypothesis by comparing data and Monte Carlo in both the signal region and in the W-enriched control sample A discussed before with and without these scale factors, see Fig. 5.16. We conclude that the application of these scale factors improves the agreement between data and Monte Carlo in the control region, although it does not impact enough the signal region to explain the ob-

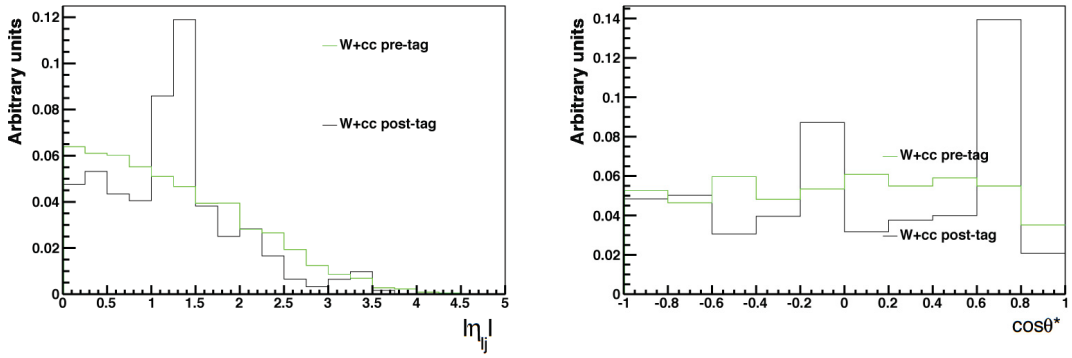

(a) (b)

Figure 5.13: Distributions of η_{lj} (a) and $\cos\theta^*_{lj}$ (b) in the W-enriched sample A and after full selection for $Wc\bar{c}$ Monte Carlo. The parton showering component taken from the W+jets sample is also shown in this plot and is the main responsible for the statistical fluctuation. The shape of the variables for the fit are thus taken from W-enriched sample.

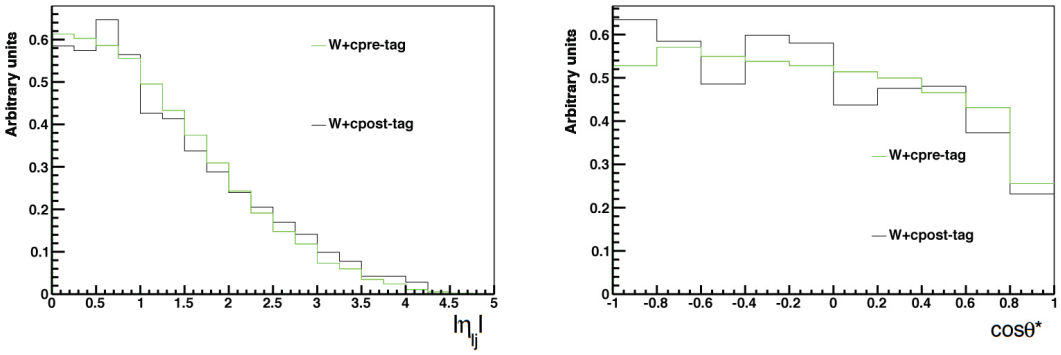

(a) (b)

Figure 5.14: Distributions of η_{lj} (a) and $\cos\theta^*_{lj}$ (b) in the W-enriched sample A and after full selection for W + c Monte Carlo.

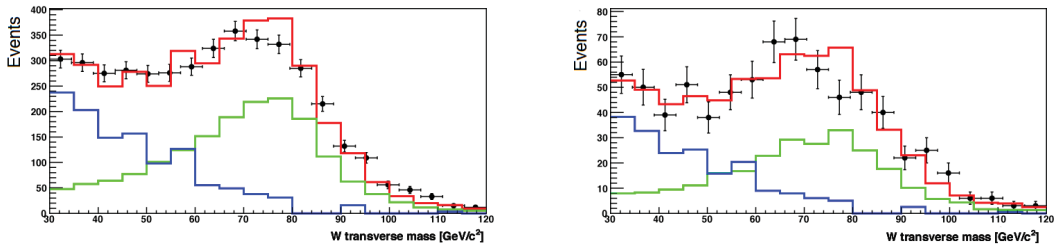

(a) (b)

Figure 5.15: M_T fits in control region A (a) and B (b). Blue: QCD template; green: W + light flavor template; red: total fit function; points: data.

served excess of data, which instead we attribute to an excess of signal with respect to the Standard Model expectation.

Summing up, in the following QCD and W + light are normalized to the predictions

SF from region A	SF from region B
0.97 ± 0.04	1.05 ± 0.11

Table 5.6: Scale factors for $W+$ light partons defined as ratio between the number of $W+$ light events fitted and the number of events predicted by Monte Carlo, in control regions A and B. Uncertainties are statistical only.

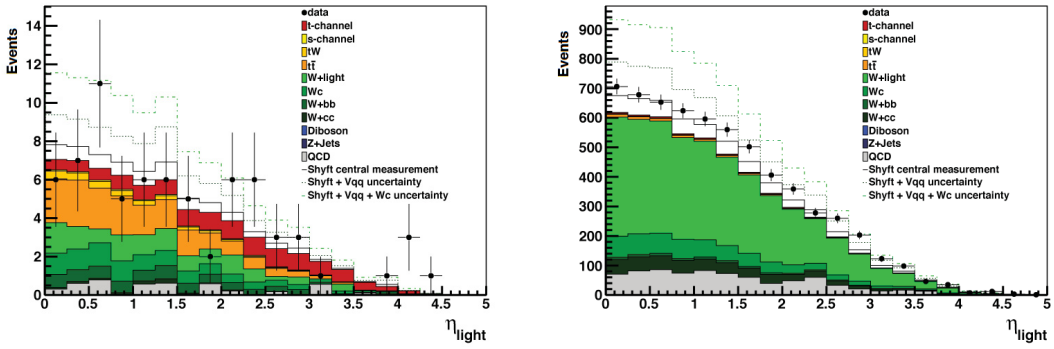

(a) (b)

Figure 5.16: Distribution of η_{lj} in the signal region (a) and in the W-enriched control sample (b), with and without the scale factors from Ref. [59].

of the data-driven procedure previously described, Z + jets is scaled by the same factor as W + light partons, $VQ\bar{Q}$ and Wc components are scaled to the LO prediction and then by the SHyFT factors, $t\bar{t}$ normalization is taken from the cross section measurement exploiting b-tagging described in [67], and for VV, single top s-channel and tW-channel, the theory predictions are used [68, 39, 69].

5.4 Signal properties and fit procedure

5.4.1 Top quark reconstruction and signal properties

Once a supposedly signal-enriched sample has been selected from real collision data, it is important to check that it exhibits the features expected for single top. One important feature of the signal is the presence of a recoil jet, from the fragmentation of a light quark (Fig. 4.5 (c)), with a characteristic pseudorapidity distribution (Fig. 5.17). In particular this jet is expected to be produced forward (high η_{lj}) for the signal and more or less centrally for all the backgrounds. The figure shows a slight excess of 4 events in the last bin of the distribution: these have been individually scrutinized, but no anomaly was found; in the end we conclude that this excess with respect to signal+background expectation is due to a mere statistical fluctuation.

Another obvious feature of the signal is the presence of a top quark, recognizable from a mass peak when properly combining the final state objects. The first step in the reconstruction of the top quark from its decay products is the reconstruction of the W boson. We assume that the x and y components of the missing energy are entirely due to the

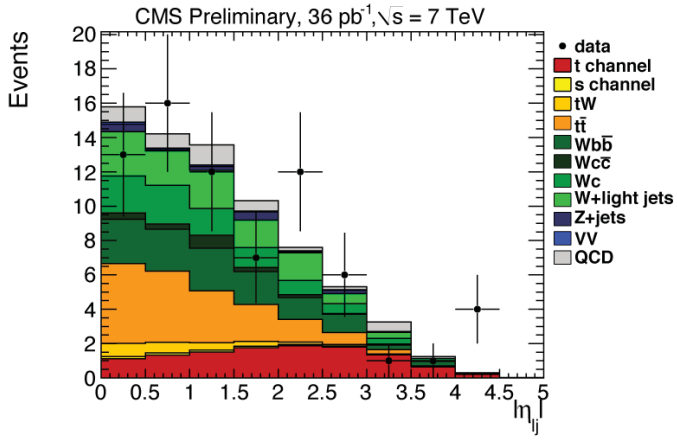

Figure 5.17: Pseudorapidity of the untagged jet (η_{lj}) after the full event selection.

escaping neutrino, and apply the W-mass constraint in order to extract the z component ($P_{z,\nu}$):

$$M_W^2 = (E_e + \sqrt{\not{E}_{\mathrm{T}}{}^2 + P_{z,\nu}^2})^2 - (\vec{P}_{T,e} + \vec{\not{E}}_{\mathrm{T}})^2 - (P_{z,e} + P_{z,\nu})^2 \,. \tag{5.11}$$

This equation has in general two solutions:

$$P_{z,\nu}^{A,B} = \frac{\mu \cdot P_{z,\mu}}{P_{T,\mu}^2} \pm \sqrt{\frac{\mu^2 \cdot P_{z,\mu}}{P_{T,\mu}^4} - \frac{E_\mu^2 \cdot \not{E}_{\mathrm{T}}{}^2 - \mu^2}{P_{T,\mu}^2}} \,, \tag{5.12}$$

with

$$\mu = \frac{M_W^2}{2} + \vec{P}_{T,\mu} \cdot \vec{\not{E}}_{\mathrm{T}} \,. \tag{5.13}$$

If the discriminant in equation 5.12 becomes negative, or equivalently M_T is larger than the W pole mass used in the constraint, the solutions have an imaginary part. This happens in 36.0% of the cases, mostly due the finite resolution of $\not{E}_{\mathrm{T}}$ (lepton momentum resolution and the finite W width give negligible contributions; see, e.g., the s-channel single-top analysis in Ref. [70] for a detailed study of this effect in very similar conditions).

Several schemes exist to deal with this situation; here the imaginary component is eliminated by modifying $\not{E}_{\mathrm{T}}$ such to give $M_T = M_W$, still respecting Eq. 5.11. This is obtained by imposing that the discriminator, and thus the square root in Eq. 5.12, are null; this gives a quadratic relation between $P_{x,\nu}$ and $P_{y,\nu}$, with two solutions, among which the one with minimal distance between $P_{T,\nu}$ and $\not{E}_{\mathrm{T}}$ is chosen.

In the case of two real solutions for $P_{z,\nu}$, different choice criteria have been proposed in the literature. Here the solution with the smallest absolute value is chosen. The W boson is thus reconstructed by this procedure when the discriminant of Eq. 5.12 is positive, and by the preceding procedure when it is negative. A similar two-fold ambiguity appears when reconstructing the top-quark hypothesis, since two jets are selected. The ambiguity is resolved by assigning the b-tagged jet to the top-quark decay.

Figure 5.18 shows the mass of the reconstructed top quark ($M_{bl\nu}$) for events passing the full selection. The observation of a peak at $\approx M_{top}^{Tevatron}$ in the selected sample from real collision data is a smoking gun of the presence of top quarks. For QCD and $W/Z+X$ events, $M_{bl\nu}$ is expected to be broad and soft. In $t\bar{t}$ events, a peak is expected but it is broadened with respect to the signal by several effects, e.g.: two true b quarks are present, and in 50% of cases we expect to pick up the one not coming from the same top as the selected lepton; and in $t\bar{t} \to 2l$ events (including tauons) the missing energy gets contributions by more than one neutrino.

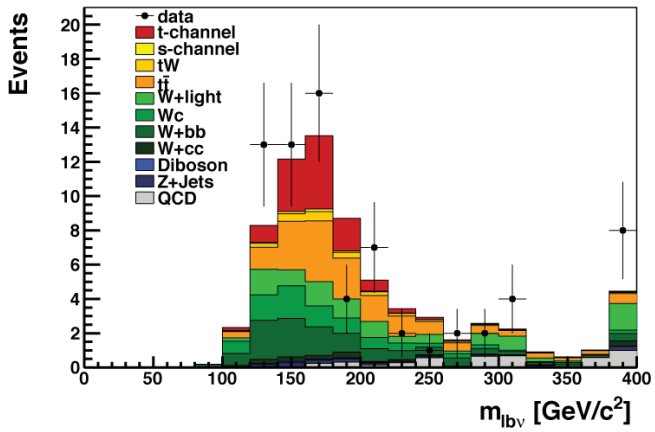

Figure 5.18: Reconstructed top-quark mass after the full selection. The last bin also contains events with $M_{bl\nu} > 400$ GeV/c^2.

An other specific feature of our signal, stemming from the $V-A$ structure of the weak interaction, is the almost 100% left-handed polarization of the top quark with respect to the spin axis [71]. The direction of the top quark spin is reflected in angular correlations in its decay products, which are distributed according to the formula

$$\frac{1}{\Gamma}\frac{d\Gamma}{d\cos\theta^*} = \frac{1}{2}(1 + A\cos\theta^*) \,, \tag{5.14}$$

where θ^* is the angle between the direction of the outgoing particle and the spin axis, in the top-quark rest frame. A is a coefficient of spin asymmetry, which depends on the identity of the particle and is equal to $+1$ for charged leptons [71]. We make use of the "spectator basis" (see, e.g., Ref. [72]), where θ^* is taken equal to the angle θ^*_{lj} between the lepton direction and the light quark recoiling against the virtual W boson, in the top-quark rest frame; in practice, the direction of the untagged jet is chosen as spin axis, after a boost of all the 4-vectors is performed in the rest frame of the reconstructed top quark. Figure 5.19 shows the distribution of the cosine of this variable ($\cos\theta^*_{lj}$). The dip at $\cos\theta^*_{lj} \approx 1$ is an artifact of the lepton selection. The same artifact, and the sensitivity of the shape of this variable to some modeling effects, have been studied at generator level in Ref. [73], and after full reconstruction in previous Monte Carlo studies [74].

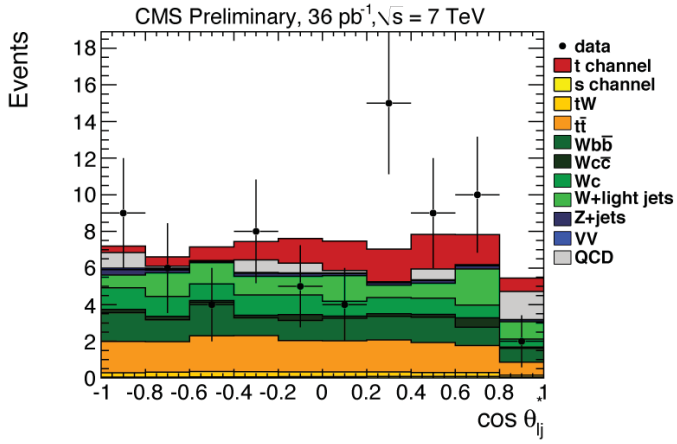

Figure 5.19: Cosine of the angle between electron and untagged jet, in the reconstructed top rest frame after the full event selection.

5.4.2 Fit method and cross section measurement

A maximum likelihood fit is performed to $\cos\theta^*_{lj}$ and η_{lj} distributions to extract the t-channel single top cross section. The free parameters are the signal and overall background yields. The individual background components are constrained in order to be as much robust as possible against background uncertainties, considering that all the backgrounds have similar distributions in the two variables chosen for the fit.

We define the following unbinned likelihood function:

$$\begin{aligned} L(\cos\theta^*_1, ..., \cos\theta^*_n, \eta_1, ..., \eta_n | N_s, N_b) = \\ = e^{-(N_s+N_b)} \prod_{k=1}^{n} \left(N_s \cdot P_s(\cos\theta^*_k, \eta_k) + N_b \cdot P_b(\cos\theta^*_k, \eta_k) \right) \end{aligned} \tag{5.15}$$

where N_s, N_b are the signal and background yields, n is the number of observed events, P_s, P_b the signal and background probability density functions. The variables $\cos\theta^*_{lj}$ and η_{lj} are weakly correlated (it has been estimated, on simulation, a correlation of 6% for signal and 2% for the overall background) and so it is possible to factorize the signal and background fit functions into the product of two pieces: $P_s = F_s(cos\theta^*) \cdot G_s(\eta)$ and $P_b = F_b(cos\theta^*) \cdot G_b(\eta)$. In detail, the background term in equation 5.15 is given by:

$$N_b \cdot F_b(cos\theta^*) \cdot G_b(\eta) = \sum_i N_{b_i} \cdot F_{b_i}(cos\theta^*) \cdot G_{b_i}(\eta) \tag{5.16}$$

where i runs over all the backgrounds. Performing an extended maximum likelihood fit with the model distributions considered fixed and taken from simulation (relative background normalizations taken from the simulation as well), we obtain the best estimation of N_s and N_b. The fit results are shown in Fig. 5.20, and the estimated yields are:

$$N_s = 30 \pm 11 N_b = 46 \pm 12 \qquad \text{electrons}$$

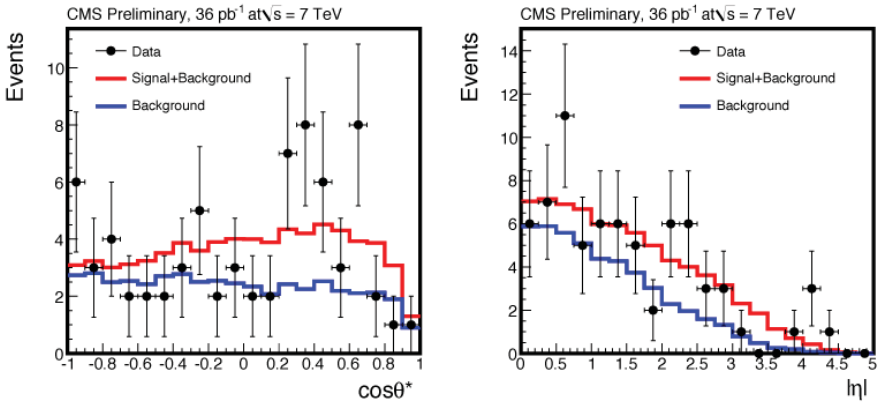

Figure 5.20: Fit to $\cos\theta^*_{lj}$ and η_{lj} .

The sensitivity of the analysis to the single top signal has been estimated using two methods: profile likelihood and CL_b method. The CL_b method is implemented with the use of the *theta* framework [75], in which systematic uncertainties are included via a prior-predictive technique using template morphing. This method is discussed in detail after the description of systematic uncertainties, in Sec 5.5.2.

Profile likelihood method

We define the test statistics λ as:

$$-2\ln\lambda(N_s) = -2\ln\left(\frac{L(N_s,\hat{\hat{N}}_b)}{L(\hat{N}_s,\hat{N}_b)}\right) \tag{5.17}$$

where $L(\hat{N}_s,\hat{N}_b)$ represents the maximum likelihood function evaluated for the best estimations of the free parameters, while $L(N_s,\hat{\hat{N}}_b)$ is the maximum value obtained by fixing N_s and fitting N_b. If we vary the signal hypothesis N_s we obtain the profile likelihood function which can be used for extracting the significance of the single top signal (Fig. 5.21 shows the $\log\lambda$ distribution for the fit to $\cos\theta^*_{lj}$ and η_{lj}). Using Wilks' theorem, $-2\ln\lambda(N_s)$ is asymptotically distributed as a χ^2 variable (that is the profile likelihood curve has a parabolic shape) with one degree of freedom since one is the number of exceeding free parameters in the numerator of Eq. 5.17 with respect to the denominator, so that:

$$-2ln\lambda(N_s) = -2(lnL(N_s) - lnL(\hat{N}_s)) = n_\sigma^2 \quad \text{with} \quad n_\sigma = \frac{N_s - \hat{N}_s}{\sigma} \tag{5.18}$$

where σ represents the Gaussian standard deviation of the parameter N_s. The observed

significance of the single top signal is:

$$n_\sigma = 3.2$$

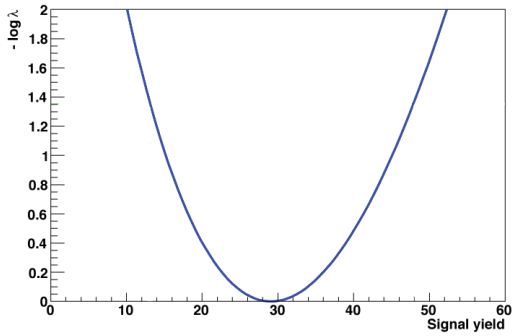

Figure 5.21: Profiling likelihood resulting from the fit to $\cos\theta^*_{lj}$ and η_{lj}.

To test the absence of biases and the consistency of the profile likelihood method as analysis sensitivity estimator, we repeat the procedure on pseudo-data generated according to the background-only hypothesis. This is done using the P_b defined previously as function for the generation. We performed 2000 pseudo-experiments and the significance distribution obtained is plotted in Fig. 5.22 (a), showing a good agreement with a one-tailed Gaussian distribution (it is shown in logarithmic scale). As further check, pseudo-experiments are also drawn according to signal + background hypothesis and the agreement with a Gaussian distribution is observed as well (as shown in Figure 5.22 (b)). The mean and RMS of significance distribution for signal + background hypothesis are 1.6 and 1.0 respectively.

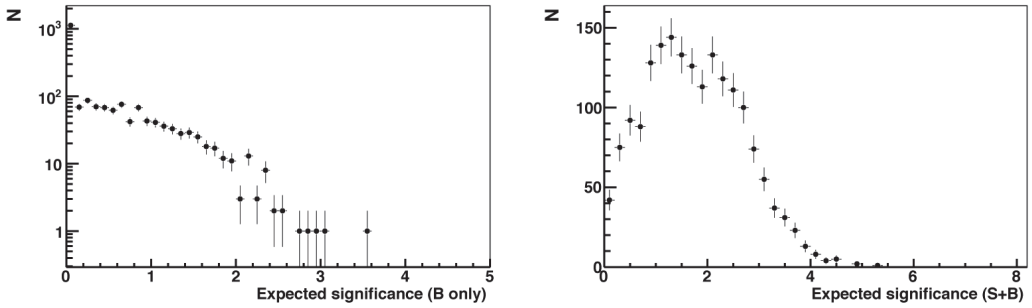

(a) (b)

Figure 5.22: Expected significance for the background-only (a) and signal + background (b) hypothesis in terms of Gaussian standard deviations for 2000 pseudo-experiments.

Finally, the single top cross section is related to the signal yield by the formula:

$$\sigma = \frac{N_s}{\epsilon \cdot B(t \to \ell\nu b) \cdot L} \tag{5.19}$$

Assuming the efficiency estimated from Monte Carlo (ϵ_{ele} = 1.69 %), $B(t \to \ell\nu b) = 0.32$ [76], and the luminosity of 36.1 pb^{-1} we obtain:

$$\sigma = 154 \pm 56(stat.) \text{ pb}$$

It is worth noting that the excess in the measured cross section with respect to data, although not dramatic for it is almost completely covered with the inclusion of systematic uncertainties (see Sec. 5.5), is a quite natural behavior of the fit. In fact the four events in the region of $\eta_{lj} > 4$, where the signal dominates, weigh a lot leading to an overall increasing of total signal yield fitted.

5.5 Results with the inclusion of systematic uncertainties

The aim of this section is to present the major systematic uncertainties affecting the analysis, both of instrumental and physics origin, and to evaluate the effect they have on the sensitivity of the cross section measurement.

5.5.1 Systematic uncertainties

The systematic uncertainties whose impact on the analysis have been evaluated are: background normalization and modeling, jet energy scale (JES) and $\not{E}_{\mathrm{T}}$ scale uncertainty, b tagging and mistagging uncertainties, signal modeling, pile up, fit procedure systematics, and in the end the luminosity uncertainty.

Backgrounds normalization and modeling

In this analysis we don't make assumptions on the overall background rate which is fitted simultaneously with the signal. Nevertheless a variation in the relative rates of different background channels can at least have an effect on the overall shape (for example the W + jets distribution in $\cos\theta^*_{lj}$ variable has a more signal-like shape than other backgrounds). So we consider:

- $t\bar{t}$: $\pm 18\%$, taken as the quadratic sum of all the statistical and systematic uncertainties evaluated in Ref. [67]; this is a conservative choice since the main systematic uncertainties of that measurement are shared by the present analysis;
- VV and single top in s- and tW-channels: $\pm 30\%$, coming from theory uncertainties;
- QCD, and $W+$ light partons: variations dictated by the data-driven procedures described in Sec. 5.3.1 and 5.3.2;
- $Z+$ light partons: variated coherently with $W+$ light partons;
- Wc: $^{+100\%}_{-50\%}$ [67];

- $VQ\bar{Q}$: $\pm 50\%$ [67].

The model uncertainties (which result in shape uncertainties) on the main backgrounds, $t\bar{t}$ and $W/Z+X$, have been evaluated using specific Monte Carlo samples, which provide simulations with varied Q^2 scale of the interaction (within half and double the nominal value, independently for $t\bar{t}$ and for $W/Z+X$), initial- and final-state radiation parameters, and fragmentation models (the latter by comparing simulations with two different MadGraph tunes, D6T and Z2 [77]).

The $W+$ light jet shapes in η_{lj} and $\cos\theta^*_{lj}$ are extracted from data, see Sec. 5.3.2. We verified on simulation that the shapes extracted from our control sample are in agreement with those in the signal region for all the processes, except for Wc channel. It shows a small difference between η_{lj} shapes in the two selections. Therefore, as a shape systematic for W + light partons, we reweight its η_{lj} distribution, taking the weights from the comparison between Wc distributions in control sample A and in the signal region.

Jet Energy Scale (JES) and $\not\!\!E_{\rm T}$ scale uncertainty

The jet energy scale uncertainty is taken into account applying a simultaneous variation of $1 \pm \alpha$ on all the jet 4-momenta, where α comes from the quadratic sum of the uncertainties on the data-driven corrections evaluated as function of the transverse energy and pseudorapidity of the jet in [66], which are better than $\pm 3.5\%$ in the whole interesting range. These terms include specific corrections for b-jet scale ($\pm$ 2-3 $\%$ depending on $p_{\rm T}$ and η) and pile-up ($\pm 1.32\%/p_{\rm T}({\rm GeV/c})$) [78, 67].

Two types of $\not\!\!E_{\rm T}$ scale uncertainty are taken into account: corrections correlated with JES and corrections uncorrelated. For the first type, after each variation in jet energy scale the $\not\!\!E_{\rm T}$ is recalculated accordingly. The second and independent source of systematic uncertainty affecting the missing transverse energy is estimated by an uncorrelated shift of the "unclustered energy" component of $\not\!\!E_{\rm T}$. The unclustered energy $\not\!\!E_{\rm T}^{\rm unc}$ is calculated by subtracting vectorially to the $\vec{\not\!\!E}_{\rm T}$ the uncorrected 4-momenta of all jets in the event and the four-momenta of all leptons which are not clustered in jets. A shift of $\pm 10\%$ is applied to the obtained $\not\!\!E_{\rm T}^{\rm unc}$ [79] and in the end leptons and jets are added back to the unclustered energy to recalculate the total $\not\!\!E_{\rm T}$.

It has not been taken into account the uncertainty on jet energy resolution, since estimated to have a small effect in the $t\bar{t}$ analyses with one electron in the final state [78, 67].

b-tagging and mistagging uncertainties

The scale factors described in Sec. 5.2.2 are varied by their data-driven uncertainties [80], propagating these variations to the formulas 5.6 and 5.7. The tight and loose working point selections are treated as fully correlated.

Signal modeling

The signal is modeled by matching the $2 \to 2$ and $2 \to 3$ diagrams at Leading Order, and then normalizing them to the NLO cross section. To estimate the uncertainty coming from the signal modeling we compare the nominal Monte Carlo sample which

uses MadGraph generator with a private production using the SingleTop generator [81]; the same matching procedure is applied, but differences stand in the Matrix Element part of the simulation, in the Parton showering and Underlying Event models (different tuning used, $D6T$ for SingleTop, $Z2$ for MadGraph).

Statistically significant differences in the total selection efficiency were observed: efficiencies are $(1.68 \pm 0.02)\%$ for MadGraph and $(1.49 \pm 0.01)\%$ SingleTop. The observed difference is believed to origin from the different tune and not from disagreement between the two generators. This is motivated by the comparison between two SingleTop signal samples performed for test with muon decays, generated with different tunes. The total selection efficiencies are $(8.06 \pm 0.10)\%$ with the Z2 tune and $(7.00 \pm 0.04)\%$ with D6T. We assign a rate systematic of -11.2%. This model uncertainty is also considered as shape systematic (5.23).

An additional uncertainty affecting the signal is the uncertainty on the W branching ratio into leptons $t \to \ell\nu b$ (with $\ell = e, \mu, \tau$), used for the extraction of the cross section 5.19. It is taken as $\pm 0.8\%$ [76].

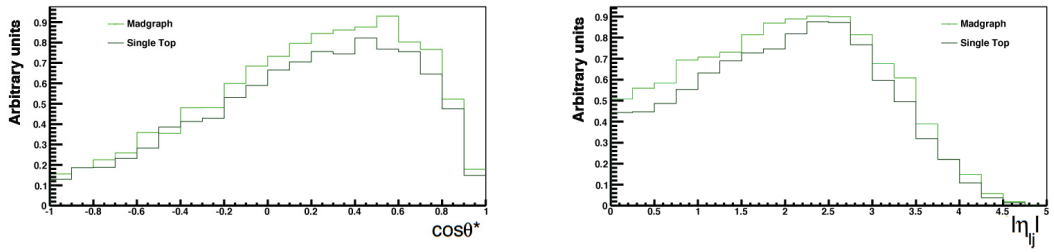

(a) (b)

Figure 5.23: $\cos\theta^*_{lj}$ and η_{lj} distributions for the signal using the Madgraph and SingleTop generators.

Pile up, fit method and luminosity uncertainties

The impact of pile-up is evaluated by comparing the standard Monte Carlo samples with no pile-up, with dedicated samples in which minimum bias interactions are superimposed to the process of interest with a probability distribution corresponding to the average over the 2010 data.

Then it is considered a conservative systematic uncertainty on the correlation between η_{lj} and $\cos\theta^*_{lj}$ (estimated as 6% from the MadGraph simulation) by comparing the fit results obtained when a true 2D template is used with those obtained when the 2D template for signal is factorized by the product of uncorrelated individual 1D templates.

Lastly, the luminosity determined from dedicated measurements [82] is known within a 4% uncertainty. This uncertainty is propagated directly to the formula 5.19.

5.5.2 Effect on signal extraction

The distributions of $\cos\theta^*_{lj}$ and η_{lj} for each channel are affected by the rate and shape uncertainties due to systematics above presented. The shape of the overall background

distribution is affected by the relative normalization of background events. Previous studies [74] have shown that the shape of $\cos\theta^*_{lj}$ is stable under variations of JES, $\not\!\!E_{\mathrm{T}}$, b-tagging, mistagging; so the effect of such systematics on the shape are considered negligible with respect to their effect on the relative normalization of the backgrounds.

Figures 5.24, 5.25, 5.26, 5.27, and 5.28 show the effect of the most relevant systematics on the signal and background model functions.

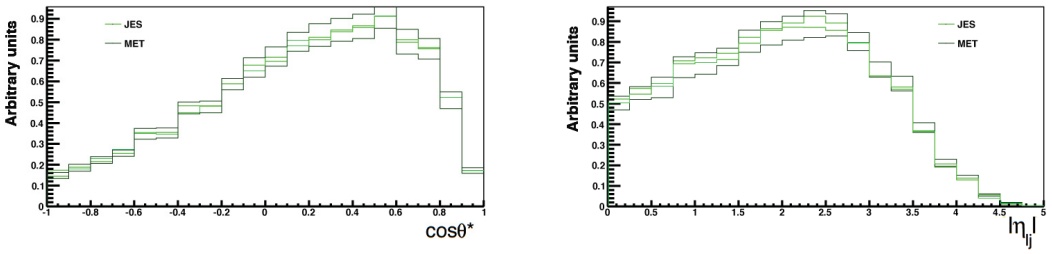

(a) (b)

Figure 5.24: JES (varied by $\pm 3.5\%$) and $\not\!\!E_{\mathrm{T}}$ ('clustered' varied by the same factor as JES, summed in quadrature with 'unclustered' $\not\!\!E_{\mathrm{T}}$ variation of $\pm 10\%$) uncertainties effect on signal $\cos\theta^*_{lj}$ and η_{lj} distributions.

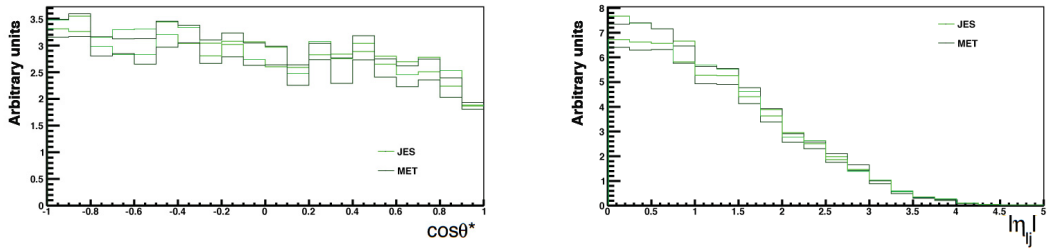

(a) (b)

Figure 5.25: JES (varied by $\pm 3.5\%$) and $\not\!\!E_{\mathrm{T}}$ ('clustered' varied by the same factor as JES, summed in quadrature with 'unclustered' $\not\!\!E_{\mathrm{T}}$ variation of $\pm 10\%$) uncertainties effect on the overall background $\cos\theta^*_{lj}$ and η_{lj} distributions.

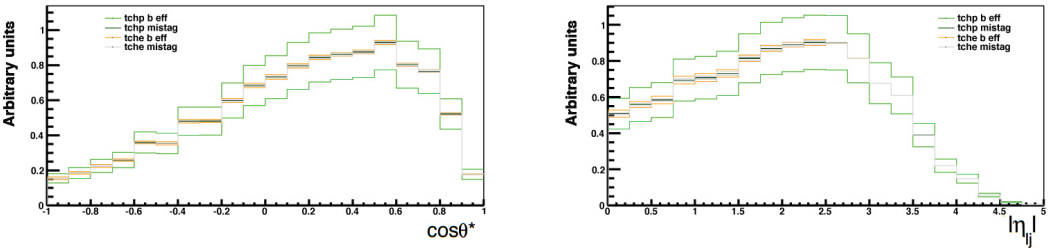

(a) (b)

Figure 5.26: Effect of the b-tagging and mistagging uncertainties on the signal $\cos\theta^*_{lj}$ and η_{lj} distributions.

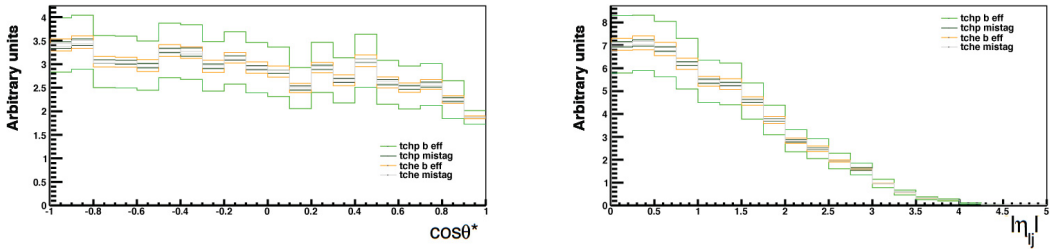

(a) (b)

Figure 5.27: Effect of the b-tagging and mistagging uncertainties on the overall background $\cos\theta^*_{lj}$ and η_{lj} distributions.

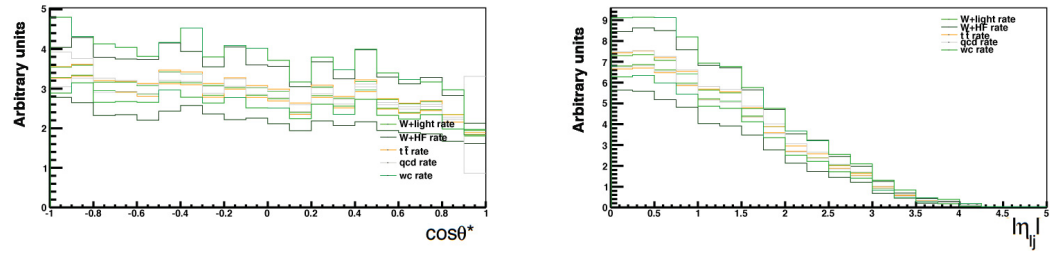

(a) (b)

Figure 5.28: $\cos\theta^*_{lj}$ and η_{lj} distributions for the overall background changing the rates of $t\bar{t}$, $W + X$ and QCD.

Procedure used with the profile likelihood method

The effect of the main systematic uncertainties on the signal yield has been evaluated applying one by one the rate/shape modifications due to these uncertainties and re-performing the likelihood fit in the new conditions for each systematics. The difference in the fitted signal yield with respect to the fit without modifications is reported In Table 5.7.

Here and in the next tables the total systematics contribution is calculated using the program at [83], which combines asymmetric systematic errors in a consistent way, assuming a non-linear dependence of the measurement result on the nuisance parameter (which the systematic error comes from); more details can be found elsewhere [84].

Table 5.8 reports the effect on the signal cross section. The significance of such measurement is extracted under the assumption that the systematic uncertainty is Gaussian, performing the quadratic sum with the statistical uncertainty and scaling the statistical significance by $\sigma_{stats}/\sqrt{\sigma^2_{stats} + \sigma^2_{syst}}$.

Procedure used with the CL_b method

In a template fit analysis the number of expected events μ_i in each bin i of the distribution of the variable of choice is compared to the observed number of events in this bin (n_i). The number of expected events in bin i is given by:

$$\mu_i = \sum_k \beta_k \cdot \alpha_{ik} \ , \tag{5.20}$$

Systematics	signal yield variation
Central value (stats)	30 $\pm$ 11 (37 %)
W+light rate	+0.7 -0.7 %
W+qq rate	-1.1 +2.7 %
W+c rate	-3.5 +2.8 %
$t\bar{t}$ rate	-0.2 +0.4 %
QCD	+6.2 -2.9 %
$b-tag$	-1.8 +2.4%
$mistag$	-0.5 +0.7%
JES (+ corr. $\not\!\!E_{\mathrm{T}}$)	-4.1 +4.1 %
Unclustered $\not\!\!E_{\mathrm{T}}$	-2.4 +0.4 %
Z+jets rate	+0.6 -0.3 %
VV rate	+0.3 -0.01 %
Single top s channel rate	-0.06 +0.3 %
Single top tW channel rate	+0.4 -0.2 %
Signal model not factorized	+2.1 %
MadGraph vs SingleTop	+12.0 %
W+light model	-3.6 %
Pile up	+1.4 %
Q^2	+7.8 -4.3 %
$ISRFSR$	+0.6 +0.2 %
$D6-Z2$	+8.2 %
Total Systematics	-10.9 +15.5 %

Table 5.7: Effect of systematics on the signal yield measured by the fit. The first number in the column refers to the effect of the up variation of the quantity considered as systematic and the second to the down variation. For example, the variation of the $t\bar{t}$ rate of +18 % has the effect of decreasing the fitted signal yield of 0.2 %, while the variation of -18 % increases the signal yield of 0.4 %.

Systematics	σ variation	significance
Central value (stats)	154 $\pm$ 56 pb (37 %)	3.25 (stat. only)
W+light rate	+0.7 -0.7 %	
W+qq rate	-1.1 +2.7 %	
W+c rate	-3.5 +2.8 %	
$t\bar{t}$ rate	-0.2 +0.4 %	
QCD	+6.2 -2.9 %	
$b-tag$	-15 +22%	
$mistag$	-0.3 +0.4%	
JES (+ corr. $\not\!\!E_{\mathrm{T}}$)	-1.4 +5.0 %	
Unclustered $\not\!\!E_{\mathrm{T}}$	-1.2 +9.0 %	
Z+jets rate	+0.6 -0.3 %	
VV rate	+0.3 -0.01 %	
Single top s channel rate	-0.06 +0.3 %	
Single top tW channel rate	+0.4 -0.2 %	
Signal model not factorized	+2.1 %	
MadGraph vs SingleTop	+12.0 %	
W+light model	-3.6 %	
Pile up	+1.4 %	
Q^2	+7.8 -4.3 %	
$ISRFSR$	+0.6 +0.2 %	
$D6-Z2$	+8.2 %	
Total Systematics	-20.1 +26.4 %	2.8 (stat. + syst.)

Table 5.8: Effect of systematics on the signal cross section and on the significance of the measurement. See Tab. 5.7 for convention about up/down variation.

where the fit parameters β_k give the ratio between the fitted fraction and the expected fraction of events for component k,

$$\beta_k = \frac{\sigma_k}{\sigma_k^{\text{pred}}}. \tag{5.21}$$

α_{ik} is the predicted number of events for bin i of process k. For fixed k, this is a template, normalized to the expected number of events. To formally describe the effect of a systematic uncertainty on the number of expected events for each uncertainty u, a strength parameter $\delta_{\text{syst},u}$ is introduced. The templates α_{ik} are written as function of $\delta_{\text{syst},u}$ such that the nominal template is reproduced for $\delta_{\text{syst},u} = 0$ and the altered templates for $\pm 1\sigma$ uncertainty for $\delta_{\text{syst},u} = \pm 1$. This is done by a linear interpolation of the templates,

$$\alpha_{ik}^{\text{syst}}(\vec{\delta}_{\text{syst}}) = \alpha_{ik} + \sum_u |\delta_{\text{syst},u}| \cdot (\alpha_{iku,\text{sign}(\delta_{\text{syst},u})}^{\text{syst}} - \alpha_{ik}) \, . \tag{5.22}$$

Therein, u runs over all sources of systematic uncertainties and $\alpha_{iku,\pm 1}^{\text{syst}}$ is the prediction for bin i of process k affected by $+1\sigma$ or -1σ of uncertainty u. They are obtained by running the same analysis procedures on samples which have been altered to include the respective uncertainty at a strength of $\pm 1\sigma$. For some uncertainties, the nominal samples have been altered as described in the following sections, for other uncertainties, dedicated samples have been produced.

In order to prevent unphysical negative predictions for a process, the linear interpolation is cut off at a bin content of zero: whenever $\alpha_{ik}^{\text{syst}}(\vec{\delta}_{\text{syst}})$ calculated according to equation 5.22 has a value below zero, zero is used instead in equation 5.20 to calculated μ_i.

To test the signal + background hypothesis against the background only (null) hypothesis we define a likelihood ratio test statistic Q as:

$$Q = -2ln\left(\frac{L_{s+b}}{L_b}\right) \tag{5.23}$$

Here L_{s+b} is the likelihood function defined in equation 5.15, while L_b is the background only likelihood (with $N_s = 0$). We generate hundreds of thousands of pseudo-experiments (from the modified templates $\alpha_{ik}^{\text{syst}}$) and evaluate the test statistics Q with best fit values for N_s and N_b on toy background samples (Q_b). For each pseudo experiment, statistics is fluctuated according to a Poisson distribution around the mean expected value. Then we calculate Q on data and define the confidence level CL_b:

$$CL_b \;\; = \;\; N_{Q_b > Q_{obs}}/N \tag{5.24}$$

where $N_{Q_b > Q_{obs}}$ is the number of the generated experiments which have a Q value greater than the measured one, and express the compatibility of the observation with the background only hypothesis, and N is the total number of generated pseudo-experiments. The sensitivity of the analysis (in terms of Gaussian n_σ) is related to the confidence level CL_b by the formula:

$$n_\sigma = \sqrt{2} \cdot \mathrm{erf}^{-1}(2 \cdot CL_b - 1) \quad \text{with} \quad \mathrm{erf}(z) = \frac{2}{\pi} \int_0^z e^{-t^2} dt \tag{5.25}$$

We implement the method with the use of the *theta* framework [75]. The median and central 68% range of the expected significance distribution for signal + background hypothesis are shown in Table 5.9 together with the observed significance. Figure 5.29 shows the Q distribution for the signal-only and signal+background hypotheses.

expected (range)	observed
1.26 (0.2,2.3)	3.1

Table 5.9: Median and central 68% range of the expected significance values in the signal + background hypothesis and observed significance.

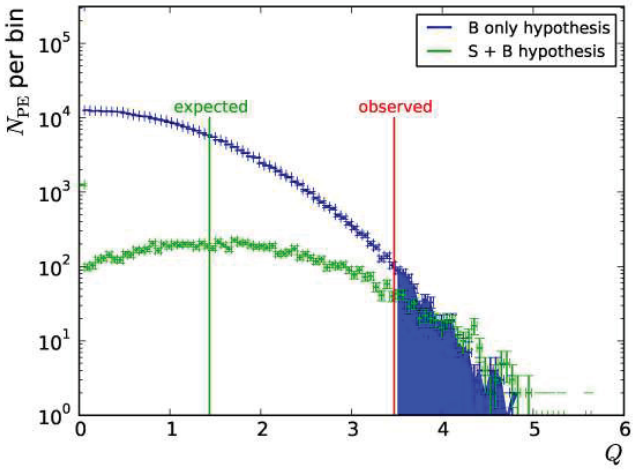

Figure 5.29: Q distribution for pseudo-experiments thrown in background-only and signal + background hypotheses.

5.6 Conclusions and V_{tb} measurement

5.6.1 Combination with muon channel

The cross section measurement in the electron channel is combined with an analogous measurement in the muon channel only [85]. The procedure adopted for signal extraction

is a simultaneous maximum likelihood fit on $\cos\theta^*_{lj}$ and η_{lj} in the two channels. We define a combined likelihood function in which we fit simultaneously the parameter N_s written as $f_e N_s + f_\mu N_s$, where f_e and f_μ are the fraction of signal events expected in the electron and muon channel, respectively, taken from simulation and adding up to 1.0. Now the variable N_s represents the measured sum of the single top event yields in the muon and electron channels.

The statistics and systematics evaluation has been performed repeating the procedure described in previous sections for the combined measurement. All the systematics are considered fully correlated for the muon and electron channels, and therefore variated coherently up/down at the same time for both channels, with the exception of the data-driven uncertainties on the QCD estimations, treated as uncorrelated.

We obtain the following cross section measurements:

$$\sigma = 103 \pm 42(stat.)\,^{+25}_{-28}(syst.) \pm 11(lumi.) \text{ pb} \qquad \text{muon channel}$$
$$\sigma = 154 \pm 56(stat.)\,^{+40}_{-46}(syst.) \pm 17(lumi.) \text{ pb} \qquad \text{electron channel}$$
$$\sigma = 123 \pm 34(stat.)\,^{+30}_{-34}(syst.) \pm 14(lumi.) \text{ pb} \qquad \text{combined}$$

In conclusion the analysis confirms the Tevatron observation of single top production, with a significance of 2.5 σ and 3.1 σ in the muon and electron channels respectively, and a combined significance of 3.7 σ. This measurement is consistent with the standard model expectation.

5.6.2 $|V_{tb}|$ measurement

Under the assumption that $|V_{td}|$ and $|V_{ts}|$ are much smaller than $|V_{tb}|$ we can express the latter as $\sqrt{\frac{\sigma^{exp}}{\sigma^{th}}}$. A Bayesian method is used to extract a 95% C.L. lower limit on $|V_{tb}|$. We use a flat prior for the single top cross section which corresponds to a flat prior in $|V_{tb}|^2$. The posterior in the model parameters is (up to an overall normalization) given by

$$p(\beta_s, \beta_{b,\mu}, \beta_{b,e}, \delta_i|\text{data}) = \prod_{i=1}^{400} \text{Poisson}(n_i|\mu_i)\pi(\delta_u). \tag{5.26}$$

The index i runs over all 400 bins of the two-dimensional template, n_i is the number of observed events in this bin and Poisson$(n|\lambda)$ is the Poisson probability to observe n events, given mean λ. The expected number of events μ_i depends on the scaling factors β_i and the shape-changing nuisance parameters δ_u as given in equations 5.20 and 5.22. $\pi(\delta_u)$ denotes the prior used for the shape-changing nuisance parameters δ_u. As priors, we choose to use independent Gaussian functions around 0 with width 1, motivated by the template interpolation (see eq. 5.22) which yields the $\pm1\sigma$ modified templates for values $\delta_u = \pm 1$.

To include the uncertainty on the cross section, the term in the sum on the right hand side of equation 5.20 which corresponds to the signal content, $\beta_s \cdot \alpha_{is}$, is modified by an additional factor $\beta_{\text{vtb-xs}}$:

$$\mu_{i,s} = \beta_s \cdot \beta_{\text{vtb-xs}} \cdot \alpha_{is}.$$

prior in $\lvert V_{tb}\rvert^2$	95% C.L. lower limit on $\lvert V_{tb}\rvert$
flat, $\lvert V_{tb}\rvert^2 \leq 1$	0.63

Table 5.10: 95% C.L. lower limit on $|V_{tb}|$ using a fully Bayesian technique.

This additional parameter $\beta_{\text{vtb-xs}}$ encodes the imprecise knowledge of the single top t-channel cross section, assuming a perfect knowledge of $|V_{tb}|$. As prior of this parameter, a Gaussian around 1.0 with a width if 3.9% is used. This corresponds to the uncertainty of the most precise cross section calculation for single top available [86]. From the full posterior given in eq. 5.26, we obtain the marginal posterior for β_s by marginalization, i.e., integration over all other parameters. Technically, this is done using a Markov-Chain Monte-Carlo technique, more details can be found in Ref. [75] and references therein. Within the framework of the standard model, V_{tb} is a diagonal element of a unitary matrix and $|V_{tb}|$ can therefore never exceed unity. This is true even if extending the standard model by additional (quark) generations. Therefore, we give a lower limit on $|V_{tb}|$ using the constraint $|V_{tb}| \leq 1$ by imposing a flat prior for β_s which vanishes for $\beta_s > 1$. From the marginal posterior in β_s, the 5% quantile is the 95% C.L. lower limit on $|V_{tb}|$. The results are summarized in Table 5.10.

5.6.3 Combination with BDT analysis

In conclusion, the analysis so far described (called 2D, because it is two-dimensional fit based) is in turn combined with a multivariate analysis (using boosted decision trees, BDT [87]). The combination of the results is performed by calculating a weighted average where the weight is chosen such that the resulting uncertainty is minimized. This method is known as best linear unbiased estimator (BLUE) [88]. For this method, the full covariance matrix has to be known, i.e., the statistical and systematic uncertainties, including their correlation between the analyses. The procedure adopted in detail is described in [89]. The result after the combination (see the PAS in [90] and the paper [52]) is shown in Fig. 5.30 where the comparison with Tevatron measurements and Standard Model prediction is also shown. The cross section obtained is:

$$\sigma = 83.6 \pm 29.8(stat. + syst.) \pm 3.3(lumi.) \text{ pb} \quad \text{combined} \tag{5.27}$$

From the combined measurement, it is has also been evaluated the $|V_{tb}|$ CKM element without assuming the constraint $|V_{tb}| \leq 1$, obtaining:

$$|V_{tb}| = \sqrt{\frac{\sigma^{exp}}{\sigma^{th}}} = 1.16 \pm 0.22(exp.) \pm 0.02(th.)$$

where σ^{exp} is taken from Eq. 5.27 and $\sigma^{th} = 62.3^{+2.3}_{-2.4}$ pb is the NLO prediction in the 5-flavors scheme.

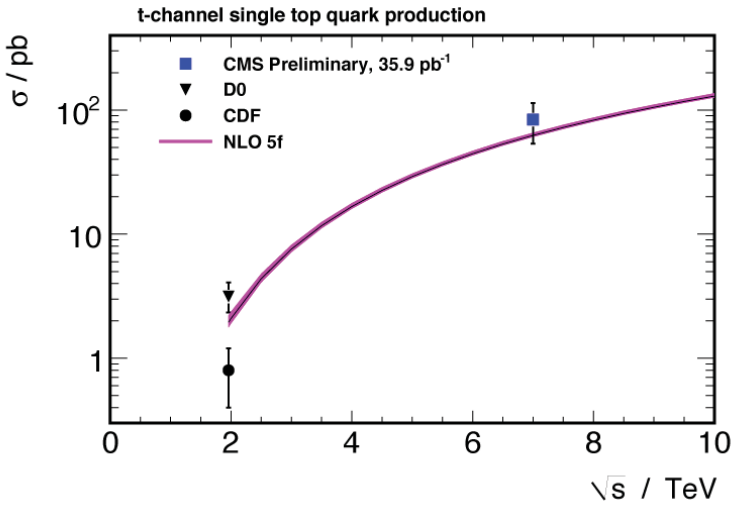

Figure 5.30: Comparison of the t-channel single top cross section obtained by CMS, the NLO Standard Model prediction and the measurements obtained at Tevatron.

Chapter 6

Analysis update with 920.7 pb^{-1} of 2011 data

6.1 Introduction

This chapter presents a preliminary update of the analysis described in chapter 5 [85, 90]. Due to the much higher statistics accumulated in the 2011 data taking, this measurement enters the regime where systematics uncertainties become dominant over statistics uncertainties for the cross section measurement. The strategy of this analysis is based on a template maximum likelihood fit on the absolute value of the pseudorapidity of the light jet stemming from the parton recoiling against the top quark η_{lj}, which allows to discriminate between single top t-channel and its main background contributions. The choice of fitting η_{lj} variable only and not η_{lj} and $\cos\theta^*_{lj}$ together comes mainly because we want to reserve the $\cos\theta^*_{lj}$ variable for top polarization studies and also because we don't want to rely on its more problematic modeling in Monte Carlo simulations. More details in Sec. 6.5.

The other main difference with respect to the old analysis strategy is that an additional cut in the $M_{bl\nu}$ variable is performed to define a signal region and a sideband region. As described in Sec. 6.5.1, $M_{bl\nu}$ is the invariant mass of the reconstructed lepton, b-tagged jet and neutrino, whose transverse momentum is inferred from the missing transverse energy and longitudinal momentum is obtained from the ansatz of the kinematic closure of the event which is verified in case of t-channel processes. The use of the sideband allows to constrain the rate of the $W+$ jets component of the background and to extract a data driven shape for $W+$ jets η_{lj}.

Following the same pattern of the previous chapter, the first part is dedicated to the event selection and the Monte Carlo samples involved, then the top quark reconstruction and data-driven techniques for QCD and W + jets background estimation will be illustrated. Afterwards the one dimensional fit method and the statistical evaluation are presented, and in the end there is the description of systematic uncertainties and the final results obtained. Throughout the chapter it will be stressed the difference with respect to the 2010 analysis, omitting details about procedures already explained before.

6.2 Samples and Event Selection

6.2.1 Data and Monte Carlo samples

This study is based on an integrated luminosity of 920.7 pb^{-1}, known with an accuracy of 5 % [98]. The t-channel events from Monte Carlo simulation used in this study have been generated with the POWHEG event generator, separately for events where a single top or a single anti-top is produced. MC simulated datasets are normalized to the NLO cross section of 41.9 (22.6) pb for events with top (anti-top), see the second reference of [40].

Table 6.1 summarizes the Monte-Carlo data samples for signal and backgrounds, and provides the number of events and cross section for each sample. All the cross sections have been taken from the references listed in Table 6.1 or, when no reference is given, from the generator itself. The MC W/Z samples are divided in the $W/Z + (u, d, s, g)$ (light flavours) and the $W/Z + c, b$ (heavy flavours) components (algorithmic matching). To each jet is associated the flavour of the quark that is within $\Delta R = \sqrt{((\Delta\phi)^2 + (\Delta\eta)^2)} < 0.5$. An event is classified as $W/Z + b$ if at least 1 b-flavoured jet is present, as $W/Z + c$ if no b-flavoured jet is present, but at least 1 c-flavoured jet is present, and finally W + light flavour if none b or c are present.

The simulation of the full detector response is based on GEANT 4 [92], and assumes realistic alignment and calibration, tuned on data. In Monte Carlo samples a flat pile up distribution is simulated. The impact of pile-up on this analysis is estimated in Sec. 6.6.

6.2.2 Event selection

The events selection is optimized for the final state topology of the t-channel production, requiring exactly one electron, one b-jet coming from top decay, and one light flavoured jet recoiling against the top quark. As in 2010 analysis the lepton selection criteria and the quality cuts for central jets are taken equal to those agreed for $t\bar{t}$ analyses in the single-electron channel. The reconstruction of all physics objects is done through an algorithm named Particle Flow (PF) [65], which uses information of all the sub-detectors when reconstructing each physics object.

Trigger selections

The first steps of the selection are the same as in the 2010; substantial differences finds in the use of triggers. Different trigger paths (single-electron and electron + jets) are used depending on the run range to follow the different luminosity conditions through the whole data-taking: triggers requiring at least an electron with measured E_{T} above 25 or 27 GeV/c and requiring a calorimetric isolation and electron isolation criteria are used for the first runs of 2011 data-taking; triggers requiring at least one electron as before plus at least one jet with $p_{\mathrm{T}} > 30$ GeV/c and $\eta < 2.4$ (called CentralJet30 triggers) are used for higher luminosity runs; triggers with the additional request that at least one b-tagged

Process	$\sigma[\mathrm{pb}] \cdot \mathcal{B}$
single top, t channel (t, inclusive)	41.9 (NNLO) [40]
single top, t channel ($\bar{t}$, inclusive)	22.6 (NNLO) [40]
single top, s channel (t, inclusive)	3.19 (NNLL) [39]
single top, s channel ($\bar{t}$, inclusive)	1.44 (NNLL) [39]
single top, tW channel (t, inclusive)	7.9 (NNLO) [40]
single top, tW channel ($\bar{t}$, inclusive)	7.9 (NNLO) [40]
$t\bar{t}$	165 (NNLL) [38]
$W(\rightarrow l\nu) + jets$	31314 (NNLO) †
$Z/\gamma^*(\rightarrow l^+l^-) + jets$ (*)	3048 (NNLO) †
WW	43 (LO)
WZ	18.2 (LO)
ZZ	5.9 (LO)
$b/c \rightarrow e$, $20 < \hat{p}_T < 30$ GeV	132160 (LO)
$b/c \rightarrow e$, $30 < \hat{p}_T < 80$ GeV	136804 (LO)
$b/c \rightarrow e$, $80 < \hat{p}_T < 170$ GeV	9360 (LO)
EM-enriched QCD, $20 < \hat{p}_T < 30$ GeV	2454400 (LO)
EM-enriched QCD, $30 < \hat{p}_T < 80$ GeV	3866200 (LO)
EM-enriched QCD, $80 < \hat{p}_T < 170$ GeV	139500 (LO)
γ+jets, $40 < H_T < 100$ GeV	23620 (LO)
γ+jets, $100 < H_T < 200$ GeV	3476 (LO)
γ+jets, $H_T > 200$ GeV	485 (LO)

(*) $m_{ll} > 50$ GeV

† separated into sub-processes with an algorithmic matching, see text

Table 6.1: Monte Carlo datasets used in this analysis. The samples are generated either inclusively or with a final state restricted to the leptonic mode, including electrons, muons, and taus. Where no references are given, the cross sections come from the generator itself if LO, from FEWZ [68] if NNLO, and from MCFM 5.8 [93] if NLO.

jet is present (called BTagIP since the b-tagging algorithm used is based on impact tracks parameter) are in the end used for the latest runs.

Since these trigger paths are not foreseen in simulation, a data-driven estimation of their impact is evaluated by calculating "turn-on" curves that are used to re-weight Monte Carlo events . The curves for CentralJet30 triggers are obtained as the ratio between the jet p_{T} distribution on data for events passing the trigger in exam and the jet p_{T} distribution for events passing a reference trigger (with no requests on jets). Similarly, the BTagIP turn-on curves are obtained as the ratio between b-tagging discriminators distributions for events passing the BTagIP trigger and for events passing a reference trigger (in this case the CentralJet30 trigger). More details could be found at [94]. In Fig. 6.1 the turn-on curves for CentralJet30 and TCHP b-tagger triggers are shown.

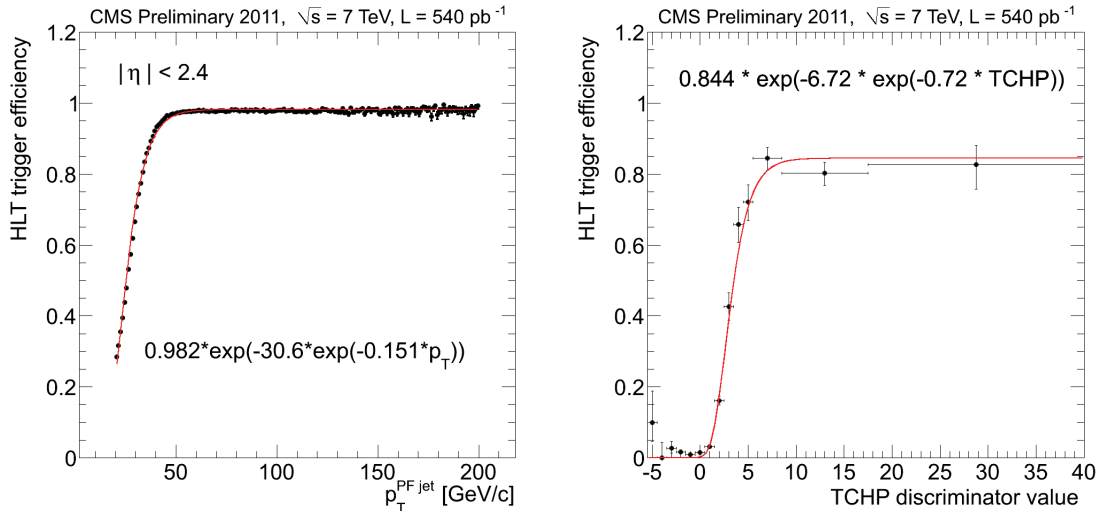

(a) (b)

Figure 6.1: Turn-on curves for CentralJet30 and TCHP b-tagger triggers, with the corresponding parameterization.

Electrons

The only difference with respect to 2010 electron selection is the cut on "particle flow relative isolation" ($I_{\mathrm{rel}}^{\mathrm{PF}}$), defined as

$$I_{\mathrm{rel}}^{\mathrm{PF}} = \frac{I_{\mathrm{Photon}}^{\mathrm{PF}} + I_{\mathrm{ChargedHadron}}^{\mathrm{PF}} + I_{\mathrm{NeutralHadron}}^{\mathrm{PF}}}{p_T}, \tag{6.1}$$

where $I_{\mathrm{Photon}}^{\mathrm{PF}}$, $I_{\mathrm{ChargedHadron}}^{\mathrm{PF}}$ and $I_{\mathrm{NeutralHadron}}^{\mathrm{PF}}$ are the sum of the transverse energies associated by the particle flow algorithm to photons, charged and neutral hadrons in a cone of size $\Delta R < 0.4$ around the lepton direction. Tight electrons are selected by the requirement $I_{\mathrm{rel}}^{\mathrm{PF}} < 0.1$ and $I_{\mathrm{rel}} < 0.2$. Also in the definition of loose electrons, we require $I_{\mathrm{rel}}^{\mathrm{PF}} < 0.2$.

It is required the presence of exactly one tight electron, vetoing events with additional loose electrons (to reduce contribution of dilepton events, which can come from $t\bar{t}$ or Drell-Yan processes), removing the Z veto from the preceding analysis.

Jets

Apart from the same requests of 2010 analysis, only jets are considered with calibrated transverse momentum larger than 30 GeV/c, within $|\eta| < 4.5$. Fig. 6.2 shows the jet multiplicity after the lepton selection, in data and simulation.

For what concerns b-tagging, the updated 2011 data/MC scale factors (and corresponding uncertainties) on efficiencies and mistag rates have been evaluated in [95]. The b-tagged jet multiplicity in events with two jets is shown in Fig. 6.3 for data and simulated samples.

Differently with respect to 2010 analysis, we apply no more the b-veto. This choice has been dictated by a double motivation: first we want to limit as much as possible the b-tagging and mistag uncertainties, which are the biggest source of systematics as we noticed in 2010 analysis; secondly we prefer not to tighten the selection too much to have enough statistics for studies on control samples.

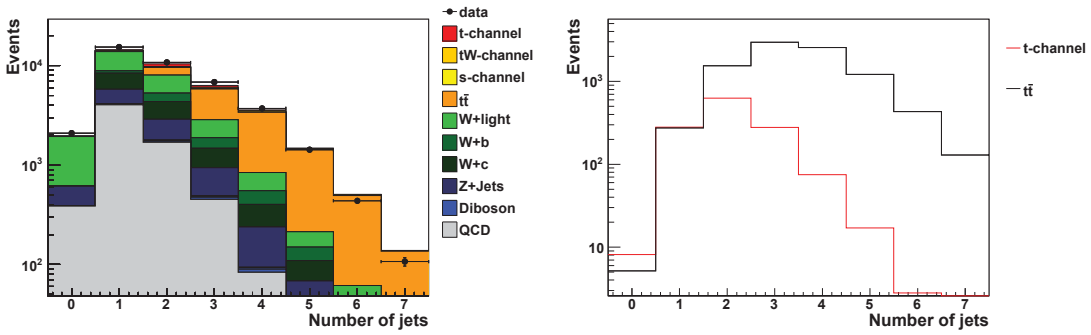

(a) (b)

Figure 6.2: Jet multiplicity after the lepton counting in data and simulation, and for signal and $t\bar{t}$ events only. In all the plots in this chapter we indicate with W+b and W+c the W events in which there is at least one b-jet and one c-jet, respectively.

Transverse W boson mass and missing transverse energy ($\not\!\!E_{\mathrm{T}}$)

We refer to the 2010 section 5.2.2 for the W transverse mass definition. The $\not\!\!E_{\mathrm{T}}$ distribution revealed to be more appropriate for QCD background description, both for better MC/data agreement and because the fit to this variable (see Sec. 6.4.1) allows to reject more QCD than the M_T fit does. Figure 6.4 shows the shape of the $\not\!\!E_{\mathrm{T}}$ distribution after the preceding selection, for Monte Carlo and data (a) and for signal and QCD (b).

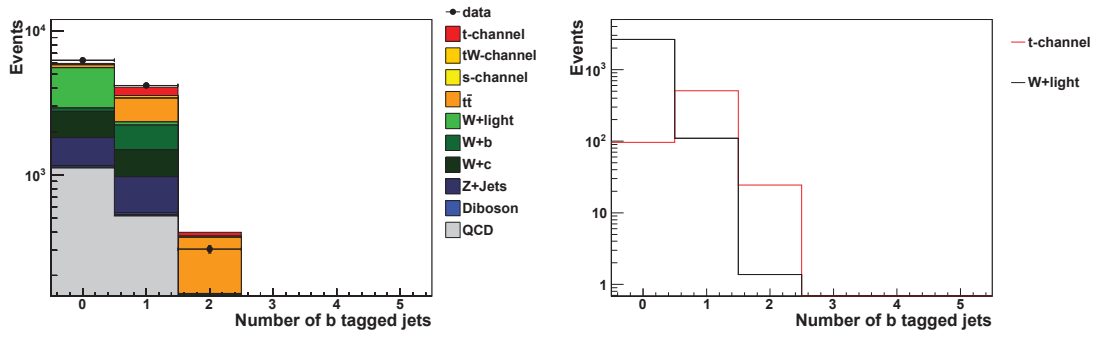

(a) (b)

Figure 6.3: Number of jets for $D_{TCHP} > 3.41$ for data and simulation and for signal and W + light partons only, after the 2 jets request.

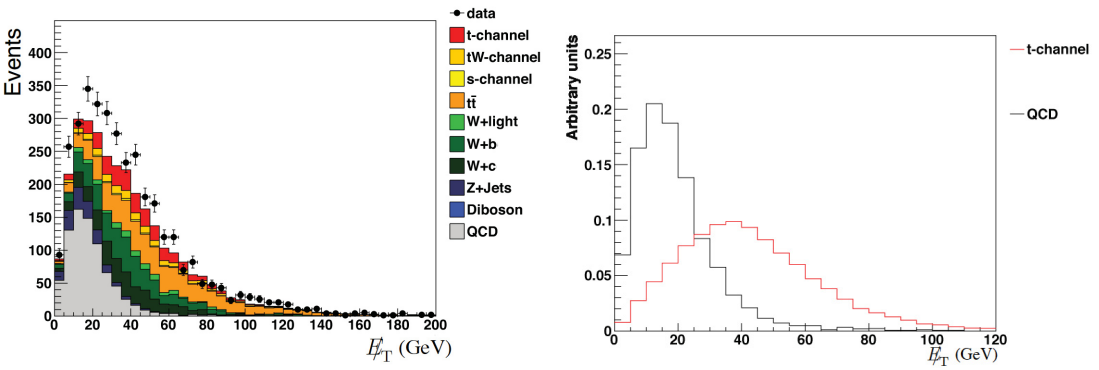

(a) (b)

Figure 6.4: Transverse mass after the entire selection minus the $\not\!\!E_T$ cut, in data and Monte Carlo and for signal and QCD.

The optimization of the threshold with a template fit on $\not\!\!E_T$ (Sec. 6.4.1) analogous to that applied in 2010 analysis leads to the choice $\not\!\!E_T > 35$ GeV.

Selection results

The number of selected events, step by step, in data and Monte Carlo is shown in Table 6.2. It should be noticed a discrepancy between data and MC yields even after all cuts have been performed. To better understand this difference, control samples for W+jets and $t\bar{t}$ are considered and a study of tagged jets multiplicity is made (see Sec. 6.3). Anticipating the conclusion, also supported by the studies in the muonic decay channel, it seems that the W + jets component is not correctly simulated in Monte Carlo, and for this reason the final extraction of the signal yield for cross section measurement is preformed fitting simultaneously also the W and $t\bar{t}$ components of backgrounds (details in Sec. 6.5.2).

Process	1 iso e, 0 μ	2 jets	$MET > 35$ GeV	1 tight b tag
single top, t channel	2386	1134	692	287.8 ± 1.7
single top, s channel	160.2	77.5	47.8	22.4 ± 0.5
single top, tW	1754	587	374	134.3 ± 1.1
$t\bar{t}$	11798	2328	1680	716 ± 5
W+jets	435480	78366	40246	728 ± 20
Z+jets	110534	14460	919	25.6 ± 1.4
VV	3522	989	529	16.3 ± 0.3
QCD	272365	68062	5125	226.5 ± 14
Total background	835613	164871	48921	1870 ± 25
Signal + background	837999	166005	49613	2158 ± 25
Data	207881	37346	13563	1606 ± 40

Table 6.2: Number of events surviving each selection step, in data and Monte Carlo (normalized to 920.7 pb^{-1}). In this table the event yields don't take into account the turn-on curves efficiencies and the b-tagging efficiencies, varying event by event.

Data-driven scale factors for b-tagging and mistagging

As in the 2010 analysis, for the tight and loose b-tagging working points, estimates of the efficiencies of true and fake b-jets identification are used, and can be found in [80], as a function of p_T and η_{lj}. To correct the Monte Carlo mistag rates and b-tagging efficiency each event is weighted by the probability of it passing the cuts given the appropriate scale factors. Here we go into the details of the procedure since it is slightly different from the 2010 analysis.

For a jet the probability to be tagged and not to be tagged varies as follows:

$$\begin{aligned} \epsilon_{b\,tag(mistag)} &\rightarrow SF \cdot \epsilon_{b\,tag(mistag)} \\ \epsilon_{b\,tag(mistag)} &\rightarrow (1 - SF) \cdot \epsilon_{b\,tag(mistag)} \end{aligned} \tag{6.2}$$

Given the number of jets n_l stemming from light quarks, n_c from c quarks, and n_b from b quarks, the probability P for an event to pass the b-tagging requirements is:

$$P^{MC} = \Sigma_{tl=1}^{nl}\Sigma_{tc=1}^{nc}\Sigma_{tb=1}^{nb} C \cdot \epsilon^{tl}(1-\epsilon)^{nl-tl}\epsilon^{tc}(1-\epsilon)^{nc-tc}\epsilon^{tb}(1-\epsilon)^{nb-tb}S \tag{6.3}$$

where S is a 0 if the event does not pass the selection, 1 otherwise, and C is the combinatorics factor. A scale factor is then applied on each event to recalculate the probability on MC. Such scale factor is derived substituting Eq. 6.2 in Eq.6.3 to get P^{Data}. Finally we define a weight as:

$$b - weight = P^{Data}/P^{MC} \tag{6.4}$$

More details could be found at [96].

Data-driven scale factors for pile up

To take into account the effect of the pile up on the analysis and to correct the different pile up conditions simulated in Monte Carlo with respect to distributions measured on data, data-driven scale factors are taken into account according to CMS prescriptions. Therefore for each simulated process, an appropriately defined function remodels the generated pile-up distribution to take the shape of the data distribution. The weights for each simulated event are therefore assigned according to this function, which is given as input the number of pile up interactions for that event.

6.3 Control samples

This section provides a summary for all the control samples used for the analysis. The data-driven background estimation procedures are described in Sections 6.4.1, 6.4.2.

Process	entries
t-channel	33.7
tW-channel	23.9
s-channel	1.12
$t\bar{t}$	63.9
$W+$ light partons	7851.1
$Z+$ jets	163.6
Wc	738.9
Wb	37.6
QCD	578.9
Total	9492.7
Data	8812

Table 6.3: Expected for the main processes (from simulation) and overall observed (from data) event yields in Control Sample A.

6.3.1 W + light flavor enriched sample

The W + light flavour background is studied in detail in the Control Sample A where 2 jets are selected and both fail the TCHP loose threshold (the zero-tag bin in jet multiplicity), running on 214.1 pb^{-1}. Table 6.3, reports the events yield for MC and Data in such control sample. The QCD yield is determined with a fit to the $\not\!\!E_{\mathrm{T}}$ distribution (Fig. 6.5) described in section 6.4.1. This procedure yields the following predictions for the number of QCD events passing the $\not\!\!E_{\mathrm{T}}$ threshold:

$$N_{qcd} = 454 \pm 21(stat.) \tag{6.5}$$

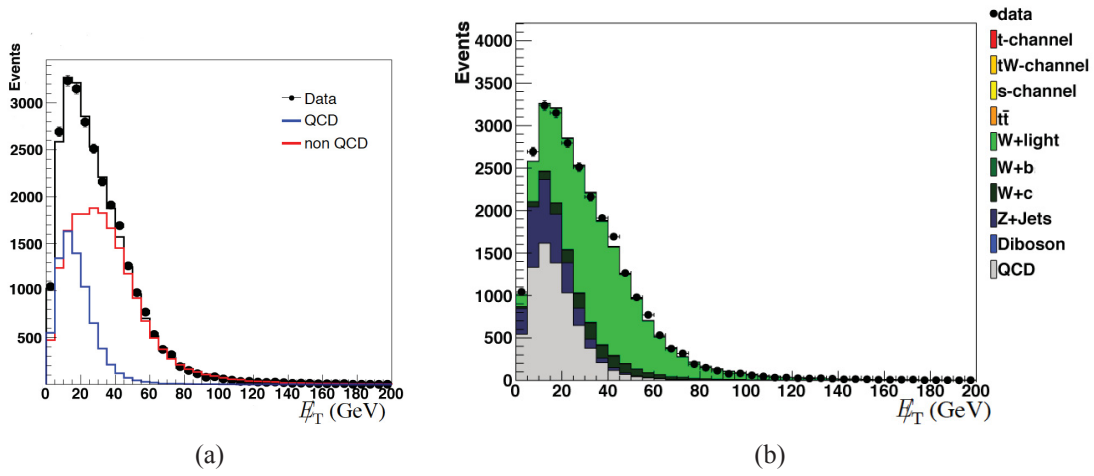

(a) (b)

Figure 6.5: $\not\!\!E_{\mathrm{T}}$ fit with the data-driven template for QCD (a) and $\not\!\!E_{\mathrm{T}}$ distribution rescaled to the fit results (b).

Figures 6.6 and 6.7 show the $\cos\theta^*_{lj}$, η_{lj} and $M_{bl\nu}$ distributions in the control sample A, in which the shape for QCD is extracted from the anti-isolated sample. This sample

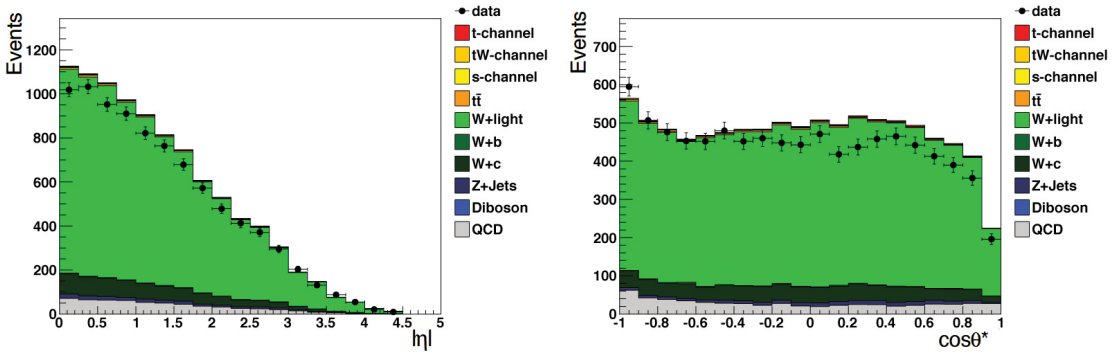

(a) (b)

Figure 6.6: η_{lj} and $\cos\theta^*_{lj}$ distributions in Control Sample A. In this sample η_{lj} is taken as the sum of both jets' η.

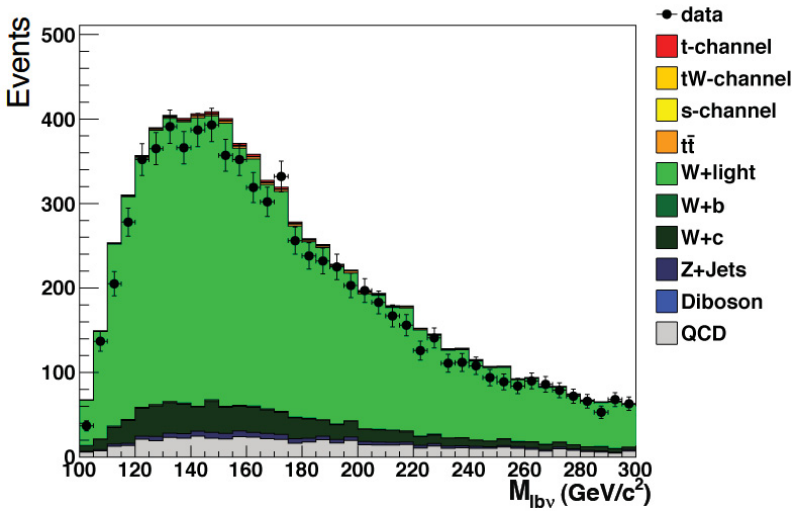

Figure 6.7: Reconstructed top mass, $M_{bl\nu}$, in Control Sample A.

is not directly used in the measurement to extract the W + jets scale factors, but only to study in detail how much its modeling in Monte Carlo is reliable. After the qcd extraction procedure, the data and MC yields agree within order of 7 %. The agreement in shapes is reasonable for η_{lj} and $M_{bl\nu}$, while $\cos\theta^*_{lj}$ seems not to be well simulated. This has not dramatic consequences on the signal extraction procedure, since $\cos\theta^*_{lj}$ is not used to measure the signal yield, but certainly it requires further investigations.

6.3.2 $t\bar{t}$ enriched sample

A $t\bar{t}$ enriched control sample is defined selecting 3 jets and requiring that 2 of them pass the TCHP tight threshold. We also refer to this sample as 3-Jet 2-Tags bin. The

Process	entries
t-channel	12.4
tW-channel	10.8
s-channel	1.68
$t\bar{t}$	224.8
$W+$ light partons	0.0
$Z+$ jets	0.65
Wc	0.48
Wb	12.7
QCD	14.2
Total	277.7
Data	279

Table 6.4: Expected for the main processes (from simulation) and overall observed (from data) event yields in 3-Jets 2-Tags Sample.

highest TCHP tagged jet is used for reconstruction of top quark hypothesis. Table 6.4 reports the event yields for MC and the overall yield for data in this control sample.

This sample is used to study the data/MC agreement both in yield and in shape for the most important variables in the analysis. Figures 6.8 and 6.9 show the $\cos\theta^*_{lj}$, η_{lj} and $M_{bl\nu}$ data/MC comparison. For what concerns $M_{bl\nu}$ the agreement seems to be not perfect, even if the Kolmogorov-Smirnov test is reasonable (giving a KS probability of 90%) and the tail regions looks like being well reproduced. Therefore, we trust at least the acceptance for $M_{bl\nu}$ variable, while it will not be used as fit variable.

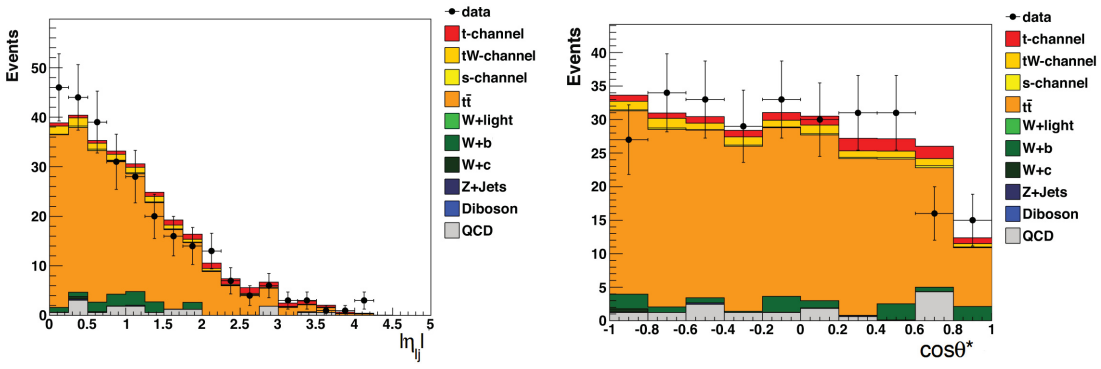

(a) (b)

Figure 6.8: η_{lj} and $\cos\theta^*_{lj}$ in $t\bar{t}$ control sample.

6.3.3 Signal region and W + heavy flavours enriched sideband region

We begin this section addressing the yield discrepancy problem mentioned in Sec. 6.2.2 and in the end presenting a way out for a reliable background description. To understand the discrepancy the b-tagged jet multiplicity plots have been studied. Figure 6.10 shows that there is an excess of data in the bins where W channels are present, while $t\bar{t}$ enriched

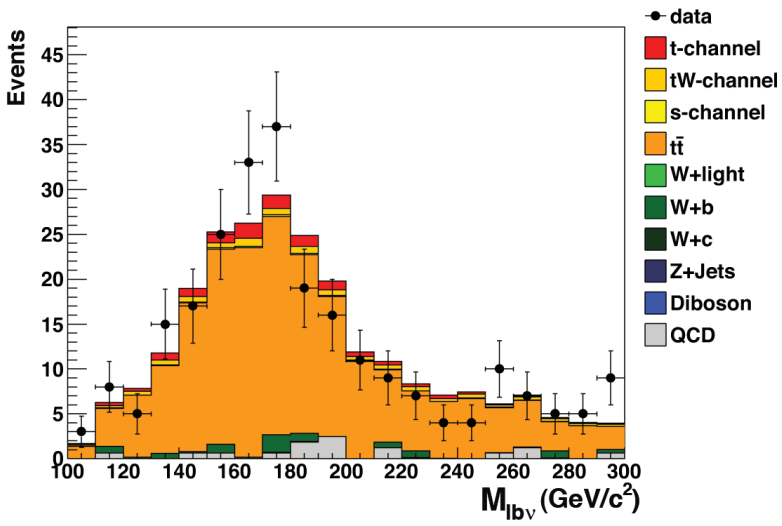

Figure 6.9: $M_{bl\nu}$ in $t\bar{t}$ control sample.

regions seem to be under control. Moreover, since in $t\bar{t}$ and W + light flavours control samples we find an excellent Data / MC agreement, and since the W channel dominating in figure is W + heavy flavours component, we can are driven to suppose that the main reason behind the discrepancy is the W + heavy flavours background.

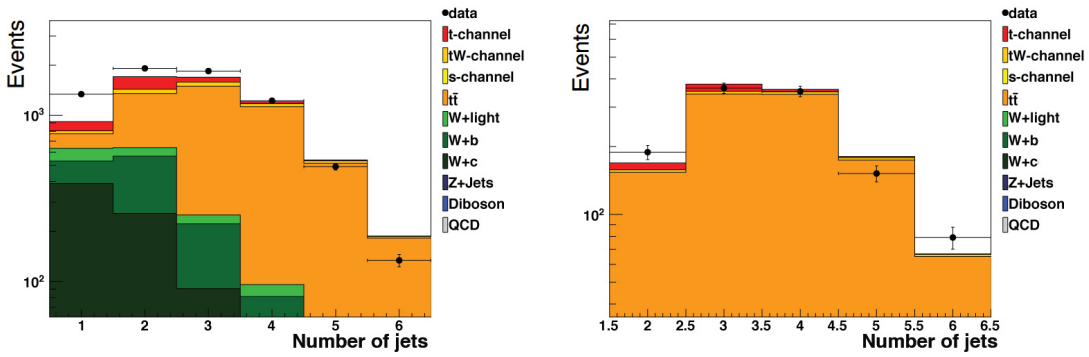

(a) (b)

Figure 6.10: Jet multiplicity in events with 1 (a) or 2 (b) jets passing the TCHP tight (3.41) threshold.

Another group independently obtained scale factors and the corresponding range of variation with a simultaneous extraction of $t\bar{t}$ and of its main background [59], finding for example for the 2 jets bin

$$SF(Wcx) = 1.21^{+0.28}_{-0.27} \quad (6.6)$$

$$SF(Wbx) = 1.66 \pm 0.6 \quad (6.7)$$

These scale factors need to be extrapolated to the kinematic region of interest, i.e. the

Process	entries signal region (SR)	entries sideband (SB)
t-channel	172.8	26.0
tW-channel	57.6	35.8
s-channel	11.7	4.8
$t\bar{t}$	322.8	199.2
$W+$ light partons	24.8	45.2
$Z+$ jets	6.4	8.5
Wc	95.0	84.0
Wb	122.7	140.7
QCD	34.7	41.4
Total	848.6	585.5
Data	943	663

Table 6.5: Expected for the main processes (from simulation) and overall observed (from data) event yields in Signal Region and Sideband Region. The QCD yield is rescaled to the $\not{E}_{\mathrm{T}}$ fit results.

2-Jet, 1-Tag bin. The procedure is far from being straightforward and attempts to define different W + heavy flavor enriched samples revealed to be not satisfactory (in particular for W + b component). In the end a reasonable way out was to use a strategy which allows for W + X global contribution estimation, not separating light from heavy flavor contribution: from Fig. 6.16 in the signal region, we can observe that the $M_{bl\nu}$ variable has a big discriminating power between the signal and W backgrounds. Therefore performing a cut on $M_{bl\nu}$ we are able to separate a signal enriched region from a W (and $t\bar{t}$) enriched region. It has been chosen $130 < M_{bl\nu} < 220$ to define the Signal Region (SR), and the off peak region $M_{bl\nu} < 130$ or $M_{bl\nu} > 220$ as Sideband Region (SB). It worth saying that we take the Sideband Region from both upper and lower mass peak values to limit kinematic biases coming from the cut itself. Table 6.5 shows the yields for MC and Data in the Sideband and Signal Region.

The fit to the $\not{E}_{\mathrm{T}}$ for the data-driven estimation of QCD contamination cannot be performed in the SR and SB separately, due to poor MC statistics which introduces big uncertainties in the modeling. Instead, the fit on the whole 2-Jet 1-Tag bin is performed (shown in Fig. 6.11) using the Anti-Isolated sample to model the $\not{E}_{\mathrm{T}}$ distribution for QCD; then the amount of QCD in the SB and SR is determined taking the $M_{bl\nu}$ Anti-Isolated distribution, rescaling it to the fitted result in the 2-jet 1-tag bin (this is done applying the $\not{E}_{\mathrm{T}}$ cut to the fit distribution) and in the end applying the $M_{bl\nu}$ cuts. The resulting QCD yields in Signal and Sideband Region are shown in Tab. 6.5. On MC we ensured that this introduces no bias and and we assume that the acceptance on the signal is reliable from what we understood in Sec. 6.3.2.

6.3.4 Anti-Isolated Samples

We define qcd-enriched samples for both 2-Jet 1-Tag sample and control sample A using anti-isolation and anti-ID requirements. The tight lepton definition is the same as 6.2.2, except for the relative isolation and electron ID requirements. The electron is

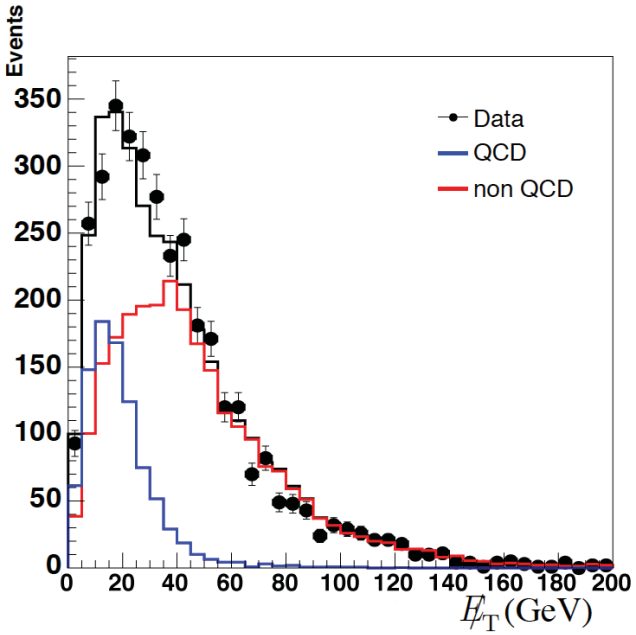

Figure 6.11: $\not{E}_T$ fit for QCD estimation in the 2-Jet 1-Tag (signal) sample.

required explicitly not to pass two out of three between:

- The 70% efficiency working point. See [63];
- the photon-conversion veto [63] requirements;
- $I_{\text{rel}}^{\text{PF}} < 0.1$.

We require exactly one tight lepton and drop any second lepton veto. The jet and b-tagging requirements are the same as they were defined for the signal sample in 6.2.2, and the control sample A in 6.3.1.

6.4 Data driven backgrounds estimation

6.4.1 Multi-jet QCD

Monte Carlo estimations of the QCD contamination have to be considered particularly unreliable for the purposes of this analysis as it was for 2010 analysis, because only extreme kinematical regions pass the selection, and tail effects are the most difficult to simulate properly. These arguments lead to the conclusion that only *in situ* data-driven estimations will give the needed confidence on the amount of this background.

For this purpose, a template fit to the $\not{E}_T$ distribution is performed, after all other cuts have been applied, with the following fit function:

$$F(\not{E}_T) = N_{sig} \cdot S(\not{E}_T) + N_{qcd} \cdot B(\not{E}_T) \,, \tag{6.8}$$

where $S(\not{E}_T)$ and $B(\not{E}_T)$ are the assumed templates for signal-like processes according

to Monte Carlo predictions, and QCD events (extracted form the Anti-Isolated sample on data, see 6.3.4) respectively, letting only $N_{sig-like}$ and N_{qcd} fluctuate in the fit. So the number of QCD events in the signal region, N_{qcd}^{SR}, is obtained by integrating the function $B(\not\!\!E_{\mathrm{T}})$ normalized to the fitted QCD events, for $\not\!\!E_{\mathrm{T}} > 35$ GeV: $N_{qcd} \cdot \int_{35}^{\infty} B(\not\!\!E_{\mathrm{T}}) d\not\!\!E_{\mathrm{T}}$. Such fit is performed both in 2-jet 1-tag Sample and in Control Sample A (details in the corresponding sections 6.3.1 and 6.3.3).

Figure 6.12 shows that the $\not\!\!E_{\mathrm{T}}$ distribution for QCD is not dramatically affected by isolation requirements. The systematics uncertainty due to this approximation is conservatively estimated to be 50%. Since we want to take the shape of the QCD discriminating variables from data, we compare the distributions of η_{lj} and $M_{bl\nu}$ in the isolated and anti-isolated samples to check that no significant bias is introduced in the final signal yield extraction (Fig. 6.13). In order to get more MC statistics, the b-requirements were dropped (having checked this doesn't introduce biases) and the presence of 1 jet of $p_T > 30$ GeV and at least 1 other jet with $p_T > 20$ GeV was required.

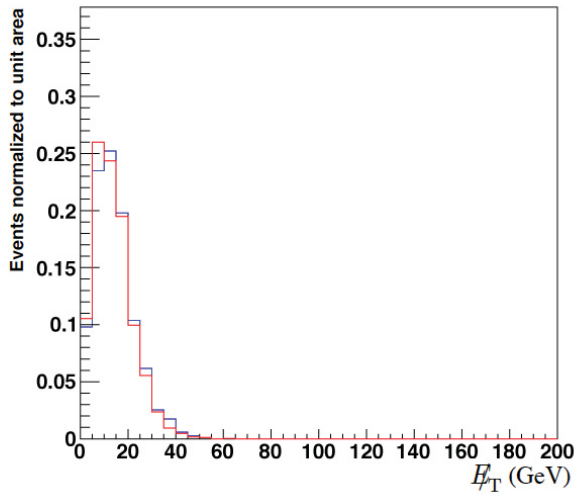

Figure 6.12: $\not\!\!E_{\mathrm{T}}$ distributions for Monte Carlo QCD samples obtained after anti isolation and ID cut for the electron (red line) and after the standard isolation cut (blue line).

6.4.2 W/Z + X extraction strategy

In this section we describe the extrapolation procedure to reliably model the $M_{bl\nu}$ and η_{lj} distributions for W components of the background. Section 6.3.3 define a W + heavy flavor enriched region, where the signal contamination is small. Plots 6.10 and sections 6.3.1, 6.3.2 allow us to understand the behavior of $W+$ light and $t\bar{t}$ components of the background. For W + heavy flavor a scale factor and data-driven shape for the modeling of η_{lj} are extracted from the sideband region SB to the signal region SR, taking the yields for $t\bar{t}$, single top tW, s-channels, and VV processes from the Monte Carlo simulation. In detail the procedure is the following:

Step 1: W/Z+X in the Sideband Region First we estimate scale factor and the η_{lj} shape

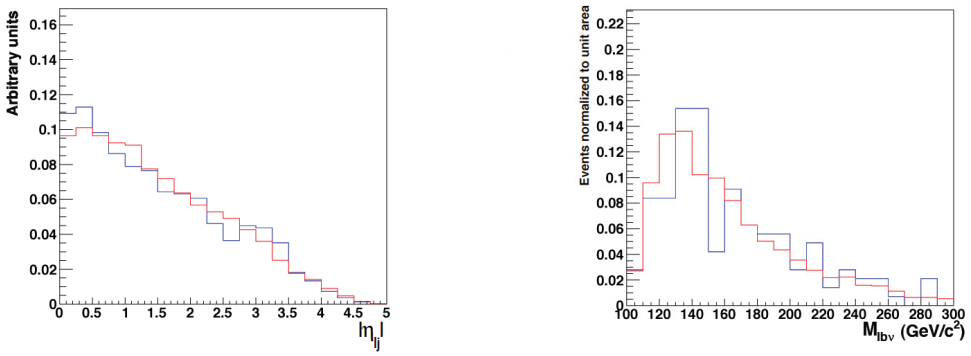

(a) (b)

Figure 6.13: η_{lj} (a) and $M_{bl\nu}$ (b) distributions for Monte Carlo QCD samples obtained after an anti isolation and ID cut (red) and after the standard isolation cut (blue).

for W/Z+X. We take the data η_{lj} in the SB and subtract the data-driven QCD shape, the Standard Model $t\bar{t}$, single top tW-, s-, t-channel, and VV. What remains is taken as the data-driven W/Z+X η_{lj}, with the scale factor evaluated as the ratio between the obtained template and the W/Z + X simulated in Monte Carlo.

Step 2: W/Z+X extrapolation in the Signal Region Then we apply the scale factor from the sideband to the signal region and use the η_{lj} shape previously determined. This will be used in the fit described later on in section 6.5.2

Figure 6.14(a) shows the comparison of η_{lj} shapes for the W/Z+X in the Signal Region and Sideband on Monte Carlo. After the extraction has been performed, a conservative estimate of the uncertainty $\pm 100\%$ for the t-channel cross section and of $\pm 20\%$ for $t\bar{t}$ yield is considered to take into account the effect of the ansatz made on the signal yield (the contamination of signal in sideband region). Figure 6.14 (b) shows the effect of these variations on the extracted shape of W/Z+X. Table 6.6 shows the results of Kolmogorov tests on distributions for the overall W/Z + X in Signal and Sideband Regions.

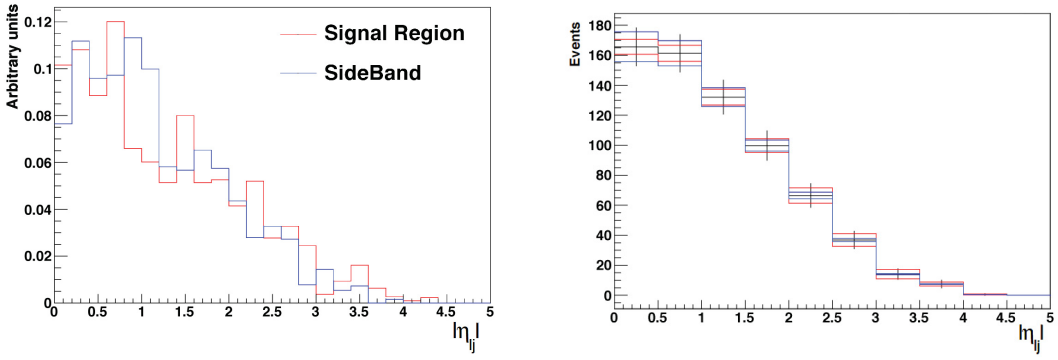

(a) (b)

Figure 6.14: (a) Shape comparison of η_{lj} variable for the W/Z + X in the Signal Region vs Sideband region. (b) Effect of varying the t-channel yield (red line) by $\pm$ 100% and $t\bar{t}$ yield (blue line) by $\pm$ 10% in the Sideband Region on the data-driven extracted shape (black line).

Process/Observable	KS(shape only) η_{lj} comparison in the SR/SB
η_{lj}	0.95
$M_{bl\nu}$	0.67
$\cos\theta^*_{lj}$	0.72

Table 6.6: KS probability for η_{lj} distributions for the overall W/Z + X, between Signal and Sideband Region

It is worth noticing that the extracted shape depends on the statistics of the sample. To take this into account, we perform pseudo-experiments where the subtraction procedure is repeated on simulated datasets. Such datasets are obtained summing η_{lj} Monte Carlo distributions for all the channels assuming the standard model yields except for $W+$heavy flavor, which is scaled by a factor 2 to get a realistic scenario. To check the compatibility of η_{lj} between the Signal and Sideband Regions we compare data-driven $W/Z+$X η_{lj} distribution with the one from Monte Carlo simulation, for each pseudo-experiment. Such results show so far that this procedure is consistent. Nevertheless the quantitative effect on the final result has to be evaluated. It turns out the statistical fluctuations in the Sideband affect the final extraction procedure, resulting in additional systematics uncertainty to be accounted for. This is discussed in the detail in section 6.6.

6.4.3 Backgrounds summary

This section sums up the results of data-driven procedures for the QCD and main backgrounds estimation. The QCD yield is obtained performing the fit described in section 6.4.1 in the signal sample. W/Z + X shape for η_{lj} is derived from data-driven procedures in the way is described in Sec. 6.4.2, while the QCD shape is taken from the Anti-isolated sample described in 6.3.4.

The uncertainty on the data-driven shapes, for the procedure adopted, is destined to decrease with the increasing statistics. Furthermore, the shape effects due to statistical fluctuations are mitigated by the subtraction procedure, since we constrain the total yield contribution of W/Z + X, and so, for example, an over-fluctuation in W + light component is compensated by an under-fluctuation in W + heavy flavor.

Table 6.7 shows the summary of the event yields in the 2-Jet 1-Tag bin before the $M_{bl\nu}$ cut.

Process	entries
t-channel	198.8
tW-channel	93.4
s-channel	16.5
$t\bar{t}$	522.0
$W+$ light partons	70.0
$Z+$ jets	14.9
Wc	179.0
Wb	263.4
QCD	76.1
Total	1434.1
Data	1606

Table 6.7: Event yields summary including data-driven estimations and b-tagging scale factors for simulation and data. Background uncertainties (QCD, W/Z+light, W/Z+heavy flavours) are discussed in Sec. 6.6.

6.5 Signal properties and cross section measurement

6.5.1 Top quark reconstruction and signal properties

Referring to Sec. 5.4.1 for details about variables definition and top quark hypothesis reconstruction, in Fig. 6.15 and 6.16 $\cos\theta^*_{lj}$, η_{lj} and $M_{bl\nu}$ for data and MC in the 2-Jet 1-Tag bin are shown.

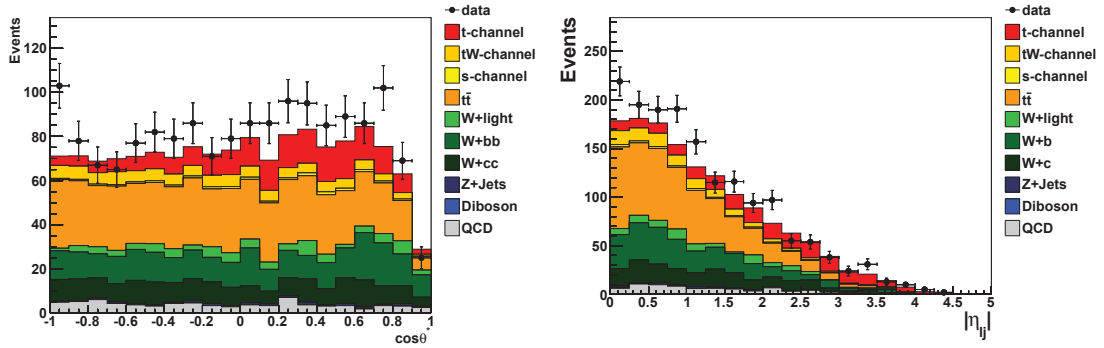

(a) (b)

Figure 6.15: Cosine of the angle between charged lepton and untagged jet ($\cos\theta^*_{lj}$), in the reconstructed top rest frame after the full event selection (a) and pseudorapidity of the untagged jet (η_{lj}) after the full event selection.

6.5.2 Signal extraction and cross section measurement

A likelihood fit is performed to η_{lj} distribution only, to determine the signal cross section. Differently from the 2010 analysis fit procedure, now the free parameters are the signal yield, the electroweak background yield (W/Z + X, Diboson), and the top

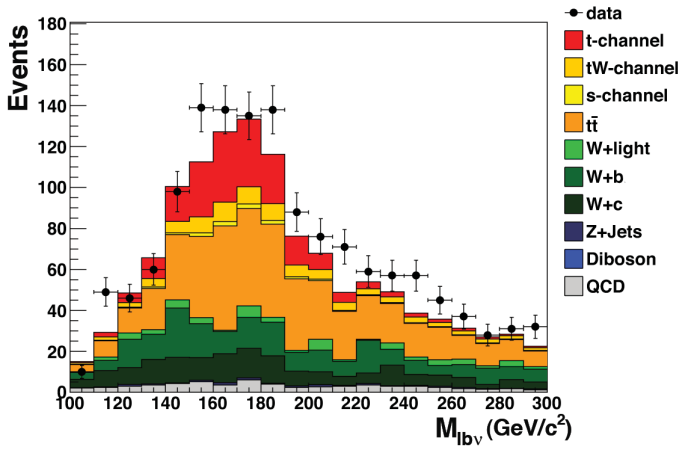

Figure 6.16: Reconstructed top quark mass after the full selection.

background yield ($t\bar{t}$, tW, and s single top channels), while the QCD is constrained to the value obtained from the fit and the uncertainty on QCD is considered in systematics. The idea behind this choice is to be maximally robust against background uncertainties, getting rid of the difference in shape while grouping together the channels, and at the same time exploiting the fact that electroweak backgrounds (W/Z + X) scale together, so that relative uncertainties on their shape only affect the shape of the overall electroweak background.

We define the unbinned likelihood function given by:

$$L(\eta_1, ..., \eta_n | N_s, N_b) = e^{-(N_s + N_{ewk} + N_{top} + N_{qcd})} \cdot \cdot \prod_{k=1}^{n} \left(N_s \cdot P_s(\eta_k) + N_{ewk} \cdot P_{ewk}(\eta_k) + N_{top} \cdot P_{top}(\eta_k) + N_{qcd} \cdot P_{qcd}(\eta_k) \right) \tag{6.9}$$

where N_s, N_{ewk}, N_{top}, N_{qcd} are the signal and backgrounds yields, n is the number of observed events, and P_s, $P_{b=(ewk,top,qcd)}$ are the signal and background distribution functions. The extended maximum likelihood fit gives us the best estimation of N_s and $N_{b=ewk,top,qcd}$, with the model distributions considered fixed and taken from Monte Carlo or data-driven templates.

It is convenient to define the signal strength S_{signal}, ewk strength S_{ewk} and top strength S_{top} as the ratio

$$S_{i=signal,ewk,top} = N_{measured,i} / N_{expectation,i} \tag{6.10}$$

Whenever the fit results will be expressed in terms of S_i, they will refer to Table 6.7 for $N_{expectation,i}$. The fit results are shown in Fig. 6.17 and the estimated yields are:

$$S_{signal} = 0.85 \pm 0.19 \quad S_{ewk} = 0.93 \pm 0.30 \quad S_{top} = 1.06 \pm 0.10$$

Which in terms of number of events becomes for the signal:

$$N_{signal} = 174 \pm 63$$

The estimation of the data-driven systematics effect for the W/Z + X component extrac-

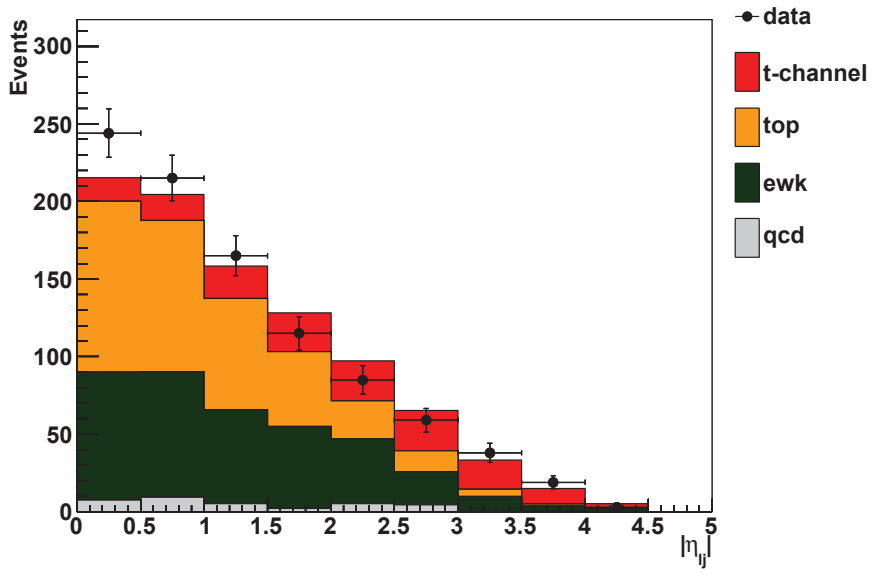

Figure 6.17: $|\eta_{lj}|$ fit results. The different contributions are rescaled by a factor equal to the strengths obtained from the fit.

tion which has been discussed in detail in Sec. 6.4.2, will be considered in Sec. 6.6.

The single top cross section is related to the signal yield by the formula:

$$\sigma = \frac{N_s}{\epsilon \cdot B(t \to \ell\nu b) \cdot L} \tag{6.11}$$

where ϵ is the efficiency estimated from Monte Carlo (ϵ = 0.35 %), $B(t \to \ell\nu b) = 0.1080$ [76], and the luminosity, L, is equal to 920.7 pb^{-1}. Table 6.8 summarizes the results of the likelihood fit to η_{lj} distributions including the cross section measurement.

N_s	σ (pb)
174 ± 63	55.1 ± 12.5

Table 6.8: Fit results: number of fitted signal events and corresponding cross section.

6.6 Results with the inclusion of systematic uncertainties

This section considers the sensitivity of the analysis to systematic uncertainties of instrumental or physics origin.

6.6.1 Systematic uncertainties

The systematic uncertainties whose impact on the analysis have been evaluated are: background normalization and modeling, jet energy scale (JES), jet energy resolution (JER) and $\not\!\!E_{\mathrm{T}}$ scale uncertainty, b-tagging and mistagging uncertainties, signal modeling, pile up, fit procedure systematics, and in the end the luminosity uncertainty.

Backgrounds normalization and modeling

Although this analysis makes no assumption on the overall background rate, a variation in the relative rates of different background processes can affect the shape of or the background yields in the fit procedure. We consider:

- $t\bar{t}$: $\pm 18\%$, motivated by the quadratic sum of all the statistical and systematic uncertainties of Ref. [67], but this choice is conservative as the main systematic uncertainties of that measurement are shared by the present analysis;
- QCD: a variation is taken conservatively as $\pm 50\%$;
- $W, Z+$ light partons and heavy flavours: we use the RMS of the pseudo-experiment distribution for the data-driven extraction procedure (see later).

Jet Energy Scale (JES) and $\not\!\!E_{\mathrm{T}}$ scale uncertainty

To take into account the JES and jet energy resolution (JER) variations, it should be applied first the nominal JER smearing and then the JES uncertainty shift to the jets. At the moment of writing this theses, the impact of JER on the fitted signal strength was not yet evaluated, nonetheless we know from estimations in the muon decay channel of the top, that this effect is far less the JES uncertainty. In detail we vary simultaneously all jet four momenta by either +1σ or -1σ of the η and p_T-dependent uncertainties [97]. The official CMS Jet Energy Corrections are taken from DataBase and include a new 10% for jets with $|\eta| > 3$ due to unexpectedly large HCAL response in the forward region. This is an important point since in that region the signal to background ratio is most favorable, and so it reflects clearly in this analysis. For each variation in jet energy scale, the missing transverse energy is recalculated accordingly.

As in 2010 analysis, to this correction the "unclustered energy" systematics is added, and a shift of $\pm 10\%$ is applied to $\vec{\not\!\!E}_{\mathrm{T}}$ (leptons and jets are added back to the unclustered energy).

b-tagging and mistagging uncertainties

We variate the scale factors of Sec. 6.3.3 by their data-driven uncertainties [95], propagating these variations to the formulas 6.2 and 6.3.

Modeling uncertainties

The following signal modeling effects have been taken into account :

- Q^2: for t-channel and $t\bar{t}$, using specific simulated samples with $Q^2 = 2$ and $Q^2 = 0.5$ the nominal value.
- ISR/FSR: for t-channel and $t\bar{t}$, using specific Monte Carlo samples.
- $fragmentation$: for $t\bar{t}$, using different fragmentation models.

Pile up

The effect of pile up events has been evaluated by re-weighting the MC samples such that the number of simulated pile up events matches the number of pile up events observed on average in data. We apply a systematic uncertainty arising from the uncertainties from this pile up re-weighting procedure. Therefore, all the simulated events gain additional weight factors which correspond to variation of the average number of pile up events by ± 1.

W branching ratio

The uncertainty on the W branching ratio into leptons, and thus of $t \to \ell\nu b$ (with $\ell = e, \mu, \tau$), is taken as $\pm 0.8\%$ [76]. This uncertainty is propagated directly to the formula 6.11.

Luminosity uncertainty

The luminosity determined from dedicated measurements [98] is known within a 5% uncertainty. This uncertainty is propagated directly to the formula 6.11.

Effect on signal extraction

The distributions η_{lj} for each channel is affected by rate and shape uncertainties due to systematics. The shape of the overall background distribution is affected by the relative normalization of background events. η_{lj} is quite stable under variations of JES, $\not{E}_{\mathrm{T}}$, b tagging, mistagging, while for instance $M_{bl\nu}$ is much more affected. We consider those uncertainties in the definition of the signal and sideband regions, as well as in the data-driven extraction procedure described in Section 6.4.2

Data driven procedure

The data driven procedure described in Sec 6.4.2 has the advantage that incorporates all W/Z rate and modeling uncertainties (Q^2, ISR/FSR, hadronization mode), but on the other hand is dependent on the statistics of the Signal Region and the Sideband Region. To evaluate this effect pseudo-experiments have been performed: using the standard model prediction for all samples except for W + heavy flavor, where a scale factor of 2 has been applied, a big number of pseudo-dataset have been built. Then, W/Z + X extraction in the Sideband and Signal Regions are repeated, and fits to the generated datasets are performed. The resulting signal strength distribution for the all pseudo-experiments is shown in Fig. 6.18. This distribution has a non-negligible RMS (in short we call it "spread") and a difference in the mean value with respect to the generation central value (in short we call it "bias").

To take into account the bias we define a simple scale factor:

$$SF_{bias} = s_{generation}/s_{meanvalue} \tag{6.12}$$

where $s_{generation}$ is 1 and $s_{mean\,value}$ is the bias. In the end, we correct the final signal strength for cross-section measurement by this SF_{bias}.

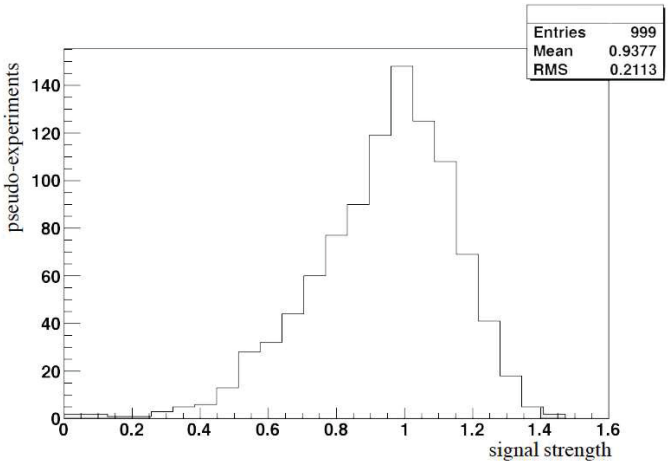

Figure 6.18: Result of the fits on one pseudo-dataset in the Signal Region, drawing random pseudo-experiments in the Sideband region.

6.6.2 Effect on signal extraction and correction

In Table 6.9, the effect of the main systematics uncertainties on the signal strenght is reported. The uncertainty from data driven procedure is intended as the RMS of the pseudo-experiments signal strength distribution of Fig. 6.18. The systematics uncertainty is evaluated dicing pseudo-experiments with the varied templates using template morphing technique with the theta software [75]. Since this procedure gives us the relative uncertainties, they are afterwards scaled to take into account the SF_{bias}.

Therefore the final result after the bias correction is:

SignalStrength: 0.85	$\pm$ 0.19 (stats)
Data driven procedure	$\pm$ 0.21(stats)
Systematics	up/down variation
$b$tagging	+0.08 -0.09
JES	+0.05 -0.08
Mistagging	-0.00024 -0.00021
Unclustered $\not{E}_{\mathrm{T}}$	-0.008 -0.0028
$t\bar{t}$ rate	-0.027 +0.027
PU	+0.031 +0.007
total systematics:	$\pm$ 0.24
total syst+stats:	$\pm$ 0.31
Corrected by SF_{bias}:	0.91 $\pm$ 0.33 (stats + syst)

Table 6.9: Effect of systematics on the signal strength measured by the fit.

$$\sigma = 58.8 \pm 13.3(stat.)\,^{+16.4}_{-16.4}(syst.)\ \text{pb} \tag{6.13}$$

6.7 Conclusions and V_{tb} measurement

In this chapter the preliminary results of the single top t-channel cross section measurement on 920.7 pb^{-1} of data collected by CMS in 2011 have been shown, considering the electronic decay channel of the W boson coming from top quark.

As in 2010 analysis the measurement in the electron channel is combined with an analogous measurement in the muon channel only [99, 100] performed on 1299.1 pb^{-1}. The procedure adopted for signal extraction is a simultaneous maximum likelihood fit on η_{lj} variable, fitting together all parameters but the electroweak component which remains separated for the two channels. It is reasonable since we don't want to make the assumption that this component behaves in the same way for electrons and muons (or, at least, we want to check that it effectively happens, and in the end the results are consistent with the assumption).

We obtain the following cross section measurements:

$$\begin{aligned}
\sigma &= 70.9 \pm 6.8(stat.)\,^{+10.6}_{-10.6}(syst.) \pm 3.7(lumi.)\ \text{pb} && \text{muon channel} \\
\sigma &= 58.8 \pm 13.3(stat.)\,^{+16.4}_{-16.4}(syst.) \pm 2.8(lumi.)\ \text{pb} && \text{electron channel} \\
\sigma &= 69.5 \pm 6.0(stat.)\,^{+9.9}_{-9.9}(syst.) \pm 3.7(lumi.)\ \text{pb} && \text{combined}
\end{aligned} \tag{6.14}$$

The combined measurement, for which all systematic uncertainties have been considered as fully correlated between the electron and the muon decay channels, is consistent with the standard model expectation. The higher amount of data analyzed in 2011 with respect to the 36.1 pb^{-1} of 2010 allowed us to reduce the statistic uncertainty, entering the systematic dominated regime. Moreover, the systematics have been reduced as well through

accurate choices of data-driven procedures (for example, not separating the individual W + jets contributions, but estimating the overall shapes and scale factors) and at selection level (for example, the aforementioned removal of the b-veto requirement). From systematic uncertainties point of view, one of the main advantages of adopting the data-driven W/Z + X estimation is that the uncertainty associated to it depends on the statistics of the samples involved, and so improve with increasing available data. Nevertheless, since the main contribution to the overall uncertainties comes from this data-driven estimation, in the next future more precise cross section measurement will also require improvements and further studies on optimization of such data-driven procedures.

In conclusion a measurement of the CKM element V_{tb} is also given. Under the assumption that $|V_{td}|$ and $|V_{ts}|$ are much smaller than $|V_{tb}|$ and without assuming Standard Model V-A coupling strength, we can measure $|V_{tb}|$ as $|V_{tb}| = \sqrt{\frac{\sigma^{exp}}{\sigma^{th}}}$. Given the next-to-next-to-leading order (NNLO) predicted cross section $\sigma^{th} = 64.57^{+2.09}_{-0.71}\,(\text{scale})^{+1.51}_{-1.74}\,(\text{PDF})$ pb (for a top mass of $m_t = 172.5$ GeV/c^2) and the combined measured cross section in equation 6.14, we find:

$$|V_{tb}| = 1.04 \pm 0.09\,(exp)\ \pm 0.02\,(th). \tag{6.15}$$

This result is in agreement with the Tevatron, combined from CDF and D0, V_{tb} measurement, $|V_{tb}| = 0.88 \pm 0.07$. Furthermore, with only 1/5 of the data collected by CMS in 2011, this measurement reaches a precision already comparable with Tevatron's. So, in the next months and through all the 2012 we will be able to investigate the CKM unitarity with an unprecedented precision in the top quark sector.

Conclusions

This thesis has presented a data analysis work performed in the context of the CMS experiment and aimed at measuring the cross section of single top produced in t-channel and decaying through $t \to Wb \to e\nu b$. The main analysis is based on data collected by CMS in 2010, corresponding to an integrated luminosity of 36.1 pb^{-1}, with an update using 920.7 pb^{-1} of 2011 data taking. The topology of the process and the spin correlations between the particles involved allow to perform a very tight selection. Furthermore, data-driven techniques have been set up for a reliable estimation of the main backgrounds (QCD multi-jet and W + jets) to the signal of interest. Different sources of systematic uncertainties have been taken into account, both of instrumental and physics origin, among which the b-tagging uncertainty, the QCD data-driven uncertainty and the signal and background modeling.

At the end the signal extraction is obtained from a template fit to the most discriminating variables and the single top t-channel cross section measured with the inclusion of systematics in the electronic channel is

$$\sigma = 154 \pm 56(stat.)\,^{+40}_{-46}(syst.) \pm 17(lumi.)\ \text{pb}$$

for 2010 analysis, and

$$\sigma = 58.8 \pm 13.3(stat.)\,^{+16.4}_{-16.4}(syst.) \pm 2.8(lumi.)\ \text{pb}$$

for 2011 analysis. Both results are consistent with latest NNLO Standard Model prediction $\sigma^{th} = 64.57^{+2.09}_{-0.71}\,(\text{scale})^{+1.51}_{-1.74}\,(\text{PDF})$ pb and we can conclude that the signal excess measured in 2010 was merely due to statistical fluctuations.

Both the results have been combined with the ones obtained in the muonic decay channel of the W stemming from the top quark. For the 2010 analysis a further combination has been performed with a multivariate analysis measuring as well the t-channel cross section (BDT). Then, the combined measurements are used to evaluate the V_{tb} element of the CKM matrix using the relation $|V_{tb}| = \sqrt{\frac{\sigma^{exp}}{\sigma^{th}}}$. The results are summarized in Tab. 6.10.

In the future, the analyses presented here, together with achieving more and more

precise and refined single top cross section determinations, can constitute the baseline for further challenging studies in single top production and decay sector.

Excess of events in the t-channel, for example, could suggest the existence of FCNC (flavor changing neutral currents, $u \to t$) which can be investigated checking top polarization and differential cross sections (as $\mathrm{d}\sigma/\mathrm{dy}$); or maybe could be related to large $|V_{tb}|$ and so to the non unitarity of the CKM matrix. On the contrary, a deficit in t-channel cross section can be a hint of the existence of a 4^{th} quark generation, which leads $|V_{tb}|$ to be < 1.

In conclusion, as in many other physics areas explored, after the Standard Model precision tests, with increasing statistics the LHC is expected to eventually enlighten some of the basic questions historically remained open in the elementary particle physics.

Dataset, integrated luminosity (pb^{-1})	σ_{t-ch} (pb)	$\lvert V_{tb}\rvert$
2010, 36.1	$83.6 \pm 29.8(stat. + syst.) \pm 3.3(lumi.)$	$1.16 \pm 0.22(exp.) \pm 0.02(th.)$
2011, 920.7 (electrons) and 1299.1 (muons)	$69.5 \pm 11.6(stat. + syst.) \pm 3.7(lumi.)$	$1.04 \pm 0.09\,(exp) \pm 0.02\,(th)$

Table 6.10: Summary of the single top t-channel cross sections and V_{tb} CKM element measurements, with 2010 and 2011 data, for muon and electron channels combined. The 2010 results take into account the combination with the multivariate analysis described in detail in [87].

Acknowledgments

I am grateful to Prof. Crisostomo Sciacca for giving me the opportunity to work in the CMS experiment at the LHC, and for his guidance since I was undergraduated student.

I also want to thank the “single top” group conveners Prof. Andrea Giammanco and Prof. Jeannine Wagner-Kuhr, and Prof. Luca Lista for the deep, enlighting and full of advice discussions we had throughout these three years of work.

My gratitude also goes to Prof. Marco Napolitano and Prof. Benedetto D’Ettorre who followed and revised my thesis work with their expert insight.

Bibliography

[1] S.L. Glashow, Nucl. Phys. **22** (1961) 579;
S. Weinberg, Phys. Rev. Lett. **19** (1967) 1264;
A. Salam, in *Elementary Particle Theory* , ed. N. Svartholm,
Almqvist and Wiksells, Stockholm (1969) p. 367 .

[2] M. Gell-Mann, Phys. Lett. **8** (1964) 214;
G. Zweig, CERN-Report 8182/TH401 (1964);
H. Fritzsch, M. Gell-Mann and H. Leutwyler, Phys. Lett. B **47** (1973) 365;
D. Gross and F. Wilczek, Phys. Rev. Lett. **30** (1973) 1343;
H.D. Politzer, Phys. Rev. Lett. **30** (1973) 1346;
G. 't Hooft, *Marseille Conference on Yang–Mills fields* (1972).

[3] P.A.M. Dirac, Proc. Roy. Soc. Lond. **A114** (1927) 243;
P. Jordan and W. Pauli, Z. Phys. **47** (1928) 151;
W. Heisenberg and W. Pauli, Z. Phys. **56** (1929) 1;
J. Schwinger, Phys. Rev. **73** (1948) 416;
R. Feynman, Phys. Rev. **76** (1949) 749.

[4] E. Fermi, Nuo. Cim. **11** (1934) 1; *ibid.* Z. Phys. **88** (1934) 161;
R. Feynman and M. Gell-Mann, Phys. Rev. **109** (1958) 193.

[5] O. S. Bruning *et al.* (eds.), *The LHC design report v1: the LHC Main Ring*, CERN-2004-003-V-1, http://cdsweb.cern.ch/record/782076;
The LHC design report v2: the LHC Infrastructure and General Services, CERN-2004-003-V-2, http://cdsweb.cern.ch/record/815187;
M. Benedikt *et al.* (eds.), *The LHC design report v2: the LHC Injector Chain*, CERN-2004-003-V-3, http://cdsweb.cern.ch/record/823808;
L. Evans and P. Bryant (eds.), JINST **3** (2008) S08001.

[6] ATLAS Collaboration, *ATLAS: technical proposal for a general-purpose pp experiment at the Large Hadron Collider at CERN*, CERN-LHCC-94-43,
http://cdsweb.cern.ch/record/290968.

[7] CMS Collaboration, *CMS technical proposal*, CERN-LHCC-94-38,
http://cdsweb.cern.ch/record/290969.

[8] LHCb Collaboration, *LHCb technical proposal*, CERN-LHCC-98-004,
http://cdsweb.cern.ch/record/290969.

[9] TOTEM Collaboration, *TOTEM, Total cross section, elastic scattering and diffractive dissociation at the LHC: Technical Proposal*, CERN-LHCC-99-007, http://cdsweb.cern.ch/record/385483.

[10] ALICE Collaboration, *ALICE: Technical proposal for a Large Ion collider Experiment at the CERN LHC*, CERN-LHCC-95-71, http://cdsweb.cern.ch/record/293391.

[11] A.A. Annenkov, M.V. Korzhik and P. Lecoq, Nucl. Instr. Meth. **A 490** (2001) 30.

[12] R.Y. Zhu, Nucl. Instr. Meth. **A 413** (1998) 297.

[13] V. Khachatryan *et al.* [CMS Collaboration], JHEP **1009** (2010) 091.

[14] P. Levai, G. Papp *et al.*, Nucl. Phys. **A 698** (2002) 631.

[15] R. Aaij *et al.* [LHCb Collaboration], Phys. Lett. B **699** (2011) 330.

[16] S. Chatrchyan *et al.* [CMS Collaboration], Phys. Rev. Lett. **107** (2011) 191802.

[17] G. Aad *et al.* [ATLAS Collaboration], JHEP **12** (2010) 060;
V. Khachatryan *et al.* [CMS Collaboration], JHEP **01** (2011) 080.

[18] V. Khachatryan *et al.* [CMS Collaboration], JHEP **04** (2011) 050;
V. Khachatryan *et al.* [CMS Collaboration], Phys. Rev. Lett. **107** (2011) 021802.

[19] V. Khachatryan *et al.* [CMS Collaboration], Phys. Lett. B **699** (2011) 196;
V. Khachatryan *et al.* [CMS Collaboration], Phys. Rev. Lett. **106** (2011) 231801.

[20] A. H. Chamseddine, R. Arnowitt and P. Nath, Phys. Rev. Lett. **49** (1982) 970.

[21] G. Kane *et al.*, Phys. Rev. **D49** (1994) 6173.

[22] V. Khachatryan *et al.* [CMS Collaboration], Phys. Lett. B **698** (2011) 196;
G. Aad *et al.* [ATLAS Collaboration], Phys. Lett. B **701** (2011) 186.

[23] G. Altarelli, B. Mele and M. Ruiz-Altaba, *Z. Phys.* **C45** (1989) 109.

[24] V. Khachatryan *et al.* [CMS Collaboration], Phys. Rev. Lett. **106** (2011) 201804.

[25] V. Khachatryan *et al.* [CMS Collaboration], arXiv:1103.0030v1 .

[26] V. Khachatryan *et al.* [CMS Collaboration], JHEP **05** (2011) 093.

[27] K. Agashe, A. Belyaev, T. Krupovnickas *et al.*, Phys. Rev. **D77** (2008) 015003.

[28] P. Meade and L. Randall, JHEP **05** (2008) 003.

[29] V. Khachatryan *et al.* [CMS Collaboration], Phys. Lett. B **697** (2011) 434.

[30] X. Wang and M. Gyulassy, Phys. Rev. **D44** (1991) 3501.

[31] G. Aad *et al.* [ATLAS Collaboration], Phys. Rev. Lett. **105** (2011) 252303.

[32] S. Chatrchyan *et al.* [CMS Collaboration], Phys. Rev. **C84** (2011) 024906.

[33] G. Aad *et al.* [ATLAS Collaboration], Phys. Lett. B **697** (2011) 294.

[34] J. J. Cao, G. Eilam, M. Frank, K. Hikasa, G. L. Liu, I. Turan and J. M. Yang, Phys. Rev. **D75** (2007) 075021.

[35] M. Perelstein, M. E. Peskin and A. Pierce, Phys. Rev. **D69** (2004) 075002.

[36] K. Nakamura *et al.* (Particle Data Group), J. Phys. **G37** (2010) 075021 and 2011 partial update for the 2012 edition available at http://pdg.lbl.gov/;
J. Charles *et al.* (CKMfitter Group), Eur. Phys. Jour. C **41** (2005) 1 [hep-ph/0406184], updated results and plots available at: http://ckmfitter.in2p3.fr;
Tevatron Electroweak Working Group [CDF, D0 Collaborations], arXiv:1107.5255v3.

[37] The Coordinated Theroetical-Experimental Project on QCD [CTEQ], http://www.phys.psu.edu/ cteq/.

[38] N. Kidonakis, arXiv:0909.0037v1.

[39] N. Kidonakis, Phys. Rev. **D81** (2010) 054028.

[40] N. Kidonakis, Phys. Rev. **D82** (2010) 054018;
ibid. Phys. Rev. **D83** (2011) 091503(R).

[41] G. S. Abrams *et al.* [MARK II Collaboration], Phys. Rev. Lett. **63** (1989) 2447.

[42] D. Decamp *et al.* [ALEPH Collaboration], Phys. Rev. **B236** (1990) 511;
P. Abreu *et al.* [DELPHI Collaboration], Phys. Rev. **B242** (1990) 536;
M. Z. Akrawy *et al.* [OPAL Collaboration], Phys. Rev. **B236** (1990) 364.

[43] T. Åkesson *et al.* [UA2 Collaboration], *Z. Phys.* **C46** (1990) 179.

[44] F. Abe *et al.* [CDF Collaboration], Phys. Rev. Lett. **68** (1992) 447;
F. Abe *et al.* [CDF Collaboration], Phys. Rev. **D45** (1992) 3921.

[45] F. Abe *et al.* [CDF Collaboration], Phys. Rev. Lett. **74** (1995) 2626;
S. Abachi *et al.* [D0 Collaboration], Phys. Rev. Lett. **74** (1995) 2632.

[46] D0's Top Quark Physics Results,
http://www.d0.fnal.gov/Run2Physics/top/top_public_web_pages/top_public.html

[47] CDF Collaboration, CDF-NOTE-10549 (2011);
D0 Collaboration, D0-NOTE-6222 (2011);
arXiv:1107.5255v3.

[48] ATLAS Collaboration, *ATLAS Conference Note* ATLAS-CONF-2011-054 (2011);
CMS Collaboration, *CMS Physics Analysis Summary* CMS PAS TOP-11-008 (2011).

[49] ATLAS Collaboration, *ATLAS Conference Note* ATLAS-CONF-2011-108 (2011); CMS Collaboration, *CMS Physics Analysis Summary* CMS PAS TOP-11-024 (2011).

[50] CMS Collaboration, *CMS Physics Analysis Summary* CMS PAS TOP-11-019 (2011).

[51] T. Altonen *et al.* [CDF Collaboration], Phys. Rev. Lett. **103** (2009) 092002.

[52] S. Chatrchyan *et al.* [CMS Collaboration], Phys. Rev. Lett. **107** (2011) 091802.

[53] V. M. Abazov *et al.* [D0 Collaboration], Phys. Lett. B **705** (2011) 313.

[54] T. Aaltonen *et al.* [CDF Collaboration], Phys. Rev. **D82** (2010) 112005.

[55] ATLAS Collaboration, *ATLAS Conference Note* ATLAS-CONF-2011-088 (2011).

[56] CMS Collaboration, *CMS Physics Analysis Summary* CMS PAS TOP-11-022 (2011).

[57] CMS Collaboration, *CMS Report* CMS-DP-11-002 (2011).

[58] J. Alwall *et al.*, Eur. Phys. Jour. **C53** (2008) 473.

[59] A. Deisher *et al.*, "Simultaneous Heavy Flavor and Top (SHyFT) Cross Section Measurement: Description of Analysis Methodology", *CMS Analysis Note* **2009/179** (2011).

[60] F. Blekman, T. Chwalek, J. Gruschke and M. Renz, "Selection of $t\bar{t}$ Candidates in the Lepton+Jets Channel", *CMS Analysis Note* **2010/297** (2010).

[61] J. P. Chou, S. Eno, S. Kunori, S. Sharma and J. Wang, "Anomalous HB/HE Noise at Startup: Characteristics and Rejection Algorithms", *CMS Internal Note* **2010/006** (2010).

[62] J. Slaunwhite *et al.*, "Top Lepton Plus Jets: Electron and Muon Efficiency Measurements for 2010 Dataset", *CMS Analysis Note* **2010/362** (2010).

[63] https://twiki.cern.ch/twiki/bin/view/CMS/SimpleCutBasedEleID; https://twiki.cern.ch/twiki/bin/view/CMS/ConversionBackgroundRejection.

[64] M. Cacciari, G. P. Salam and G. Soyez, JHEP **04** (2008) 063.

[65] CMS Collaboration, *CMS Physics Analysis Summary* PAS PFT-09-001 (2009).

[66] CMS Collaboration, *CMS Physics Analysis Summary* PAS JME-10-010 (2010).

[67] CMS Collaboration, *CMS Physics Analysis Summary* PAS TOP-10-003 (2010).

[68] R. Gavin, Y. Li, F. Petriello, and S. Quackenbush, *Comput. Phys. Commun.* **182** (2011) 2388.

[69] J. Campbell and F. Tramontano, Nucl. Phys. B **726** (2005) 109.

[70] V. Abramov *et al.*, "Selection of Single Top Events with the CMS Detector at LHC", *CMS Analysis Note* **2006/084** (2006).

[71] G. Mahlon and S. Parke, Phys. Rev. **D55** (1997) 7249.

[72] G. Mahlon and S. Parke, Phys. Lett. B **476** (2000) 323.

[73] P. Motylinski, Phys. Rev. **D80** (2009) 074015.

[74] A. Giammanco, J. Bauer, Th. Mueller, J. Wagner-Kuhr and D. Konstantinov, "Prospects for the measurement of the single-top t-channel cross section in the muon channel with 200 pb^{-1} of CMS data at 10 TeV", *CMS Analysis Note* **2009/069** (2009).

[75] Th. Müller, J. Ott and J. Wagner-Kuhr, "Theta - a framework for template based modelling and inference", *CMS Internal Note* **CMS-IN 2010/017** (2010). See also http://www-ekp.physik.uni-karlsruhe.de/ ott/theta/html/index.html.

[76] K. Nakamura *et al.* (Particle Data Group), J. Phys. **G37** (2010) 075021 and 2011 partial update for the 2012 edition available at http://pdg.lbl.gov/.

[77] R. Field, "Early LHC Underlying Event Data - Findings and Surprises" arXiv:1010.3558 (2010).

[78] CMS Collaboration, *CMS Physics Analysis Summary* PAS TOP-10-002 (2010).

[79] CMS Collaboration, *CMS Physics Analysis Summary* PAS TOP-09-005 (2009).

[80] CMS Collaboration, *CMS Physics Analysis Summary* PAS BTV-10-001 (2010).

[81] E. Boos *et al.*, Phys. Atom. Nucl. 69 **8** (2006) 1317.

[82] CMS Collaboration, *CMS Physics Analysis Summary* PAS EWK-10-004 (2010).

[83] R. Barlow, http://www.slac.stanford.edu/ barlow/java/statistics1.html

[84] R. Barlow, "Asymmetric Systematic Errors" arXiv:0306138v1 (2003).

[85] A. Giammanco, A.O.M. Iorio, L. Lista, M. Merola *et al.*, "Measurement of the single-top t-channel cross section at sqrt(s) = 7 TeV with an angular analysis", *CMS Analysis Note* **2010/393** (2010).

[86] J.M. Campbell, F. Rikkert, F. Maltoni and F. Tramontano, JHEP **10** (2009) 042.

[87] M. Erdmann, R. Fischer, R. Hoenig, D. Klingebiel, J. Steggemann *et al.*, "Measurement of the t-Channel Single Top Quark Cross Section using Boosted Decision Trees with the CMS Experiment at 7 TeV", *CMS Analysis Note* **2010/388** (2010).

[88] L. Lyons, D. Gibaut and P. Clifford, Nucl. Instr. Meth. **270** (1988) 110.

[89] Th. Müller, J. Ott, S. Röcker *et al.*, "Combination of t-channel single top cross section measurements at 7 TeV in 2010 data", *CMS Analysis Note* **2011/090** (2011).

[90] CMS Collaboration, *CMS Physics Analysis Summary* PAS TOP-10-008 (2010).

[91] CMS Collaboration, *CMS Physics Analysis Summary* PAS EWK-11-001 (2011).

[92] J. Allison *et al.*, "Geant4 developments and applications", *IEEE Transactions on Nuclear Science* **53,1** (2006) 270.

[93] J.M. Campbell ans K. Ellis, http://mcfm.fnal.gov/.

[94] D. Konstantinov, J. Komaragiri and Th. Peiffer, https://twiki.cern.ch/twiki/bin/view/CMS/SingleTopTurnOnCurves.

[95] CMS Collaboration, *CMS Physics Analysis Summary* PAS BTV-11-001 (2011).

[96] A. Rizzi, https://twiki.cern.ch/twiki/pub/CMS/BTagWeight/BTagWeight.pdf.

[97] CMS Collaboration, *CMS Physics Analysis Summary* PAS JME-10-010 (2010).

[98] CMS Collaboration, "Absolute Calibration of the Luminosity Measurement at CMS", **DP-2011/002** (2011).

[99] A.O.M. Iorio, L. Lista, M. Merola *et al.*, "Measurement of the single-top t-channel cross section at sqrt(s) = 7 TeV with a template fit analysis", *CMS Analysis Note* **2011/229** (2011).

[100] CMS Collaboration, *CMS Physics Analysis Summary* PAS TOP-11-021 (2011).